COMPUTATIONAL FLUID DYNAMICS FOR LNG VAPOR DISPERSION MODELING: A KEY PARAMETERS STUDY

A Dissertation

by

BENJAMIN R. CORMIER

Submitted to the Office of Graduate Studies of
Texas A&M University
in partial fulfillment of the requirements for the degree of

DOCTOR OF PHILOSOPHY

August 2008

Major Subject: Chemical Engineering

COMPUTATIONAL FLUID DYNAMICS FOR LNG VAPOR DISPERSION MODELING: A KEY PARAMETERS STUDY

A Dissertation

by

BENJAMIN R. CORMIER

Submitted to the Office of Graduate Studies of
Texas A&M University
in partial fulfillment of the requirements for the degree of

DOCTOR OF PHILOSOPHY

Approved by:

Co-Chairs of Committee,	M. Sam Mannan
	Mahmoud M. El-Halwagi
Committee Members,	Charles Glover
	Debjyoti Banerjee
Head of Department,	Michael Pishko

August 2008

Major Subject: Chemical Engineering

ABSTRACT

Computational Fluid Dynamics for LNG Vapor Dispersion Modeling:

A Key Parameters Study. (August 2008)

Benjamin R. Cormier, B.S, Virginia Tech; M. S., Texas A&M University

Co-Chairs of Advisory Committee: Dr. M. Sam Mannan
Dr. Mahmoud M. El-Halwagi

The increased demand for liquefied natural gas (LNG) has led to the construction of several new LNG terminals in the United States (US) and around the world. To ensure the safety of the public, consequence modeling is used to estimate the exclusion distances. The purpose of having these exclusion distances is to protect the public from being reached by flammable vapors during a release. For LNG industry, the exclusion zones are determined by the half lower flammability limits (half LFL, 2.5% V/V). Since LNG vapors are heavier-than-air when released into atmosphere, it goes through stages, negative, neutral and positive buoyant effect. In this process, it may reach the half LFL.

The primary objective of this dissertation is to advance the status of LNG vapor dispersion modeling, especially for complex scenarios (i.e. including obstacle effects). The most used software, box models, cannot assess these complex scenarios. Box models simulate the vapor in a free-obstacle environment. Due to the advancement in computing, this conservative approach has become questionable. New codes as computational fluid dynamics (CFD) have been proven viable and more efficient than box models. The use of such advance tool in consequence modeling requires the refinement of some of the parameters. In these dissertation, these parameters were identified and refine through a series of field tests at the Brayton Firefighter Training Field (BFTF) as part of the Texas A&M University System (TAMUS).

A total of five tests contributed to this dissertation, which three of them were designed and executed by the LNG team of the Mary Kay O'Connor Process Safety Center (MKOPSC) and the financial support from BP Global SPU Gas (BP). The data collected were used as calibration for a commercial CFD code called CFX from ANSYS. Once the CFD code was tuned, it was used in a

sensitivity analysis to assess the effects of parameters in the LFL distance and the concentration levels. The dissertation discusses also the validity range for the key parameters.

ACKNOWLEDGEMENTS

I am deeply grateful to my advisor, Dr. M. Sam Mannan, for all his feedbacks and his guidance through my education at Texas A&M University. I would like to acknowledge my committee members, Dr. Mahmoud El-Halwagi, Dr. Charles Glover and Dr. Debjyoti Banerjee. Thanks to all the students and especially to the staff of the Mary Kay O'Connor Process Safety Center for their assistance and friendship during my stay at the Center. I would like to recognize the efforts of the LNG team, Jaffee Suardin, and Morshed Rana, who helped in the realization of field tests. I would like to thank Robin Passmore, and Benedict Ho from BP Global SPU Gas for their financial support and guidance in the realization of this dissertation. I want to acknowledge Kirk Richardson from the Brayton Fire Training Field of the Texas A&M University System and the firefighters who provided guidance in the realization and the execution of these field tests in a safe manner. Ray Peacoe, from Detection & Measurement System, Inc. who help not only to select the detection equipments but also to help in the troubleshooting. Mike Moore from Flameout who helps to start this work by sharing his knowledge in field testing. And last but not least, I am grateful to my friends here who helped through my stay at Texas A&M University.

TABLE OF CONTENTS

Page

CHAPTER Page

CHAPTER Page

LIST OF FIGURES

Page

Page

Page

Page

LIST OF TABLES

Page

CHAPTER I

INTRODUCTION*

1.1 Background on LNG

LNG refers to natural gas converted into liquid state by super cooling to -260°F (-162.2°C). LNG commonly consists of 85%-98% methane with the remainder being a combination of nitrogen, carbon dioxide, ethane, propane, and other heavier hydrocarbon gases.

The super cooling process of LNG is performed at temperature of -260° F (-162.2°C) under atmospheric pressure reducing the volume by 600 times as compared to its gas phase (at standard conditions) into its liquid phase. This also provides cost-effective LNG containment while removing some undesired impurities such as sulfur and water. The liquid phase also permits cost effective LNG transportation across great distances onshore and offshore, at atmospheric pressure. LNG may be stored for a long period allowing for use to meet peak demand in certain seasons. Because of these advantages, LNG is expected to play an increasingly vital role in the industry and energy market by supplementing conventional sources of natural gas in the next several decades.

1.1.1 Growth of LNG demand

Demand for LNG as an energy source is increasing. The natural gas energy consumption in the United States (US) is about 25% of the overall energy. According to the estimation of the energy information administration (EIA), the production of natural gas is expected to increase to 20.5 trillion cubic feet (Tcf) in 2010 and 21.9 Tcf in 2025, which is slower than the increase in consumption as shown in Figure 1.

This dissertation follows the style and format of the *Journal of Loss Prevention in the Process Industries.*

*Part of this chapter is reprinted from *Liquefied Natural Gas: New Research*, Benjamin Cormier, Jaffee Suardin, Morshed Rana, Yingchun Zhang and M. Sam Mannan, Development of design and safety specifications for LNG facilities based on experimental and theoretical research, Copyright (2008) with permission from Nova Science Publishers.

The gas demand is rising sharply as well as the natural gas price. LNG has been considered as an alternate fuel that can meet 20%-25% of the demand because of its low production cost and practicability in transportation and storage.

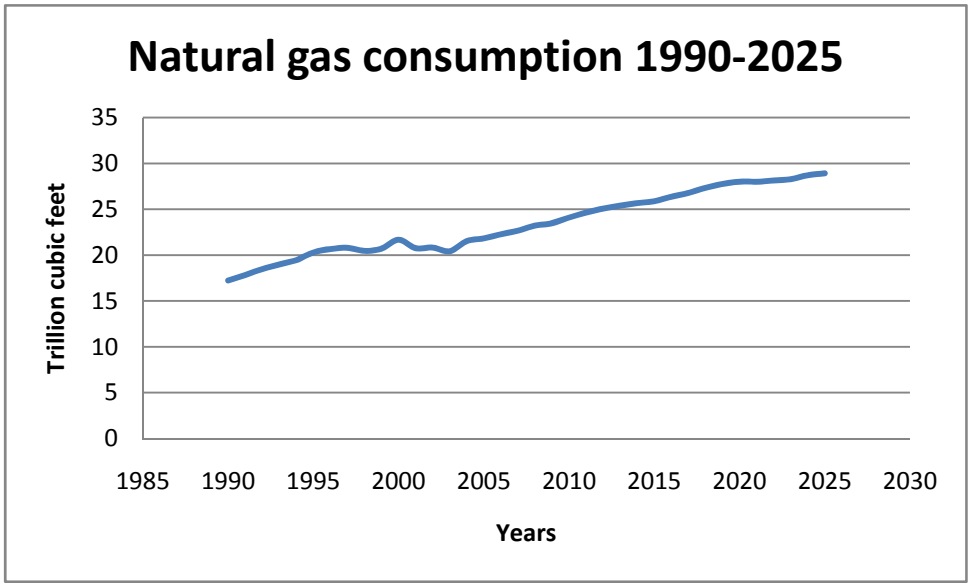

Figure 1. US gas production and consumption (Energy Information Administration, 2004)

Currently, there are at least 113 active LNG facilities across the US, including marine terminals, operating and storage facilities for use during periods of peak natural gas demand ("peak shaving") or as a base load source of natural gas. Among those facilities, there are eight active marine LNG import terminals: Lake Charles and Sabine, Louisiana; Everett, Massachusetts; Elba Island, Georgia; Cove Point, Maryland; Freeport, Texas, Penuelas, Puerto Rico, and Kenai, Alaska. As projected natural gas demand in the US has increases, EIA expects three new LNG terminals to be constructed within the next four to five years: over 40 LNG importation terminals have been approved, proposed, under consideration and investigated. The US LNG deliverability growth is shown in Figure 2.

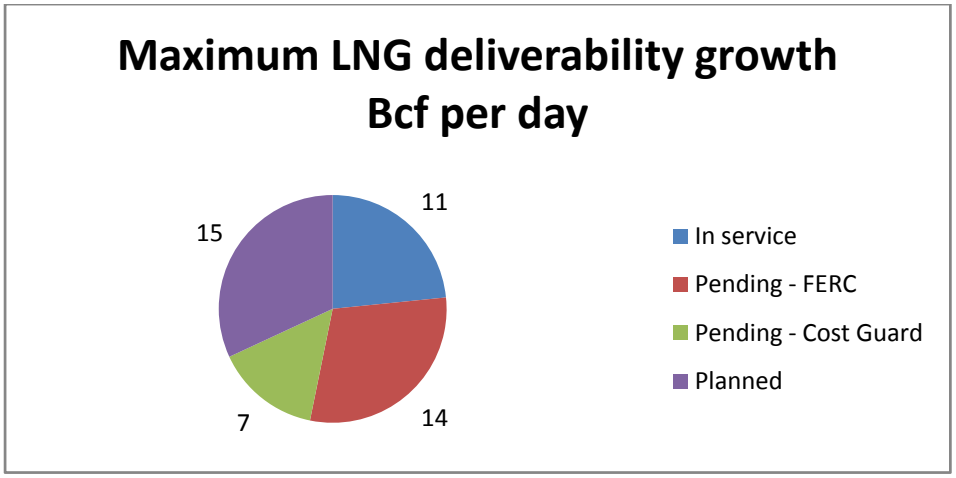

Figure 2. US LNG deliverability growth(Energy Information Administration, 2004)

1.1.2 Modern LNG facilities

The typical LNG facility today, ranging from large base-load liquefaction plants to small satellite storage units, consists of extremely large process units annually producing millions of tons of LNG or turnover capacity. Modern, large atmospheric LNG storage tanks have a capacity of 150,000 to 200,000 m^3 each. Recently designed loading jetties are capable of loading 12,000 m^3 LNG per hour into large cargo ships (Kuhwoi, et al., 2005). Generally, LNG facilities are divided into four different types as follows (West & Mannan, 2001, Zuber, 1976):

- Gathering and liquefaction plants. This is where the natural gas is liquefied, sold, and shipped with LNG tanker.
- Base-load terminals. This is where the shipped LNG is received, stored, vaporized, and send to gas pipelines to consumer at a normal rate.
- Peak shaving plants. This is where the extra amount of the available gas (usually during warm weather) is intentionally liquefied, stored and will be used only during peak season where the normal LNG distribution rate is not sufficient. The LNG is re-vaporized and send convert extra gas to meet the future demand.
- Satellite facilities. This is similar to the peak shaving plant but without the liquefaction unit. LNG is shipped and stored in smaller quantities with LNG truck or barge. The location is usually in remote location where the peak shaving facility is not available.

1.1.3 LNG safety and security

LNG is highly flammable and poses potential hazard to the surrounding communities. The increasing demand for natural gas is significantly increasing the possibilities of new LNG terminal construction near major population centers on the US coasts. Hence, the risk posed has created controversy over facility siting involving the LNG industries, local and federal government regulatory bodies, and the public adjacent to the proposed facilities. The damage or disruption caused by an LNG at terminal or facility incident could curtail the possibility of new LNG deliveries; thus, impacting natural gas supplies. The application of appropriate measures to ensure safety, security, and reliability through off-site and on-site competent risk and safety analysis of current and future LNG terminals and facilities are critical from both public safety and property perspective as well as from reliability of regional energy supply standpoint.

1.1.4 Hazards

In this section, we identify and discuss several potential hazards that could arise from an LNG spill. The following potential hazards are of an LNG spill are described in the following pages.

- Cryogenic hazards
- Over-pressurization
- Flash fire
- Pool fire
- Jet fire
- Rapid phase transition (RPT)
- Vapor cloud explosion (VCE)
- Rollover

1.1.4.1 Cryogenic hazards

LNG is stored and transported at very low temperature, around -260°F. Cryogenic hazards include extreme thermal effects associated with freezing of living tissue as a result of direct contact with very cold liquid. Cryogenic fluids may cause the brittlement and subsequent failure of containment materials and structure. For instance, carbon steel loses ductility and

impact strength (ability to withstand an impact force) at cryogenic temperature. Thus, careful selection of materials for equipment involved in the process (e.g., tank, pipe, pump, gas detector, valve, flow meter, etc) is critical for the LNG industry.

1.1.4.2 Over-pressurization

The potential for over-pressurization is a recognized hazard in facilities that handle refrigerated or liquefied gases, including LNG. It is often possible to isolate a vessel or a portion of a pipe by closing valves at both ends while the vessel or pipe contains a significant quantity of liquid. If the temperature of the liquid is increased, e.g., due to heat transfer through an insulating cover, the liquid will expand due to the temperature increase and also will vaporize. The vapor generated will cause the pressure within the vessel or pipe to increase and may ultimately result in vessel or pipe failure, particularly if safety protective equipment (relief valves, etc.) are not available (West & Mannan, 2001).

1.1.4.3 Flash fire

LNG will evaporate upon releasing and the vapor generated by this boiling liquid will start to mix with the surrounding air and will be carried downwind with the air creating a heavier-than-air, cold vapor. As the cold vapor cloud continues to be carried downwind, it will mix with additional air and be further diluted. However, some portion of the vapor cloud will be within the flammable limits (between 4.4-16.5% volumetric concentration mixture with air). If this flammable portion comes in contact with an ignition source, the vapor cloud may ignite. The flame might then propagate through the cloud, back to the source of the vapor, particularly if the flammable portion of the cloud is continuous. This simple burn-back of an unconfined vapor cloud can cause secondary fires by igniting materials in the path of the flame and can cause severe burns to persons caught within the cloud. Damage to equipment will generally be limited since the time of exposure to the fire will be relatively short (Zinn, 2005).

1.1.4.4 Pool fire

LNG may accumulate as liquid on the ground from an accidental if the spill is of sufficient size. If any ignition source is encountered, a pool fire can occur. Ignition can occur at the pool location (either immediately or delayed), or the pool can be ignited by a vapor cloud fire. The pool fire will continue if the spill expands from its source and continues evaporating.

Compared to a vapor cloud fire, the effects are more localized, but of longer duration (Qiao, et al., 2005, Zinn, 2005).

1.1.4.5 Jet fire

When a flammable liquid is accidentally released from pressurized containment, the leak may form a spray of liquid droplets and vapor. If ignited, the resulting fire is termed jet fire. Such a fire also can result from a pressurized vapor leak. Jet fires present the same types of hazards as pool fires, i.e., direct flame contact and radiant heat. However, the radiant heat from a jet fire is often greater than that from a pool fire of similar size.

1.1.4.6 Rapid phase transition

The phenomenon of rapid vapor formation with loud "bangs" has been observed when LNG is released under water. This non-flaming physical interaction is referred to as "rapid phase transition" or "flameless explosion".

1.1.4.7 Vapor cloud explosion

If the flammable vapor cloud evolving from an accidental LNG spill, as carried downwind, reaches a confined area, damaging overpressures or gas explosion may occur. The damage by such an explosion is limited to the enclosed area itself. Most buildings will withstand very little internal pressure, and when the pressure limit is reached, the building actually explodes (Kuhwoi, et al., 2005, West & Mannan, 2001).

1.1.4.8 Rollover

The addition of LNG with different densities to partially filled LNG tanks or the preferable evaporation of nitrogen has been known to lead to the formation of stratified layers. The density difference may be due to different sources of LNG or the weathering of LNG in the tank. Due to heat and mass transfer, the densities of the two layers approach each other. Eventually, these two layers mix resulting in a sudden increase in the vapor evolution and sometimes tank pressure. Rollover may result in excessive loss of valuable fuel at best, or lead to an incident under extreme conditions.

1.1.5 Overview of LNG vapor dispersion

An LNG vapor cloud is the gas cloud developed from an LNG release into the atmosphere, which is flammable between 4.4% v/v (Lower Flammability Limit, LFL) and 16.5 % v/v (Upper Flammability Limit, UFL). In an unconfined space, the cloud burns slowly and quietly once ignited. In a confined space, it may produce an explosion and damage the surrounding structures due to gas expansion (up to 8 times larger than the original volume). Figure 3 shows the exclusion zone for LNG vapor cloud.

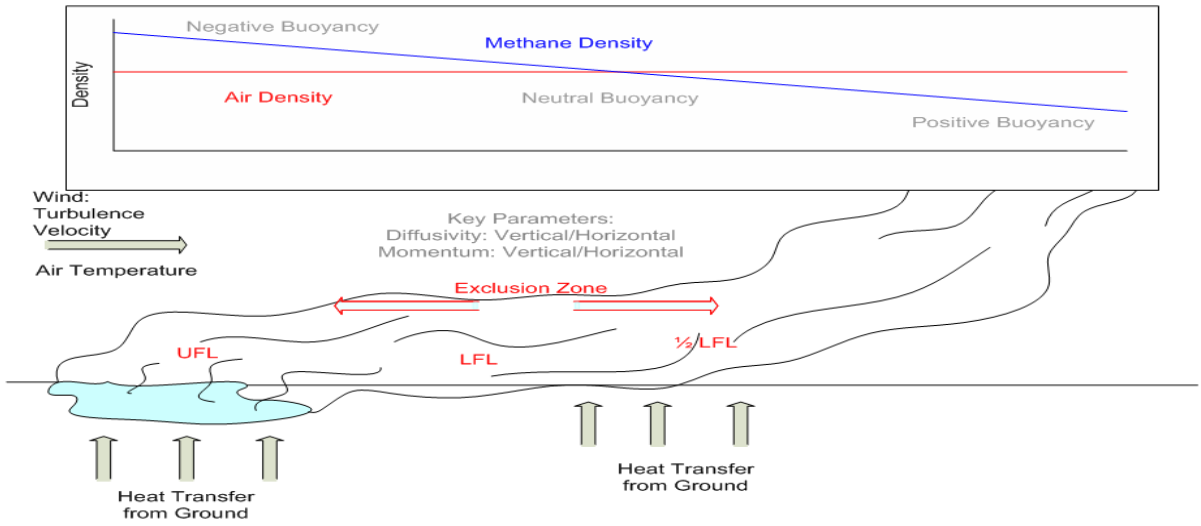

Figure 3. Exclusion zone description

This figure also describes the change in the density of LNG vapor during its dispersion. At room temperature, methane gas is not visible and its density is lighter than air. The cryogenic temperature of LNG is around 110 K (-260 F) at atmospheric pressure. When released into the atmosphere, it will vaporize rapidly and form a denser-than-air gas (1.5 times heavier than air) due to the LNG's extremely low temperature. LNG vapors are usually associated with a visible white cloud. This is because the cold vapor cloud condenses the water content in the air into a visible white condensate cloud, which may or may not represent the actual methane cloud. As the vapor cloud progresses through the atmosphere, two mechanisms are identified to dilute the concentration to LFL downwind: (i) Heat transfer from the surroundings may warm and

then expand the vapors to the point that the cloud start to lift off, and/or (ii) wind or forced entrainment may dilute the concentration below the LFL. Models are needed to predict the concentration downwind.

1.2 Motivation

The development of LNG terminals requires a deep evaluation of the potential release consequence associated with these installations. Figure 4 shows a typical configuration of an LNG base-load terminal. The LNG terminal is composed of an off loading desk, storage tanks, control room and re-gasification unit. The off loading desk is where the LNG tanker is anchored and then loading arms are used to transfer the LNG from the ship to the storage tanks. The storage tanks may be located near off-shore or inland. Several release scenarios could be developed from the current configuration.

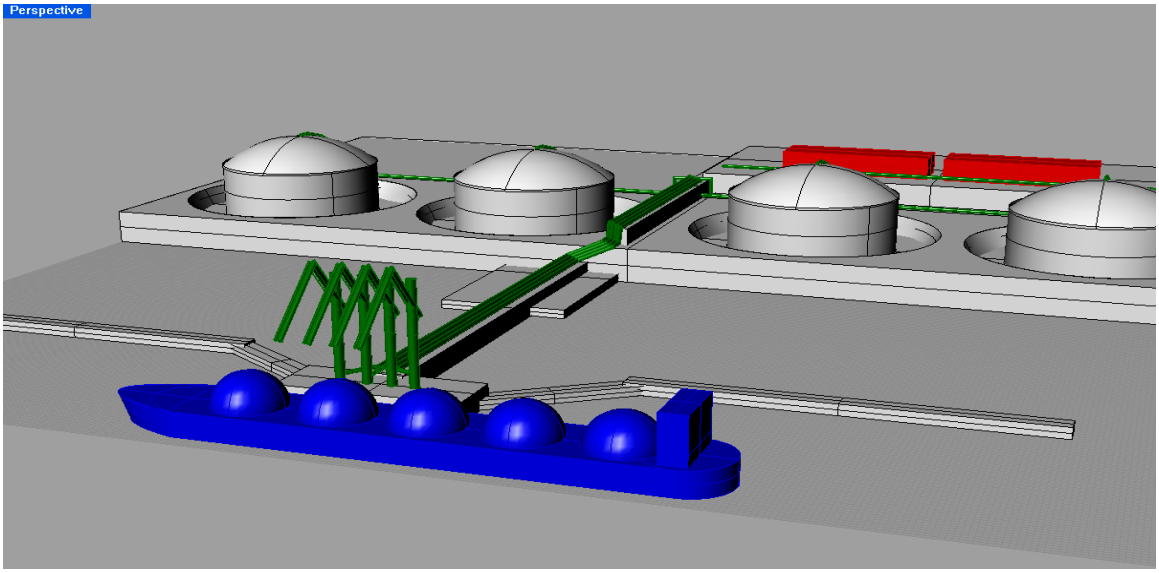

Figure 4. Typical representation of LNG base-load terminal

An LNG release on land or water may happen during normal operations. For example, an LNG release may occur during the liquid transfer between the tanker and the storage tanks, where LNG may be released onto water in between the desk and tanker or the land and the off loading desk. Another release scenario may occur when there is a rupture in the pipeline either

from the inlet line or the tanker itself. This release would be on land inside the containment area.

While these two potential release scenarios described above are illustrated in the Figure 4, the complexity of these releases and the interactions between the surroundings and the release is evident. Complex scenarios call for more advanced tools to simulate these scenarios. For instance, when LNG is released onto water between the tanker and the off loading desk, the LNG pool will form between the two obstacles. Then, vapors will be generated from the pool and will disperse according to the wind direction and the obstacles. US regulations require the use of consequence modeling tools to assess the exclusion zones for LNG industry. The conventional modeling, called free-obstacles two-dimensional dispersion cannot account for such features and complexity. Advance tools such CFD codes may be used for consequence modeling to estimate the exclusion zones. This consequence modeling approach is not only applicable to LNG terminals, but also other facilities where consequence modeling on complex scenarios is needed.

1.3 Problem statement

A vapor dispersion phenomenon is a complex task especially for heavy gas such as LNG vapors. The prediction of the flammable cloud is important information not only for the public but also the operator. The exclusion distances are meant to protect the public from the exposition of flammable vapors. The exclusion distances are estimated using current modeling software as called "box models". These box models have limited capabilities when it comes to the estimations of LFL distance including obstacle effects. New tools are needed to incorporate the obstacles in the modeling, in order to assess their effects on results. It would be important information not only for the operator to plan the strategy in a case of a release but also to improve/develop design to reduce the LFL distance and exclusion zones.

Simple to complex models have been developed and compared to experimental data to obtain a certain level of confidence in the prediction of the exclusion distances. Today there is a need to assess complex scenarios (including complex geometry and obstacles). The applicability of the previous developed models is limited in complex scenarios. Several groups of research

have been focusing on using CFD code, which seems to be an ideal candidate for the current needs of evaluation for complex scenarios.

CFD modeling requires a detail and time consuming setup compared to box models. CFD modeling is capable of handling obstacles in a three dimensional environment, it presents itself as being an ideal candidate for consequence analysis tools for complex scenario. It is not only capable of assessing the effectiveness of passive barrier such as dike (that may have an effect on the exclusion zones) but also it may be used a design and plant layout tool. Even though the open literature has grown on the use of CFD for consequence modeling, there is no detailed procedure on how to address complex scenarios and verify the calculation involved with CFD specific to LNG vapor dispersion. CFD consequence modeling is based on a specific scenario which makes the task of developing standard guidelines difficult.

The uncertainties with any models need also to be assessed to give to the user an understanding of the uncertainties associated with the simulation and results. This assessment may be performed using a sensitivity analysis on the key parameters.

1.4 Objectives

This work focuses on the potential use of a CFD model for LNG vapor dispersion modeling. The objective of this research is to identify the gaps and the key parameters in the current LNG vapor dispersion modeling, then to use CFD to advance LNG vapor dispersion modeling. The output of this work is to provide a workable version of a CFD model using a general purpose CFD model. To accomplish these goals, experimental work is needed to illustrate the capability of CFD models for LNG vapor dispersion modeling with obstacles. The objectives of this work include:

- Gaps identification on vapor dispersion through literature review
- Identification of parameters that needs to be refined
- Fields tests will be carried out at the BFTF to refine the parameters needed
- Data analysis on the collected data
- CFD modeling comparison against data collected and developing a strategies to simulate specific scenarios

- Sensitivity analysis on the key parameters

Once the gaps and key parameters are identified, a modeling strategy and experimental plan are developed to address these gaps and evaluate the effects of key parameters.

The experimental plan includes a series of three main field tests. The field tests are performed at the BFTF where LNG is allowed to be released. The experimental work focuses first on a better definition of the source term which is incorporated into simulation of vapor cloud. This source term is then compared and validated using the experimental data collected at the BFTF at Texas A&M University.

A sensitivity analysis is performed to estimate the impact of the model parameters after the model is tuned with the data collected at the BFTF. A sensitive analysis on the key parameters is performed to estimate the effects of these parameters on the simulation results. The sensitivity analysis should help engineers to estimate the degree of uncertainties in the use of CFD in the consequence modeling.

1.5 Organization of the dissertation

The main objective of this dissertation is not only to advance the status of LNG consequence modeling through experimental work but also to provide a well-detail literature review on vapor dispersion on dense gas for further research.

Chapter I introduces the background in LNG and the role of LNG in near future for the US energy. Handling cryogenic liquid like any other materials has its hazards, which needs to be well understood to prevent large consequences. This chapter also introduces the motivation for the need of new tools that are not only capable to assess complex scenarios, but also to study new concept or simply improve current design. Chapter II is a well details background in vapor dispersion modeling, where the phenomena include in vapor dispersion are reviewed and key parameters are identified. It also includes a review of the models that were developed especially for LNG vapor dispersion and their limits. The gaps and the direction of this research are presented in this chapter. Chapter III is the description of the test facility at BFTF. The description of tests and their analysis are also provided in this chapter. The analysis is composed of vapor dispersion and evaporation rate profile. These information are then used in

chapter IV, where the model is introduced and the numerical analysis is performed. The numerical analysis is composed of the tuning of the parameters for the model and then the model is used in the sensitivity analysis to obtain a degree of understanding in the parameters used.

CHAPTER II

BACKGROUND FOR VAPOR DISPERSION MODELING*

The modeling of such phenomenon is a complicated process and should be approached with a rigorous methodology to evaluate the important parameters. The modeling is composed of two steps: (i) the source term and (ii) the vapor dispersion. The source term includes the physical description of the LNG pool to simulate the gas phase generation. The vapor dispersion includes the physical description of the entrainment of the gas in the air and dilution process.

2.1 Phenomenology of source term

Several models have been developed to estimate the evaporation rate for a release scenario. Most of the work done on LNG pool formation is summarized in this section. Several detailed reports that sum up the equation involved in the estimation of the evaporation rate profile for LNG pool have been published, (Briscoe & Shaw, 1980) and (Melhem, 1991). The approaches included a mass, momentum and energy balance in the estimation of the evaporation rate profile with a pre-assumed LNG pool shape.

For a continuous release in an area with boundaries, if a pool is formed, the pool shape and size are limited by the boundaries. When the liquid reaches the boundaries, the depth of the liquid will start rising. On the other hand, for a continuous release in an open area, if a pool is formed, LNG will spread onto the surface. The pool shape and size are not limited by any boundary, but primarily depend on the quantity release.

---

*Part of this chapter is reprinted from *Liquefied Natural Gas: New Research*, Benjamin Cormier, Jaffee Suardin, Morshed Rana, Yingchun Zhang and M. Sam Mannan, Development of design and safety specifications for LNG facilities based on experimental and theoretical research, Copyright (2008) with permission from Nova Science Publishers.

The evaporation rate profile depends mainly on the heat transfer between the cryogenic liquid and the surface the cryogenic liquid contacts. For releases on a solid surface, the surface will be cooled and the evaporation rate will decrease over time. In the particular case of a release on water, the evaporation rate profile depends on the water and the turbulence created by the release.

The evaporation rate profile is one of the critical input parameters in the vapor dispersion modeling. For the purpose of simulation, the source term has to be simplified, but not to the point that the physical descriptions are diminished and not representative of the phenomenon. The phenomenology of the source term is reviewed to develop an evaporation profile that will be considered at a source term for the LNG vapor dispersion modeling, where the key features are identified.

2.1.1 Approach in the evaluation of the evaporation rate

The evaluation of the evaporation rate starts with the determination of the scenario. Assuming that the LNG flow rate is enough to form a pool, the LNG spread includes several variables that are represented in Figure 5. As LNG reaches the surface, it starts spreading over the surface until either it reaches the minimum thickness or the boundaries of the area (if any). In both cases, the evaporation rate profile should be developed with a transient function.

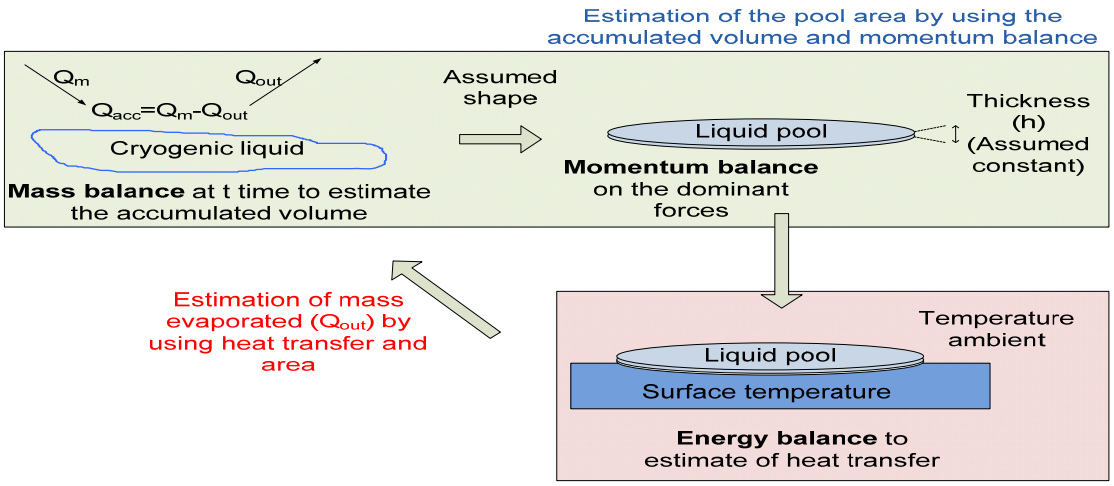

Figure 5. Pool formation calculation scheme

Depending on the scenario, the mass accumulated on the surface creates a pool. The pool starts spreading as the dominant forces equalize (inertia and gravity forces). Meanwhile, LNG starts vaporizing because of the warm surface. If the mass evaporation rate is higher than the rate of mass released, the size of any existing pool will decrease. For the pool spreading scheme shown schematically in Figure 5, the primary parameters include:

1. Release scenario
2. Flow rate of LNG into the pool
3. Pool geometry and thickness
4. Forces involved during pool formation to determine the rate of spreading
5. Heat transfer and turbulence effect on evaporation rate

The secondary parameters also depend on the scenario, including:

For a release onto land

1. State of the land (sand, grass, humidity)
2. LNG composition
3. Roughness

For release onto water the followings are also considered,

1. Wind and waves
2. Ice/hydrate formation
3. Water temperature

2.1.2 Release scenarios

The release scenarios presented in this section illustrate the involvement of the variables in the source term. With this purpose in mind, two possible locations are identified, an onshore and offshore release. An onshore release may occur inside a terminal during normal operation, and the release is on land or concrete. An offshore release may occur from a LNG tanker, and the release is onto the water surface. The water surface is assumed to have infinite heat sink.

2.1.2.1 Onshore release

As illustrated in Figure 4, several scenarios are possible from an LNG Terminal. US regulations require the estimation of exclusion distances for a full bore release of 10 minutes. The 10 minute period is based on the time to identify, to react and to stop the leak. The LNG released is usually contained in an impoundment. From the release point (i.e. storage tank) to the impoundment, several vapor dispersion modes may be performed to evaluate the exclusion distances:

1. Release inside the dike (around the storage tank)
2. Release progressing through the trench to the impoundment area
3. Release into the impoundment

All these release scenarios have boundaries for the pool formation. The evaporation rate profile during this scenario should be a transient function. Figure 4 also shows the water areas where a release may happen. This scenario topic is addressed in the next section.

2.1.2.2 Marine transportation release

Three main scenarios are identified for an LNG release from a LNG tanker. The scenarios depend on the location of the hole in the tanker: (i) hole above the water surface (Category I), (ii) hole at or close to the water surface (Category II), (iii) hole underwater (Category III).

The flow rate out of a breached tank depends on the location of the hole relative to the liquid surface (hydrostatic depth), the size of the hole, and the shape of the hole. If the hole is at water surface or underwater, additional phenomena due to water inflow will affect the LNG flow rate. In addition, the LNG release onto water depends on the relative distance between the breach in the inner tank and the hole in the outer hull. Table 1 shows the breach diameter used for LNG tanker by different researchers.

Category I has the highest hole location. Therefore, if any LNG reaches the water surface, it will penetrate the surface creating more turbulence at the location of contact. The LNG jet will penetrate the water column; break up partially into droplets in different sizes which evaporate due to heat transfer from the water. The remaining un-evaporated liquid will rise to the

surface and form a pool. Another phenomenon in this type of release is a formation of liquid aerosols and flashed vapor which reduces the volume of LNG contributing to pool spread.

Category II contains two scenarios: (1) both the holes are just above water level and (2) the inner hole is above water level and outer hole is partially under water level. In Category II.1 this scenario is more likely to create a quiescent release onto water because of substantial horizontal momentum of the released jet. This will result in a larger pool than in the other categories. Most of the available published information, referred to as a release on water, seems to apply to this type of release. In a Category II.2, part of the LNG release may undergo evaporation due to mixing with water flowing into the hold space thereby reducing the volume in the spreading pool.

Category III releases originate underwater and rise to the surface to create a pool. In the process of the rising to the surface, part of the jet may be evaporated.

Table 1. Breach diameters used by different researchers

Event Type	*Range of breach diameter (m)*	
	Det Norske Veritas (DNV) (DNV, 2004)	Sandia National Laboratory (SNL) (Hightower, et al., 2004)
Puncture	0.25	-
Accidental operational	0.75	0.8 – 1.4
Intentional	1.5	1.6 – 3.9 (nominal 2.5 – 3.0)

The same type of scenario may be used for a release when the LNG tanker is anchored to the off-loading desk. The pool spread will be modified due to the boundary limits imposed by the desk and the LNG tanker.

The scenario evaluation is a critical step in the estimation of the consequence modeling. The presented scenarios are based on credible scenarios. The reader should be aware of the complexity of these scenarios and most of the phenomena such as the outcomes of LNG mixing with water are extremely difficult to evaluate. For the purpose of CFD consequence modeling

for vapor dispersion, gas phase, i.e. the evaporating LNG pool and turbulence associated with it, is needed.

2.1.3 Flow rate estimation

The determination of the flow rate depends on the scenario. Bernoulli's equation is used to calculate the flow rate at the release point (Crowl & Louvar, 2002):

$$\int \frac{\Delta P}{\rho} + \frac{\Delta \bar{u}^2}{2\alpha g_c} + \frac{g}{g_c}\Delta z + F = 0 \qquad (1)$$

where

P = the pressure

ρ = the density of the liquid

u = the average instantaneous velocity of the fluid

g_c = the gravitational constant

α = the velocity profile correction factor with the following values:

α = 0.5 for laminar flow, α = 1.0 for plug flow, and $\alpha \rightarrow$ 1.0 for turbulent flow

g = the acceleration due to gravity

z = the height above datum

F = the net friction loss term

For illustration of the flow rate calculation, it is assumed that the release is from a tanker. The flow rate of LNG is calculated by the gravity created inside a tanker in case of non-pressurized release. In the case of pressurized release, the pressure may be added as additional driven force. This model may be modified to fit a particular scenario. However, this is only applicable for a continuous release. In the case of a release from a tanker, the equation 4 may be modified to the following, known as the orifice equation:

$$Q_m = \rho \bar{u} A = \rho A C_d \sqrt{2\left(\frac{g_c P_{tank}}{\rho} + g h_L\right)} \qquad (2)$$

Q_m = the mass flow rate

ρ = the density of liquid

u = the mean liquid velocity

A = the orifice area

C_d = the drag coefficient

P_{tank} = the pressure inside of the tank

h_L = the level of liquid in the tank

g_c = the gravitational constant

g = the acceleration due to gravity

Other modifications of the Equation 1 are available from Crowl and Louvar's textbook (Crowl & Louvar, 2002) for any scenario (i.e. pipeline, etc.).

2.1.4 Pool geometry and thickness

The pool geometry depends on the boundaries and the feature of the surface. As stated previously, for the case of a release in an impoundment, the pool geometry will depend on the impoundment boundaries. When the LNG reaches a boundary, the LNG will accumulate and the level will rise. In the case of a release in an open area, the LNG will start spreading. The equivalent diameter is calculated from the assumed shape.

In the case of a quiescent release on sea water (open area) near the LNG tanker, a semi-circular pool may be used if it is assumed that the pool is anchored on one side of the ship. In the case of a more energetic release from higher ground, the pool shape may be more elliptical rather than circular due to the horizontal momentum from the LNG. The shape of the pool also may be influenced by the motion of the tanker, current and waves.

The spread model is determined for two types of release, continuous and instantaneous release. These equations are shown in rate spreading section.

Table 2 represents a compilation of minimal thickness values used by different researchers to terminate the spreading of the pool. It should be pointed out that some of the researchers measured these data while others have assumed the termination of pool spread at this thickness.

Table 2. Pool thickness data

Reference	*Pool Thickness*	*Substrate*	*Remarks*
Feldbauer(Feldbauer, et al., 1972)	1.8 mm	water	Analytical determination
Boyle and Kneebone(Kneebone & Prew, 1974)	1.7 mm	water	Test data
Opschoor(Opschoor, 1980)	5 mm	land	Analytical determination
DNV(Pitblado, et al., 2005)	100 mm (initial) 1 mm (maximum spread)	water	Analytical determination
SNL(Luketa-Hanlin, 2006)	1 mm (maximum spread)	water	Analytical determination
Esso(Hissong, 2007)	6.4 mm and 4.4 mm (minimum stable pool beyond which the pool breaks up)	water	Test data

2.1.5 Rate of spreading

Assuming that the flow rate is constant, the commonly used model for calculating the pool spread area in an open area is (Fay, 2003):

$$A_p = \frac{\dot{V}}{\dot{y}} \tag{3}$$

$\dot{V}$ = mean release rate

A_p = pool area

$\dot{y}$ = mean liquid regression rate

where

$$\dot{y} = \frac{\textit{Mean heat flux to the pool}}{\rho_L \lambda} \tag{4}$$

with

ρ_L = Liquid of density

λ = liquid latent heat of vaporization

This equation only gives the mean of the pool area spread. This equitation may be used when the information about the release scenario is not available or well defined. However, it does not account for a spreading pool. The mean liquid regression rate will change over time, if the spread pool area changes as well. The mean heat flux values are given in heat transfer section.

A spreading pool model was derived by Fay (Fay, 2003), which is applicable to cryogenic liquid pool spreading. The model describes a spread of a buoyant fluid released instantaneously onto water surface and three consecutive regimes of pool spread are identified. During each regime, certain forces are dominant and others are negligible. Momentum balance is needed to determine the size of the pool. The forces involved in the spreading of liquid are the gravity force (f_G), inertia force (f_I), surface tension force (f_{ST}), viscous drag forces (f_V), and the water forces (f_W) presented in Figure 6.

1. Gravity-Inertia Regime: gravity and inertia forces are dominant
2. Gravity-Viscous Regime: viscous force becomes too important to be negligible
3. Surface Tension-Viscous Regime: the surface tension becomes dominant

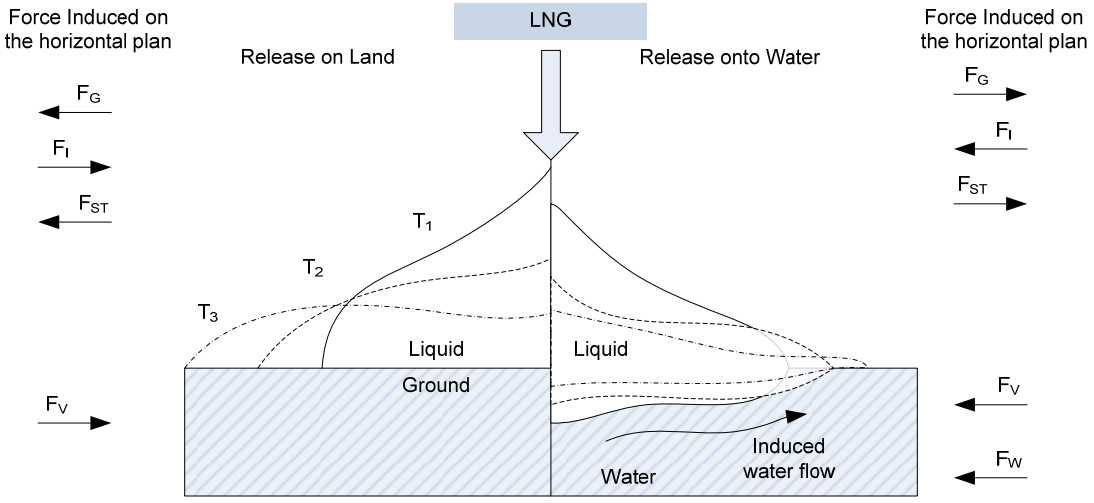

Figure 6. Momentum balance on LNG pool modified from (Briscoe & Shaw, 1980)

A cryogenic liquid spreading on the water surface will evaporate. Most of the evaporation and spreading occurs only during the gravity inertia regime (Briscoe & Shaw, 1980). Therefore, the Gravity-Inertia regime model is described below and used to predict the pool spreading. The main driving force is gravity. The gravity force pushes horizontally on the pool to spread the pool sideways and counterbalances with the inertial resistance of the liquid. The rate of spread for an instantaneously released volume is estimated by the following equations (Briscoe & Shaw, 1980):

$$F_G=F_I \tag{5}$$

$$h=\frac{V}{\pi r^2} \tag{6}$$

then the momentum balance can be written as:

$$\rho\pi r^2 hg\frac{\Delta h}{r}=-\frac{1}{\varepsilon}\rho\pi r^2 h\frac{d^2r}{dt^2} \tag{7}$$

$$r\frac{d^2r}{dt^2}=-\varepsilon\left(gh\left(\frac{\rho_w-\rho}{\rho_w}\right)\right) \tag{8}$$

$$\frac{dr}{dt}=-Ks\left(gh\left(\frac{\rho_w-\rho}{\rho_w}\right)\right)^{\frac{1}{2}} \tag{9}$$

$$Ks=\varepsilon^{1/2} \tag{10}$$

where

h = the minimum thickness

V = the total volume on spread on water

r = the radius of the pool, assuming that the pool is a circle

g = the gravity acceleration

ε = the inertia factor

ρ_w = the water density

ρ = the cryogenic liquid density

Fay's model provides a means of classifying the release into rapid (instantaneous) or slow releases on an open area. For releases in an impoundment, the spreading model may be used until the boundaries are reached.

This equation may be used to model the dynamic formation of the pool on a surface. This equation must be combined with the heat transfer to evaluate the evaporation rate at each instance.

2.1.6 Heat transfer and turbulence effect on evaporation rate

The heat transfer is the sum of the heat available around the pool involved in the evaporation of the LNG pool. Figure 7 shows a possible energy balance around a cryogenic pool.

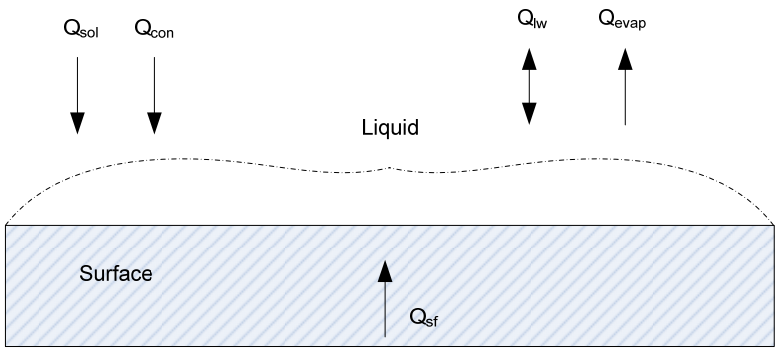

Figure 7. Energy balance on LNG pool (Melhem, 1991)

Then the energy balance may express with the following (Melhem, 1991):

$$\frac{dQ_t}{dt} = \frac{dQ_{lw}}{dt} + \frac{dQ_{sol}}{dt} + \frac{dQ_{con}}{dt} + \frac{dQ_{grd}}{dt} - \frac{dQ_{evap}}{dt} \quad (8)$$

where

Q_t = the total energy

Q_{con} = the surface conduction

Q_{sol} = the solar insolation

Q_{lw} = the long wave radiation

Q_{sf} = the convection from surface

Q_{evap} = the heat lost to evaporation

The general formula for the energy balance is simplified according to the scenario. The difference of temperature between the surface and the cryogenic liquid affects the heat transfer. Three regimes are possible, nucleate evaporation, film evaporation and transition regime. The heat transfer depends on the existence of these regimes. At high a temperature difference, a evaporation film regime is applied. At a low temperature difference, a nucleate evaporation regime is applied. Heat transfer may be evaluated by using standard film and transient evaporation correlation for a quiescent condition as reported in appendix A from Hissong (Hissong, 2007). This transition results in a higher heat transfer coefficient. Either on water or land, the same phenomenon is valid.

Once the pool spreads, the diameter may change as the heat transfer is affected by the change of surface temperature. The pool will stop spreading when the mass evaporated from heat transfer is equal to the mass released (mainly in the continuous release case). The pool may keep spreading beyond the initial spread when either the mass released increase or the heat transfer is reduced due to the change of surface temperature (i.e. change in surface temperature will reduce the heat transfer, thereby decreasing the mass evaporated, then forcing the pool to spread to reach the equilibrium between the mass evaporated and the mass released)

On land, high evaporation rates occur at the beginning during the film evaporation and transition regime and generally occur in a short time period. Once the surface is cooled (i.e., a low temperature difference), a nucleate evaporation is more likely to happen for the rest of the release. In a confined area, this would decrease the evaporation rate once the surface is cooled enough to sustain a pool.

For release on water, there are several ways that the evaporation rate may be influenced. Hissong (Hissong, 2007) assessed that a substantial increase in turbulence occurs when LNG is dumped into water at a high flow rate. Reports indicate an increase in turbulence by a factor of 10 or more results when the release rate increases by a factor of 4. This increase in turbulence leads to a much higher heat flux within the spreading pool. This conclusion is also drawn from

Briscoe and Shaw's study (Briscoe & Shaw, 1980). However, the turbulence created by LNG plunging jet into the water, the droplet formation, and the associated heat transfer has not been studied. Cryogenic liquid releases on water have a tendency to form ice underneath the cryogenic pool. The conditions of the ice and hydrate formation is not well understood either. A heat transfer model including ice formation was developed by Vesovic (Conrado & Vesovic, 2000, Vesovic, 2006). The ice formation or the temperature change of the surface suggests the evaporation rate may not be uniform over the pool area.

Turbulence and ice effects on the evaporation rate are also scenario related. For a release on land, in most cases, the cryogenic liquid is in a confined area, where the surface area is somewhat controlled (e.g.., impoundment, dike, or trench). The evaporation rate may be derivable from the energy and mass balance (Briscoe & Shaw, 1980). The evaporation rate for release on sea water is higher than a release on land because of the infinite heat sink from the sea water, except in the case of heavy rain. Rain may increase the evaporation when it falls into the trench or the impoundment. As of today, there is no data available to prove the effect of rain on an LNG pool.

2.1.7 Estimation of the mass evaporated at any given time

The mass evaporation rate is estimated using the liquid pool area and heat transfer/heat flux from the surface to the LNG. The transient mass evaporating model may be developed in three steps as described below and follow Briscoe and Shaw's (Briscoe & Shaw, 1980) or Hissong's (Hissong, 2007)work. At any given time step shown in Figure 5, the following order to calculate the evaporation may be applied:

1. The initial pool area is calculated using an assumed thickness and volume released (Q_{in}) through a rate of spreading at time *t*
2. The mass evaporated is calculated knowing the area of the pool and the heat transfer rate to the pool. A variable heat transfer model may be incorporated here (as function surface area and contact time).
3. Change of time, *t* to *t+1*
4. The mass evaporated (Q_{out}) is removed from the calculated pool area and the volume released is added to establish the new pool area.

5. Then, steps 2 through 4 are repeated until the volume release is ceased.
6. The mass evaporated is estimated through step 2 to 4 and the volume released for "dying" pool area is removed.

The size of the pool is determined by the quantity of LNG released and how much evaporates at any given time. Time-varying analysis should be used in any modeling because the phenomena involved are complicated. Many variables are involved and while one variable reaches its steady state value, another variable may start changing. Time-varying analysis will capture changes and effects among variables.

2.1.8 Other parameter considerations

2.1.8.1 Wind and waves

The effect of wind moves the pool in the wind direction. In the case of pool that is still forming due to a continuous release, the wind effect may increase the pool area. Waves also increase the surface area for releases in or on water. If the waves break the LNG pool apart, small LNG pools may be pushed into the water column resulting in substantially increased local evaporation rate. There are no studies that describe the effect of wind. However, tests have been conducted to determine the effect of breaking waves on LNG releases.

2.1.8.2 LNG composition

Usually, LNG is mainly composed of methane; most simulations today are done using pure methane as LNG. Therefore, the thermodynamic properties are assumed to be constant. During the pool spreading and evaporation, methane is preferentially emitted due to fractional distillation and the thermodynamic properties. The composition of the pool changes continuously with time due to fractional evaporation. However, the effect of changes in the density of the liquid in the pool is considered small regarding the affect on the pool spread.

RPT may occur during pool spread as a result of the mixing between LNG and water towards the end of the pool life due to increased concentration of heavier hydrocarbon. No systematic study results are available to determine the effect on pool spread by waves, wind, and composition.

2.1.8.3 Water temperature and ice/hydrate formation

Ice and hydrate formation have been observed in both large and small LNG releases onto water bodies. The condition in which ice or hydrate occurs is not well understood. Assuming that the release is happening in deep water and there is an infinite resource of fresh water, the formation of dense ice underneath the LNG is unlikely because of the constant mixing effect due to density changes in the water.

As the water is cooled by the LNG, the cold water sinks and warm water is pushed upward by the cold water movement, thereby creating a cycle where fresh water is continuously provided to the LNG. This phenomena results in an infinite heat sink for the LNG. The salinity of the water will change the heat capacity and in turn change the temperature profile of the water. The influence of the recycling of water underneath the pool on the heat transfer rate to the pool has not been studied.

2.1.9 Incorporation of source modeling into vapor modeling

Because the theoretical approach may not account for all the phenomena involved in the evaporation rate evaluation, today's best practice is to use a mean value for the mass evaporation rate over the maximum pool diameter possible (respect to the release). These values are from the published literature and usually estimated from actual releases and large release tests, shown in Table 3.

Table 3. Summary of the evaporation rate published in the literature

Reference	*Mass Evaporation rate, kg/m^2 s*	*Remarks*
	Heat transfer from water	
Waite and Whitehouse(Waite, et al., 1983)	0.049 to 0.19	Analytical results
Briscoe and Shaw (Briscoe & Shaw, 1980)	0.21	Analytical results
Bureau of Mines Test - (Burgess, et al., 1970)	0.181	Test data
Bureau of Mines Test - (Burgess, et al., 1972)	0.155	Test data
Shell Ltd - (Hightower, et al., 2004)	0.029 to 0.195	Test data
Esso - (Hightower, et al., 2004)	0.195	Test data
Maplin Sands - (Luketa-Hanlin, 2006)	0.085	Test data

Note: Test data and analytical results have been converted into mass evaporation rate using the following values for properties: ρ_L *=425 kg/m^3,* λ*=510 kJ/kg, T_{water}=293 K, T_{liquid} = 112 K*

The range of mean values is between 0.029 and 0.21 kg/m^2 s. The large range may be explained by the different scenarios and release sizes. The current software (Baik, et al., 2006) usually assumes the upper bound of this range, 0.15 to 0.185 kg/m^2 s, which gives a upward velocity from 0.08 to 0.10 m/s (with gas density of 1.78 kg/m^3). The discrepancy in the experimental data suggests the need for LNG release tests with the identification of the important feature of the scenario.

The mass evaporation rate is usually translated into an evaporation velocity in the vapor dispersion. Complex scenarios are focused not only on the effect of surrounding the vapor dispersion, but also on the refined physical descriptions of the source term. Source turbulence created results in an increase in the evaporation rate (where the mechanism is not well understood), which should be translated into higher evaporation velocity. By using a mean value for the evaporation velocity, this physical characteristic of the source term is lost. CFD

modeling has the capability to incorporate this higher evaporation rate and assess their effects on the vapor dispersion.

2.2 Phenomenology of LNG vapor cloud

Some hazardous substances are denser than air when released into the atmosphere. The dispersion behavior of these substances can differ considerably from the dispersion of atmospheric pollutants. It is important to understand the physical phenomena involved in dense gas dispersion. Gas can be denser-than-air for a number for reasons: (i) its molecular weight is larger than that of air, (ii) it is significantly colder than the air, (ii) and/or it consists partly of a suspended aerosol of liquid or solid particles. LNG vapor is heavier-than-air because of its high gas density at a cold temperature (normal evaporation point is 111 K). This section focuses on describing the phenomena involved in dense gas dispersion.

When a dense cloud is created at ground level from a release either on water or on land, several mechanisms are noticeable. This phenomenon may be described in two stages, (i) the initial evaporation off of LNG creating an upward (or vertical) velocity, and (ii) the horizontal mixing due to the wind entrainment. These two phenomena may overlap or may be one after the other one. The overlapping of these phenomena is influenced by the atmospheric boundary layer, which depends on the surface roughness and atmospheric stability. The atmospheric boundary layer condition describes the wind and temperature profile.

Depending on the atmospheric conditions, as the cloud travels in a horizontal direction (or downwind direction), gravity spreading flow occurs due to the density gradient in the horizontal plane. During an unstable stability condition, the buoyancy turbulence is dominant and during the stable stability condition, this turbulence is suppressed. At low wind velocity, this gravity spreading flow may displace the ambient atmosphere. This displacement makes the penetration of atmospheric wind difficult. Without external turbulences, breaking this pattern is limited and may result in a large vapor cloud.

Heat flux from the ground and the solar energy affects buoyancy turbulence inside the cloud. As the gravity flow takes place, the vapor cloud travels over the surface (either water or land)

emitting heat flux from the solar radiation. The heat flux increases the temperature of the cloud, leading to an increase of buoyancy turbulence in the vapor cloud.

2.2.1 Vapor dispersion modeling

The approach for this work was to study in details the parameters involved in vapor dispersion, especially for LNG. The algorithm behind vapor dispersion is described in Figure 8. Box models or CFD modeling for vapor dispersion would have the same type of inputs. The level of details that may be capture by CFD modeling is far superior to box models. In Figure 8, the algorithm may be divided in three sections, (i) problem definition, (ii) solver, and (iii) post processor. Typically, solver and post processor are not variable in the study of the key parameters. Using a commercial CFD code and proven viable throughout other fields reducing the uncertainties associated with the computational code calculations. The current best practice to assess the uncertainties of a model is to run a sensitivity analysis on the key parameters.

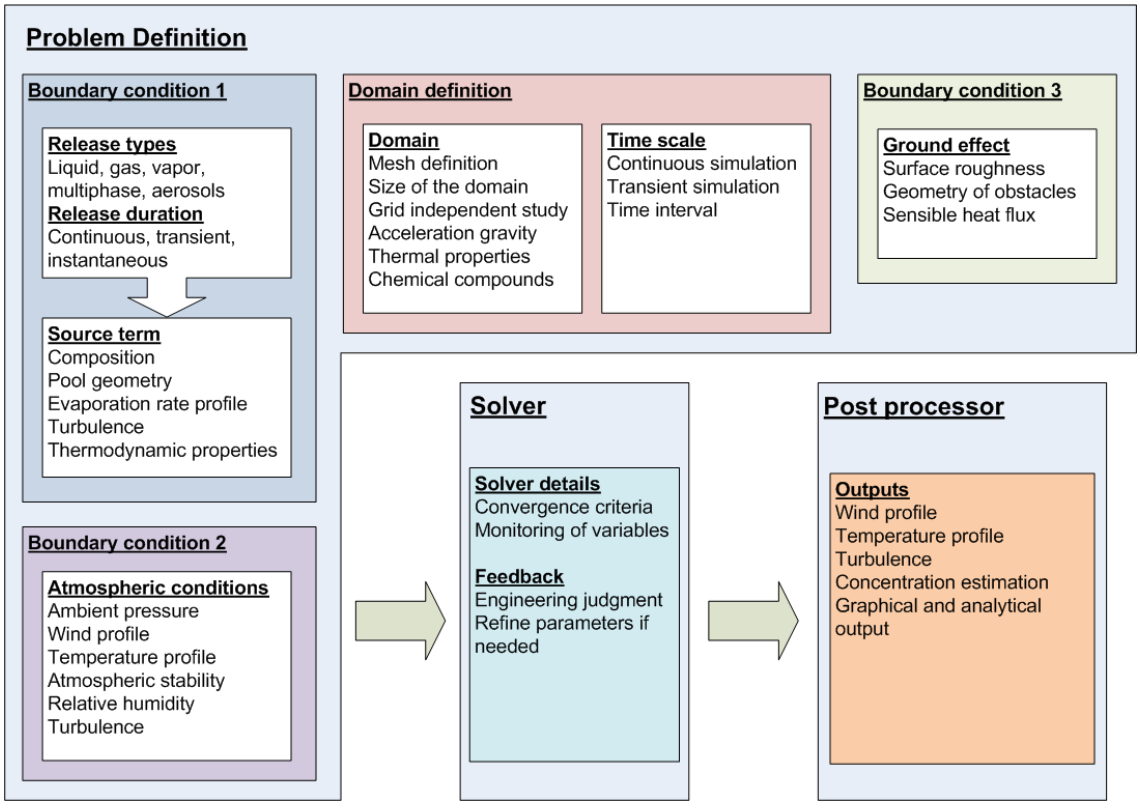

Figure 8. Algorithm beyond the vapor dispersion

As described in Figure 8, the parameters are defined at the problem definition. The problem definition is composed of four set of parameters, (i) domain definition, (ii) source term, (iii) atmospheric conditions, and (iv) ground effects.

2.2.1.1 Domain definition

CFD modeling requires the determination of the domain. The domain is then divided into finite elements with mesh technique. In each element, the governing and turbulence equations are solved simultaneously respect to a set of reference parameters, initial and boundary conditions. The size of the domain is strongly scenario dependent. Since simple models do not need this input, they may be used to obtain a first estimate of the volume required for more advanced models such as the CFD model. This volume then is divided into small control volumes using a mesh technique. An unstructured or structured mesh may be used. Fine cells are used where high gradients are expected and coarse cells for the remaining areas. To establish the mesh independent from the domain, a mesh refinement procedure should be performed and to help identify the optimal mesh resolution. At least one reference variable should be monitored to estimate the mesh independently, in order to obtain independent mesh solutions. The use of a domain also permits the incorporation of obstacles and terrain features. The geometry in the domain may be adapted to simulate any type of obstacles shown in Figure 9. The obstacles are incorporated into the domain to assess the effects of them on the cloud dispersion. Passive barriers and layout configuration may be studied.

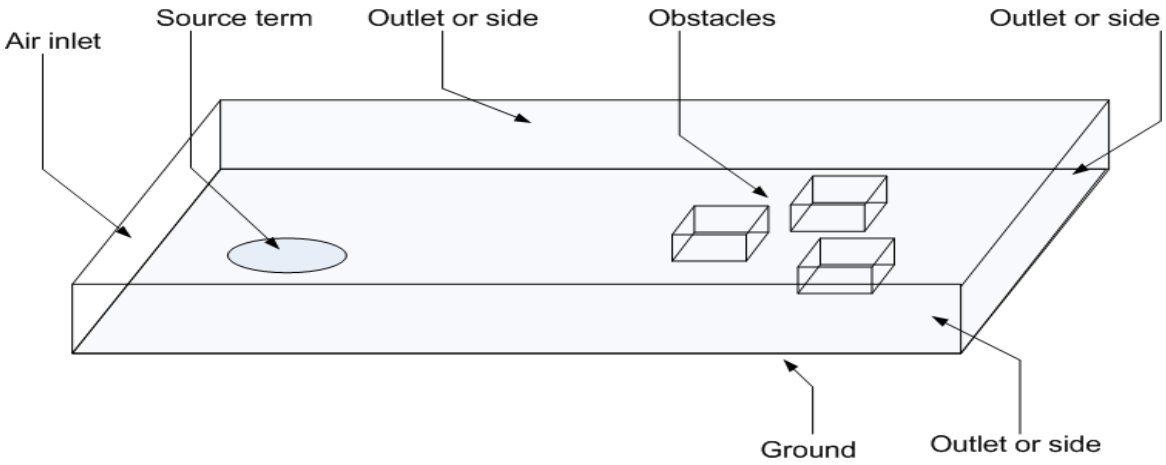

Figure 9. Domain simple with boundary conditions

The boundary condition can be set to either: inlet, outlet, wall, symmetric or opening (ANSYS, 2007):

- Inlet and outlet boundary: strictly lets a fluid in and out, respectively. It is usually used to simulate the incoming LNG (i.e. methane) or other fluid inputs. The wind flow also may be setup as an input. This condition does not allow back flow.
- Wall boundary: solid (impermeable) boundaries to fluid flow; it does not let any flow go through. It could be set to a temperature or heat flux with either smoothness or roughness values. It is usually used to setup the ground.
- Symmetric boundary: a mirror image plane of flow on the opposite side. By definition, a symmetry boundary condition refers to a planar boundary surface. It has been used in cases where the simulation has a plane of symmetry to cut the domain into two pieces and only run the simulation on one side to reduce the running time.
- Opening boundary: location used when the flow may be into or out of the domain. The opening type boundary condition, therefore can be used where there is simultaneous inflow and outflow at a single location. It is used for the wind profile, especially when the wind direction is not parallel to the wall of the domain.

It is possible to specify a boundary condition based on the interpolated values from a data file. This option may be useful when the source term or the wind profile is interpolated from experimental data. The domain is composed of boundary conditions where different inputs are specified.

2.2.1.2 Domain size and mesh

The domain represents the volume of interest. The size may be estimated either from a coarse gird or the use of a box models. Then the domain is refined through a process to determine the numbers of elements required to obtain a grid independent solution. This practice is called grid independent test (Olvera & Choudhuri, 2006) or numerical experiments i.e. repeating the calculation on a series of successively refined gird. For a sufficiently small sizes, the rate of convergence is governed by the order of principal truncation error component (Ferziger & Peric, 1999).

2.2.1.3 Governing equations

The governing equations are solved simultaneously by using RANS. The continuity equations is (ANSYS, 2007):

$$\frac{\partial \rho}{\partial t} + \nabla \cdot (\rho U) = 0 \tag{11}$$

and the momentum equation is:

$$\frac{\partial (\rho U)}{\partial t} + \nabla \cdot (\rho U \otimes U) - \nabla \cdot \left(\mu_{eff} \nabla U \right) = -\nabla p' + \nabla \cdot \left(\mu_{eff} \nabla U \right)^T + B \tag{12}$$

where

$$\mu_{eff} = \mu + \mu_t \tag{13}$$

$$p' = p + \frac{2}{3} \rho k \tag{14}$$

μ_{eff} = the effective viscosity accounting for turbulence

μ_t = the turbulence viscosity

B = the sum of body forces

p' = the modified pressure

U = the velocity vector

ρ = the density

B = the sum of body forces

The total energy balance is:

$$\frac{\partial(\rho h_{tot})}{\partial t} - \frac{\partial p}{\partial t} + \nabla\cdot(\rho U h_{tot}) = \nabla\cdot(\lambda \nabla T) + \nabla\cdot(U\cdot\tau) + U\cdot S_M + S_E \quad (15)$$

S_E = the energy source

T = the temperature

τ = viscous stress

S_M = the momentum source

where h_{tot} is the total enthalpy, related to the static enthalpy h is function of temperature and pressure by:

$$h_{tot} = h + \frac{1}{2}U^2 \quad (16)$$

S_M and S_E are assumption in the model for source inlet in the boundary conditions. The boundary condition has an internal source term which is included in the momentum transport equations by S_E and S_M.

2.2.1.4 Turbulence model

The two-equation turbulence model k-ε, based on RANS equations, seems to be adequate for heavier-than-air gas modeling within the low atmospheric boundary layer (Sklavounos & Rigas, 2004). The values of k and ε come directly from the differential transport equations for the turbulence kinetic energy and turbulence dissipation rate (ANSYS, 2007):

$$\frac{\partial(\rho k)}{\partial t} + \nabla\cdot(\rho U k) = \nabla\cdot\left[\left(\mu + \frac{\mu_t}{\sigma_k}\right)\nabla k\right] + P_k - \rho\varepsilon \quad (17)$$

$$\frac{\partial(\rho \varepsilon)}{\partial t} + \nabla\cdot(\rho U \varepsilon) = \nabla\cdot\left[\left(\mu + \frac{\mu_t}{\sigma_\varepsilon}\right)\nabla \varepsilon\right] + \frac{\varepsilon}{k}\left(C_{\varepsilon 1}P_k - C_{\varepsilon 2}\rho\varepsilon\right) \quad (18)$$

where

$$P_k=\mu_t \nabla U\cdot\left(\nabla U+\nabla U^T\right)-\frac{2}{3}\nabla\cdot U\left(3\mu_t \nabla\cdot U+\rho k\right)+P_{kb} \quad (19)$$

$C_{\varepsilon 1}$, $C_{\varepsilon 2}$ = turbulence model constant

σ_k = turbulence model constant for the k equation

σ_ε = turbulence model constant for the ε equation

The k-ε two-equation model uses the gradient diffusion hypothesis to relate the Reynolds stresses to the mean velocity gradients and the turbulent viscosity. The turbulence viscosity is linked to the turbulence kinetic energy and dissipation using the relation:

$$\mu_t=C_\mu \rho\frac{k^2}{\varepsilon} \quad (20)$$

with

C_μ = turbulence constant

k = turbulence kinetic energy

ε = turbulence dissipation rate

The k-ε turbulence model presented in Equation (3) and (4) has default parameters for C_μ, $C_{\varepsilon 1}$, and $C_{\varepsilon 2}$ as (0.09, 1.44, 1.92). Further study showed how to tune these parameters with respect to atmospheric data. Alinot and Masson's (Alinot & Masson, 2005) study recommended using (0.033, 1.17, 1.92) instead of the default parameters for simulations less than one hundred meters above the ground. These parameters differ from the default setup because they were proven to be more accurate for the atmospheric boundary layer under various thermal stratifications (stable, neutral and unstable).

2.2.1.5 Domain reference setup

The reference parameters are defined by the acceleration due to gravity, reference pressure and reference density. A reference density value was set at 1.225 kg/m^3 at ground level (Olvera & Choudhuri, 2006). A high precision of reference density was required given the importance of significantly small density variations. The buoyant effect is driven by the gravity, and the density of the fluid. Mixing cold gas with ambient air contains important thermal effects that need to capture by the model. For LNG vapor dispersion, air and methane are usually modeled

as gas phase and their physical properties must be temperature dependent. The assumption of the using methane gas instead of LNG composition (e.g. methane and trace of heavier hydrocarbons) seems reasonable since methane will vaporize first. For instance, methane gas density must be around 1.78 kg/m^3 at 110 K to 0.45 kg/m^3 at 300 K. CFX uses the Boussinesq model to predict the turbulence inside the cloud as function of the thermal expansivity, set to 0.00366 K^{-1}:

$$\rho-\rho_{ref}=-\rho_{ref}\beta(T-T_{ref}) \quad (21)$$

where

$$\beta=-\frac{1}{\rho}\frac{\partial\rho}{\partial T}\Big|_P \quad (22)$$

with

β = the thermal expansivity,

T_{ref} = the reference temperature

ρ_{ref} = the reference density

2.2.1.6 Other considerations

The LNG flow of particular interest is located in the first hundred meters of the atmospheric boundary layer. Consequently, the Coriolis acceleration may be negligible, which may be true for most of the LNG release on land and on water (Alinot & Masson, 2005).

2.2.2 Source term

The details of the source term are presented in Figure 8 under boundary condition one. First, the scenario is determined to develop the source term. The size and geometry are setup as the surface boundary of the domain, and the gas phase velocity is specified as an inlet. The gas phase velocity is calculated from the mass evaporation rate (kg/m^2 s) by using the gas density. The literature and current consequence modeling software packages use a mean mass evaporation rate from previous validated tests. The mean value is ok for simple and box models since they do not provide an accurate three dimensional representation and they are used to obtain a conservative estimation.

Mean mass evaporation rate may not represent the evaporation phenomenon correctly. For instance, release on an open water have been proven to be more energetic resulting on locally increase of the mass evaporation (e.g. increase in gas phase velocity). Hissong (Hissong, 2007) reported an increase of the heat transfer by a factor between 8 to 10 during Esso test release on water. During large release on water, hydrate/ice formation were observed. Hydrate/Ice formation is known to influence the mass evaporation rate locally. The current consequence modeling does not account for these phenomena. Hydrate may or may not be relevant.

For the release in an impoundment (with boundary for the pool spread), as the LNG spread reaches the warm concrete, high evaporation will occur. Then overtime, as the LNG is accumulating at the bottom of the impoundment, the concrete will cool down resulting in a reduction of the heat transfer between LNG and concrete. The mass evaporation rate will be a transient function.

The initial vapor cloud height is depending on the source term and wind entrainment. Figure 10 shows the balance of the forces around the gas phase velocity as it gains altitude. In the case where the wind velocity is dominant, the upward momentum effect is diminished resulting in a vapor cloud height is low (e.g. flat cloud). When the wind velocity is low, the upward momentum is more pronounced, resulting in a high cloud height and higher gas concentration downwind. This phenomenon was observed during November 2007 test at BFTF. As the wind velocity drop, the upward momentum increases as a white cloud upward until the gravity force equalizes with the gas phase velocity force, where the cloud seem to have freeze.

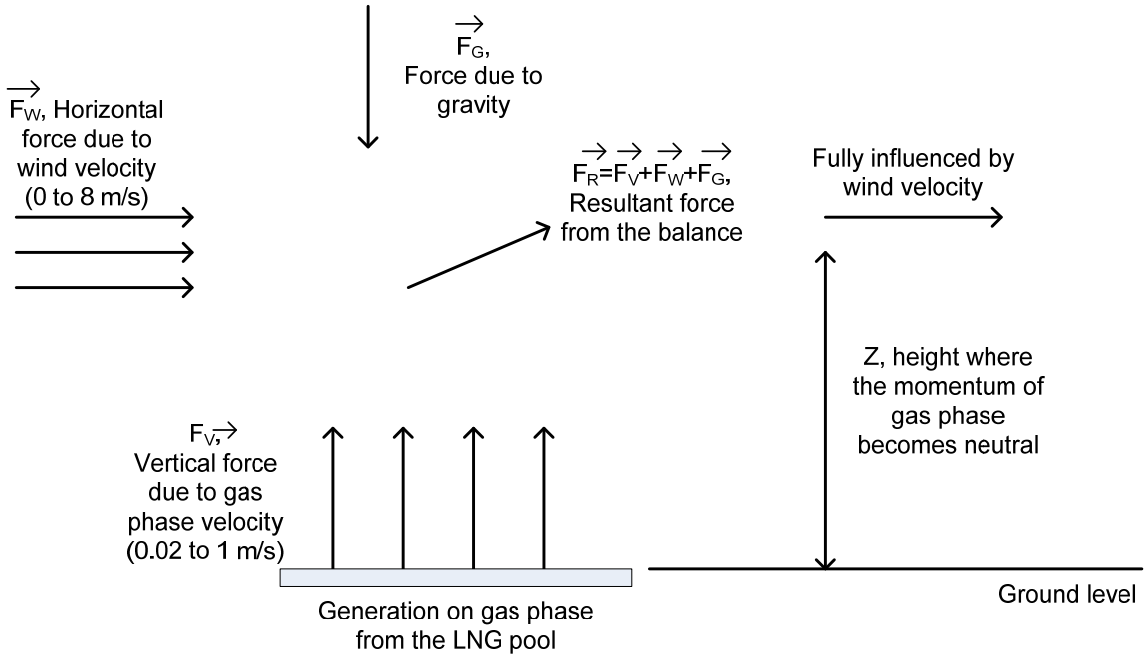

Figure 10. Balance of forces for LNG release in the estimation of the cloud height

The formation of turbulence created by evaporation phenomenon or from any external turbulence (i.e. fluid velocity, pressure release) may be modeled through the turbulence kinetic energy and dissipation energy by using the equation (Luketa-Hanlin, et al., 2007):

$$k=\frac{3}{2}\left(v_g T_i\right)^2 \tag{23}$$

and

$$\varepsilon=C_\mu^{3/4}\frac{k^{3/2}}{0.07D} \tag{24}$$

Where v_g is the mean gas phase velocity, T_i is the turbulence intensity parameter and D the relative diameter of the LNG pool. The recommended values of turbulence intensity are between 1 and 10 %.

2.2.3 Atmospheric condition

In consequence modeling, the atmospheric condition is characterized by the Pasquill-Gifford (Pasquill, 1974) stability classes (*A*-*F*) with *A* corresponding to the most unstable and *F* to

moderately stable conditions. The stability conditions are function of temperature, sensitive heat flux, roughness, wind velocity, and wind direction (negligible in the case of flat terrain). Figure 11 illustrates the atmospheric conditions for stable (*F*) and unstable (*A*) atmospheric conditions.

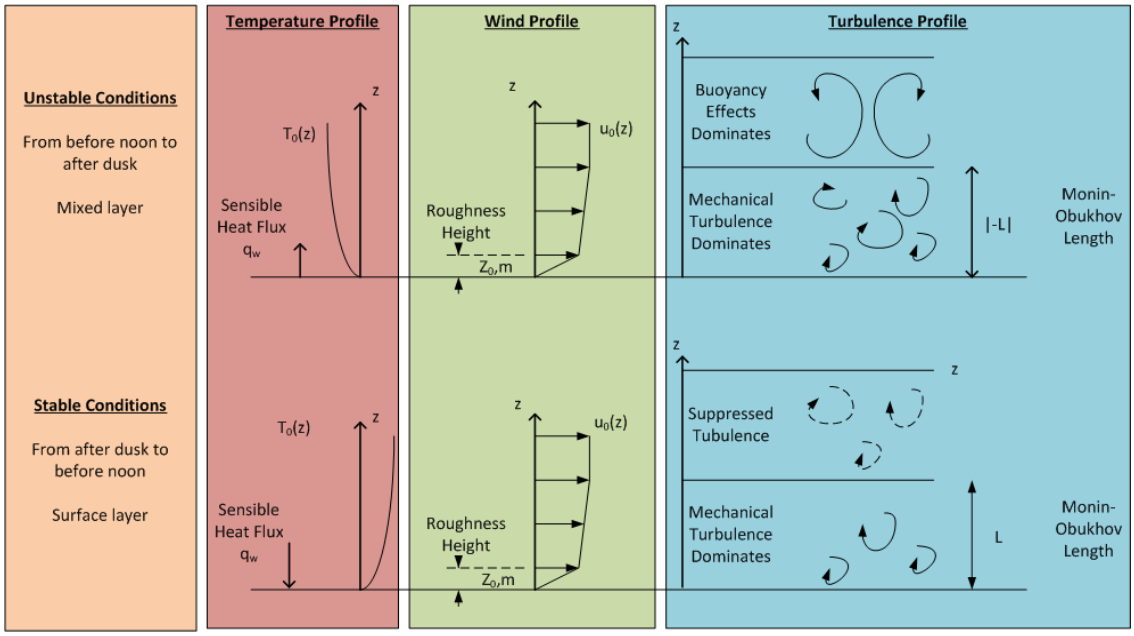

Figure 11. Atmospheric boundary layer for unstable and stable conditions(DeVaull, et al., 1995). Copyright©1995 by the Center for Chemical Process Safety of American Institute of Chemical Engineers and reproduced by permission of AIChE. This figure is from DeVaull, G. D., King, J. A., Lantzy, R. J., & Fontaine, D. J. (1995). *Understanding atmospheric dispersion of accident releases.* New York: Center for Chemical Process Safety.

Unstable conditions occur during the day as the ground is heated by the sun. The warm ground leads to unstable density stratification. This thermal effect leads to high vertical mixing rates, i.e. rapid dilution of the chemical in the atmosphere. Neutral atmospheric condition occurs in the evening when the heat transfer from the ground is very small, nearly zero. During a stable stratification, the convection and conduction cools the atmospheric boundary layer leading to limited vertical mixing rates in the atmosphere, i.e. the dilution is minimal and usually happens during the night.

The Monin-Obukhov length demarcates the height below which mechanically generated turbulence dominates in the mixing process, shown in Figure 11. The Monin-Obukhov length is negative for unstable conditions, positive for stable conditions and infinite for neutral conditions.

The atmospheric conditions may be modeled by using an atmosphere boundary layer model related to Monin-Obukhov length. This model predicts temperature, wind velocity, atmospheric stability, and turbulence for the domain. To express the atmospheric conditions based on Monin-Obukhov length (Brown, et al., 1990), the wind velocity, $u_0(z)$, and temperature, $T_0(z)$, may be derived as function of vertical z-axis:

$$u_0(z)=\frac{u_*}{k}\left[log_e\left(\frac{z}{z_0}\right)-\psi_m\left(\frac{z}{L}\right)\right] \quad (25)$$

$$T_0(z)=T_w+\frac{T_*}{k}\left[log_e\left(\frac{z}{z_0}\right)-\psi_h\left(\frac{z}{L}\right)\right] \quad (26)$$

when $L > 0$

$$\psi_m\left(\frac{z}{L}\right)=\psi_h\left(\frac{z}{L}\right)=-5\frac{z}{L} \quad (27)$$

$$\phi_m\left(\frac{z}{L}\right)=\phi_h\left(\frac{z}{L}\right)=1+5\frac{z}{L} \quad (28)$$

when $L < 0$

$$\psi_m\left(\frac{z}{L}\right)=2log_e\left[\frac{1+x}{2}\right]+log_e\left[\frac{1+x^2}{2}\right]-2tan^{-1}(x)+\frac{\pi}{2} \quad (29)$$

$$\psi_h\left(\frac{z}{L}\right)=2log_e\left[\frac{1+x^2}{2}\right] \quad (30)$$

$$\phi_m\left(\frac{z}{L}\right)=\frac{1}{x} \quad (31)$$

$$\phi_h\left(\frac{z}{L}\right)=\frac{1}{x^2} \quad (32)$$

with

$$x=\left(1-\frac{16z}{L}\right)^{1/4} \quad (33)$$

L = the Monin-Obukhov length

z = the vertical coordinate (z=0, at the ground level)

z_0 = the surface roughness

g = the acceleration of gravity

k = the von Karman constant

The parameters in the wind and temperature equation (i.e. (25) and (26)) have the following parameters derived from the historical data:

$$L=\frac{u_*^2 T_w}{KgT_*} \tag{34}$$

and

$$T_w=T_a\left(\frac{P_0}{P}\right)^{\mu} \tag{35}$$

u_* = the turbulence friction velocity

T_w = the zero level potential temperature

T_* = the scaling potential temperature

T_a = the ambient temperature

The sensible heat flux is defined from the estimated variables as well:

$$\dot{q}_w=T_*\rho_{air}C_{Pair}u_* \tag{36}$$

with

$\dot{q}_w$ = the sensible heat flux

C_{Pair} = the heat capacity of air

ρ_{air} = the density of air

The momentum diffusivity and the heat diffusivity are estimated from the equations:

$$K_m(z)=\frac{u_*kz}{\phi_m(z/L)} \tag{37}$$

$$K_h(z) = \frac{u_* kz}{\phi_h(z/L)} \tag{38}$$

where the Richardson number is defined and calculated from the same functions:

$$R_i\left(\frac{z}{L}\right) = \frac{\frac{z}{L}\cdot\phi_h\left(\frac{z}{L}\right)}{\phi_m^2\left(\frac{z}{L}\right)} \tag{39}$$

The turbulence kinetic and energy dissipation term may be expressed in function of the Monin-Obukhov length as well (Panofsky & Dutton, 1984):

$$\epsilon_0(z) = \frac{u_*^3}{Kz}\phi_h\left(\frac{z}{L}\right) \tag{40}$$

$$k_0(z) = 5.48u_*^2\left[\frac{\phi_h\left(\frac{z}{L}\right)}{\phi_m\left(\frac{z}{L}\right)}\right]^{\frac{1}{2}} \tag{41}$$

where the constant 5.48 has been experimentally determined for neutral atmospheric layer (Panofsky & Dutton, 1984)

2.2.4 Ground effects

The ground effect is characterized by the obstacles geometry that may affect the simulation. Each surface may have a different heat flux (or temperature) respect to the sun exposure, and surface roughness. The ground effect may be also significant for free obstacles simulation. For more complex scenario, obstacles are represented by geometry shape where a surface roughness or/and temperature may be set. Petersen study (Peterson, 1990) showed that effect of large homogeneous roughness may significantly reduce the concentrations downwind. Heterogeneous roughness, when the surface roughness changes as the features of the terrain changes (i.e. from concrete to grass), may have also an effect on the concentration downwind. The roughness effect on the wind profile is described in Figure 12.

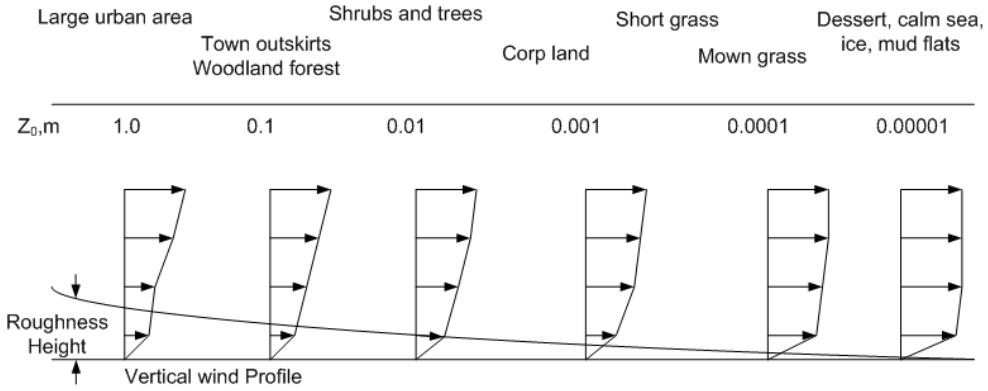

Figure 12. Roughness description(DeVaull, et al., 1995).

2.3 Available models and their limits

The dispersion mechanisms are described with respect to each model below. Different approaches were used over the years and there are three broad classes of models for dense gas dispersion:

1. Modified conventional models
2. Box and slab models (one-dimensional integral models)
3. Navier-Stokes-based models: Finite element modeling (three-dimensional models)

2.3.1 Modified conventional models

The Germeles-Drake model (Ermak, et al., 1982) is derived from the steady state, Gaussian plume model, point source solution to atmospheric advection diffusion equation. This equation includes the change of concentration respect to x, y, z, and time:

$$\frac{\delta c}{\delta t} + U\frac{\delta c}{\delta x} = K_y\frac{\delta^2 c}{\delta y^2} + K_z\frac{\delta^2 c}{\delta z^2} \qquad (42)$$

where

c = concentration of the emitted species

U = the wind velocity, assumed to be constant in x-direction

K_y = horizontal turbulence diffusivities

K_z = vertical turbulence diffusivities

The turbulence diffusivity with respect to *x* is neglected because it is negligible compared to the turbulence due to the wind. The equation for the concentration of methane vapor is obtained by integrating the previous equation over a finite line source.

The atmospheric conditions effects are derived from the dispersion coefficients, which are based on the Pasquill-Gifford dispersion coefficients. The source length and the virtual distance are determined by the gravity spread calculation on a cylindrically shaped volume of LNG vapor equal to the volume evaporated in the time it takes for the wind to traverse the liquid pool.

The source term is defined with an initial height (H_i) of the cylindrical cloud is

$$H_i = \frac{2R_i W_v}{U} \tag{43}$$

where W_v is the vapor source velocity (considered uniform) and R_i is the initial radius. The properties of the cylindrical cloud are assumed to be homogeneous. The height, radius, temperature, and density change with time due to three processes: gravity spread of the denser-than-air cloud, air entrainment into the cloud, and surface heating of the cloud. The radius, *R*, of the cylinder is calculated with the gravity spreading:

$$\mathrm{R} = \left[2g\frac{(\rho-\rho_a)}{\rho_a}H\right]^{1/2} \tag{44}$$

where

g = the acceleration due to gravity

ρ = the cloud density

ρ_a = the ambient air density

Most of these equations are solved with the time independent ideal gas law and as function of time. The first model developed for vapor dispersion was the Gaussian puff/plume model.

2.3.2 Box and SLAB models: one-dimensional integral models

Because of the unsuccessful modeling of negative buoyancy vapor clouds by using modified Gaussian models, the need for a new approach was required. The release of a heavier-than-air gas in the atmosphere has three stages: negative buoyancy-dominated dispersion, stable stratified shear flow, and passive dispersion. All stages must be integrated into the model to simulate it successfully.

2.3.2.1 Box modeling: Dense Gas DISpersion (DEGADIS)

DEGADIS was developed by Jerry Havens, et. al. at the request of USCG (Spicer & Havens, 1986). DEGADIS is a dense gas dispersion model that predicts the ground level dispersion. As discussed previously, a heavier-than-air gas goes through three stages. The Richardson number is used to determine what stage is dominant. By using the following equation:

$$R_i = \frac{g}{U_*^2}\left(\frac{\rho-\rho_a}{\rho_a}\right)\left(\frac{\dot{M}}{\rho U D}\right) \tag{45}$$

with

$R_i \leq 1.0$ Release essentially passive from the source i.e., passive dispersion

$1.0 \leq R_i \leq 30$ No significant lateral spreading i.e., stably stratified shear flow

$R_i \geq 30$ Significant upstream spreading i.e., dense gas dominant

DEGADIS is an adaptation version of the Shell HEGADAS model (Witlox, 1994) and incorporates some techniques used by Van Ulden.

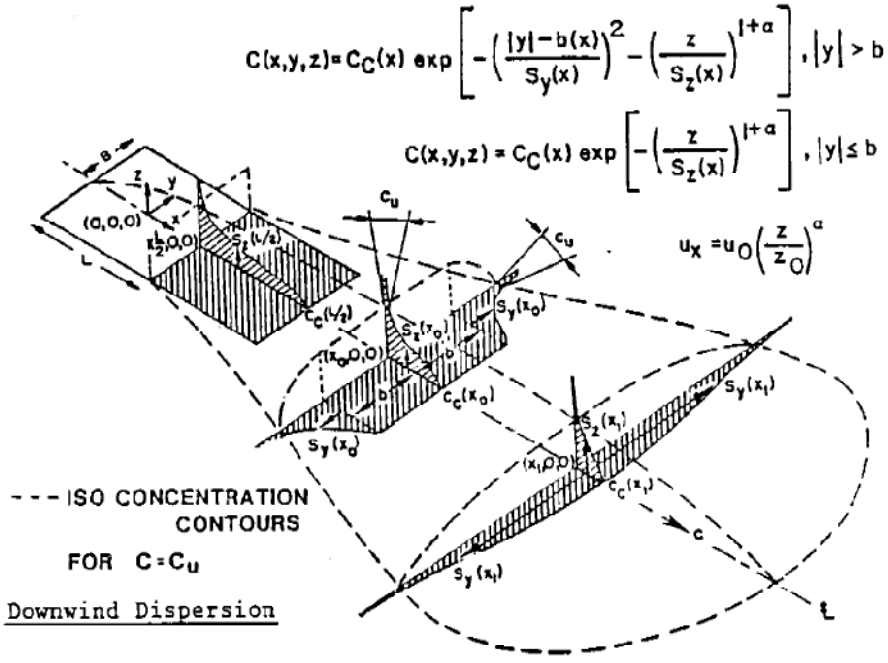

Figure 13. Vapor modeling in DEGADIS (Spicer & Havens, 1987).

This figure was reproduced by permission from Spicer, T. O., & Havens, J. A. (1987). Field test validation of the DEGADIS model. *Journal of Hazardous Materials*, *16* (1987), 231-245.

DEGADIS is divided into three different codes for each regime with respect to Richardson number. The negative buoyancy dispersion phase is based on experimental data from a laboratory release performed by Havens and Spicer(Spicer & Havens, 1986). For the stably stratified shear flow phase, it also is modeled from experimental laboratory data. Established passive atmospheric dispersion modeling principles are used for the passive dispersion phase (i.e., Gaussian modified). The concentration profile used the two first equations illustrated in Figure 13. The wind profile is developed with the following equations, where α is evaluated from the stability conditions, also illustrated in Figure 13.

The source model represents an averaged concentration of gas present over the primary source, while the downwind dispersion phase of the calculation is shown in Figure 14. A secondary source is created on top of the initial source for the vapor dispersion model shown in

Figure 13. The near field buoyancy regime is modeled by using a lumped parameter model of a denser-than-air gas "secondary source" cloud which incorporates air entrainment at the gravity spreading front using a frontal entrainment velocity. The downwind dispersion phase assumes a power law concentration distribution in the vertical direction and a modified Gaussian profile in the horizontal direction with a power law specification for the wind profile.

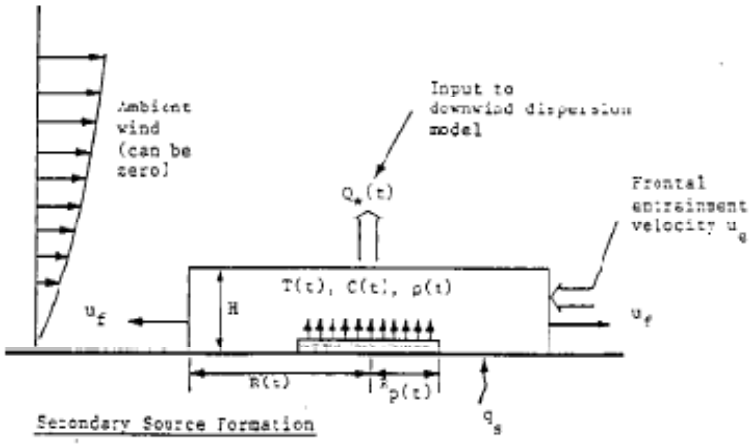

Figure 14. Source modeling in DEGADIS (Spicer & Havens, 1987, Spicer & Havens, 1989).

This figure was reproduced by permission from Spicer, T. O., & Havens, J. A. (1987). Field test validation of the DEGADIS model. *Journal of Hazardous Materials*, *16* (1987), 231-245.

2.3.2.2 Slab modeling: SLAB

The SLAB model treats the dispersion of dense gas as a well-defined cloud of height *h* and a half width *B* as shown in Figure 15.

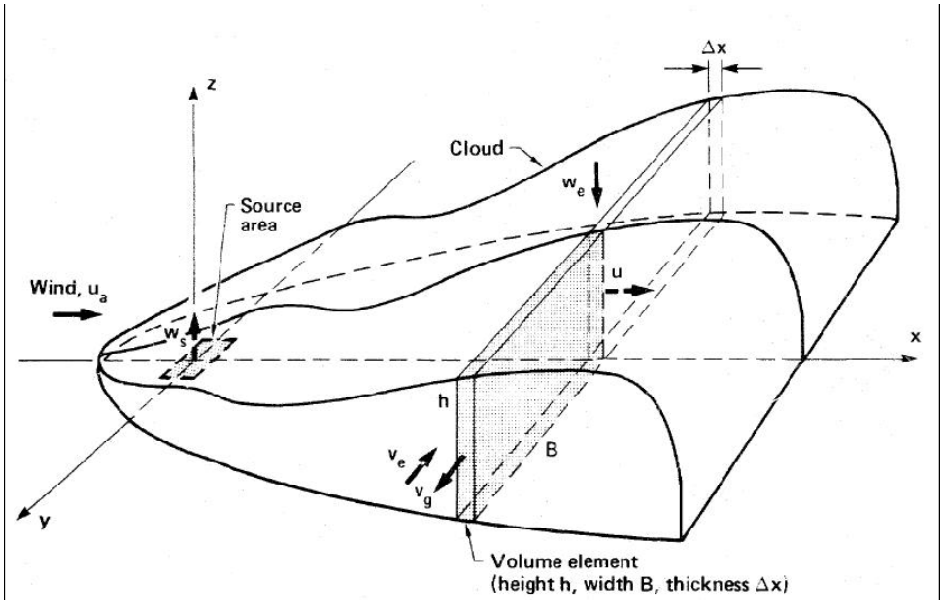

Figure 15. Depiction of a dispersing cloud of heavy gas and air assumed by SLAB model (Ermak, 1990). Credit must be given to the LLNS, Lawrence Livermore National Laboratory, and the Department of Energy under whose auspices the work was performed, when this information or a reproduction of it is used.

The inside properties are considered to be uniform in the crosswind plane so that they vary only with time and in the distance downwind. This assumption allows the cloud to be described in terms of slab or layer-averaged properties for the cloud density with:

$$\bar{\rho}(x)=\frac{1}{Bh}\int_0^B dy \int_0^h dz\rho(x, y, z) \qquad (46)$$

Therefore, it is justified to approximate the average of the product as equal to the product of the average. The above assumption and approximation are used to derive the layer-averaged conservation equations for mass (46), vapor (47), momentum (48 and 49) and energy (equation 50). These equations, along with a rate equation for the cloud half-width (51), are:

$$\frac{\delta(\rho Bh)}{\delta t}+\frac{\delta(U\rho Bh)}{\delta x}=\rho_a v_e h+\rho_a w_e B+\rho_s w_s B_s \quad (47)$$

$$\frac{\delta\omega}{\delta t}+U\frac{\delta\omega}{\delta x}=\frac{\rho_a v_e \omega}{\rho B}+\frac{\rho_a w_e \omega}{\rho h}+\frac{\rho_s w_s B_s(1-\omega)}{\rho Bh} \quad (48)$$

$$\frac{\delta U}{\delta t}+U\frac{\delta y}{\delta x}=-\frac{g}{2\rho Bh}\frac{\delta[(\rho-\rho_a)Bh^2]}{\delta x}+\frac{\rho_a}{\rho}\left[\frac{v_e}{B}+\frac{w_e}{h}\right](U_a-U)-\frac{\rho_s W_s B_s U}{\rho Bh}-\frac{\tau_x}{\rho h} \quad (49)$$

$$\frac{\delta V_g}{\delta t}+U\frac{\delta V_g}{\delta x}=\frac{gh}{\rho B}(\rho-\rho_a)-\frac{\rho_a}{\rho}\left(\frac{v_e}{B}+\frac{w_e}{h}\right)V_g-\frac{\rho_s W_s B_s V_g}{\rho Bh}-\frac{2\tau_x}{\rho h} \quad (50)$$

$$\frac{\delta T}{\delta t}+U\frac{\delta T}{\delta x}=\frac{\rho_a}{\rho C_p}\left(\frac{v_e}{B}+\frac{W_e}{h}\right)(T_a-T)+\frac{\rho_s C_{pn} W_s B_s(T_s-T)}{\rho C_p Bh} \quad (51)$$

$$\frac{\delta B}{\delta t}+U\frac{\delta B}{\delta x}=V_g+v_e \quad (52)$$

where

g = the acceleration due to gravity

C_p = the heat capacity

h = the height

B = the haft-width

ρ = the average density

ω = the mass fraction

U = the velocity in the direction of the wind

T = the temperature

V_g. = the crosswind velocity

W_e = the vertical entrainment

V_e = the horizontal entrainment

j = the surface heat flux

τ = the surface momentum flux

with the subscript "s","a", and "n" for source, ambient, and natural gas properties. The vertical entrainment was modified from the Zeman rate equation (Zeman, 1979, Zeman & Lumley, 1976) to integrate the density-weighted combination of an ambient air entrainment rate, a stably stratified dense layer entrainment rate and horizontal entrainment. These equations (six

nonlinear partial differential equations, PDE) are coupled together and solved. SLAB software was developed by Ermak (Brown, et al., 1990).

2.3.2.3 Other models

There are other models for vapor dispersion modeling. One-dimensional integral models such as SLAB (Lakes Interface), DEGADIS (code integrated in AHOLA®), Canary (Quest), Cirrus (BP), PHAST (DNV) and Fred (old HEGADAS) (Witlox, 1994) may model either buoyancy, neutral, or stably stratified as well jet release. A shortcoming of these models is that they cannot model flow around obstacles or over a complex terrain. DEGADIS(Havens, 1988), SLAB(Brown, et al., 1990) and PHAST are widely used in the public and private sector because of the fast computational time and ease of use. Several papers were published on comparing the model types described in the previous sections against experimental data, such as Hanna et al. (Hanna, et al., 1993). Ermak (Ermak, et al., 1982), Alp(Alp, et al., 1985), and Kakko(Kakko, 1991).

2.3.3 Navier-Stokes based models: finite element

In the open literature, there are four distinct CFD codes that may be used for LNG vapor dispersion modeling, FEM3 CFD(Luketa-Hanlin, et al., 2007), FLACS (Dharmavaram, et al., 2005, Hanna, et al., 2004), FLUENT(Gavelli, et al., 2006) and CFX(Sklavounos & Rigas, 2004). CFX and FLUENT are general-purpose CFD code, and it is not calibrated for the solution of specific problem like FEM3 CFD or FLACS which specifically designed to model vapor dispersion. The use of a generic CFD code was more appropriate for this type of work because of the flexibility in the setting of the model. For the vapor model dispersion, CFX uses the Reynolds Averaged Navier-Stokes (RANS) equations and is based on the finite volume method for the conversion of partial differential equations and auxiliary conditions into a discrete system of equations.

This model is associated with CFD models. FEM3 CFD, FLUENT, and CFX are based on RANS. This approach may be used with a finite element method to estimate the profile of the cloud in a three-dimensional configuration. In this section, the instantaneous equation of mass, momentum, and energy conservation are presented. For turbulent flows, the instantaneous equations are averaged leading to additional terms. The instantaneous equations of mass, momentum and energy conservation can be written as follows in a stationary frame. The governing equations are shown by Equation (11-15).

2.3.3.1 FEM3 CFD

FEM3 CFD model was initiated in 1979 to develop a validated computer model for simulating gravitational spread and vapor dispersion that results from a release into atmosphere. FEM3 CFD is the first three-dimensional computer model that was designed for simulating the atmospheric dispersion of heavy gas releases such as LNG. This model uses a modified Galerkin finite element method that is capable of solving the time-dependent conservation equations of mass, energy, momentum and species together with the ideal gas law for the density of the gas/air mixture. This model also includes sub-models for the source, ground heat transfer and K-theory sub-model for turbulence. These sub-models provide a mathematical description of the physical for heavy gas dispersion including gravity spread, the effect of density stratification on turbulent mixing and ground heating of the gas cloud. FEM3 can treat complex flow and dispersion scenarios over variable obstacles. The FEM3 CFD model solves the following three-dimensional, time-dependent conservation equations (Chan, 1997). The anelastic approximation assumes that the compressibility effects are negligible since the Match number is always very small. FEM3 CFD treats turbulence by using a k-theory local equilibrium model, in which the turbulence model is modified by a cold, dense cloud in high concentration regions. Three diffusivity tensors are assumed to be diagonal. The vertical diffusion coefficient is a function of the sum of the ambient vertical diffusivity and dense-layer diffusivity. The atmospheric conditions are characterized by the diffusivity and the wind velocity profile. The software is composed of three parts, pre-fem3a, fem3a and post analysis (independent software). The code is written in Fortan77. The input is based on a text file and there is no interface for the user.

2.3.3.2 CFX-11.0

CFX is a general-use CFD code, and it is not calibrated for the solution of specific problems like FEM3 CFD, which is specifically designed to simulate LNG. However, CFX has been validated for several heavy gas dispersions (Sklavounos & Rigas, 2006). CFX code is composed of three parts: preprocessor, solver and post-processor for problem definition, problem solution and results processing as described in Figure 8. CFX had shown good results in the cryogenic release in atmosphere from Sklavounos and Rigas (Sklavounos & Rigas, 2005). The authors showed the

results of their CFX model against LNG and hydrogen trials. Even through the release trails were performed over the flat terrain, the results were in agreement with the historical data.

The two first sub-models are used to define the problem, and then the rest of the sub-model t is used in getting a solution and analysis. For the vapor model dispersion, CFX uses the RANS equations and is based on a finite volume method for the conversion of partial differential equations and auxiliary conditions into a discrete system of equations.

2.3.3.3 FLUENT

FLUENT (Gavelli, et al., 2006) like CFX is a general purpose CFD code, and not a consequence model. The extra step to setup the simulation with the parameters and particular boundary conditions specific to consequence modeling is required.

2.3.3.4 FLACS

FLame ACeleration Simulator (FLACS) (Dharmavaram, et al., 2005) is a CFD consequence model like FEM3 CFD, all the inputs are already specified to consequence modeling.

2.4 LNG release experiments and data

Over the past thirty years, a substantial amount of data has been made available from the tests performed by different entities. These entities are listed below; however their data was not usable for this work. This section presents a survey of the LNG experiment data. Only data relevant to LNG is presented in detail in this section. The data may be divided into two sets: continuous releases and instantaneous releases.

- Bureau of Mines 1970 (Burgess, et al., 1970)
- Matagordo, Esso 1971(Feldbauer, et al., 1972, May, et al., 1973)
- Bureau of Mines/AGA 1972 (Burgess, et al., 1972)
- Bay Nantes, Gaz de France 1972(Humbert-Basset & Montet, 1972)
- Shell “Gadila” Tests 1973(Kneebone & Prew, 1974)
- Capistrano, AGA LNG test program 1974(1974)
- Avocet, Lake China 197 (Meroney & Neff, 1982)

2.4.1 Burro series 1980 (Koopman, et al., 1982)

The Burro tests were performed by Lawrence Livermore National Laboratory (LLNL) at the Naval Weapons Center (NWC), China Lake, California and sponsored by the DOE and the Gas Research Institute. These tests were classified as continuous releases. This series involved eight release of LNG and one release of liquid nitrogen onto water. These releases were approximately 40 m^3. A large array of equipment was used including gas, temperature, heat flux, humidity, and turbulence sensors. The facility at China Lake was updated from a storage capacity from 5.7 m^3 to 40 m^3 for the purpose of this series. The release was onto a pond of water. The size of the pond was about 10,000 m^2. This surface gave enough space for the LNG layer to spread onto water from a 25-cm diameter release line. A large array of gas-sensing and wind-measuring was deployed around the site. This instrumentation array expanded up to 900 meters on the prevailing wind direction and 800 meters on the opposite directions. Only wind field anemometer stations were installed in the upwind direction to measure the wind behavior. The operating pressure was 2.4 bars and the approximate flow rate was 11.3 to 18.4 m^3/min. Table 4 shows the Burro Series test summary. Burro 1 was a liquid nitrogen release, which is not included here.

Table 4. Burro series test summary (Koopman, et al., 1982)

Test Name	*Release Volume (m^3)*	*Release Rate (m^3/min)*	*Average Wind velocity (m/s)*	*Atmospheric Stability*
Burro 2	34.3	11.9	5.4	C
Burro 3	34.0	12.2	5.4	C
Burro 4	35.3	12.1	9.0	C
Burro 5	35.8	11.3	7.4	C
Burro 6	27.5	12.8	9.1	C
Burro 7	39.4	13.6	8.4	C/D
Burro 8	28.4	16.0	1.8	E
Burro 9	24.2	18.4	5.7	D

2.4.2 Maplin Sands 1980 (Puttock, et al., 1982)

In 1980, tests were conducted at Maplin Sands, England by the National Maritime Institute and were sponsored by Shell. The main purpose of these tests was to obtain data for dispersion

and radiation due to fire from 20 LNG releases and 14 propane releases. The release of LNG was underneath of the water. LNG was released onto seawater from a pipeline terminating in a downwards-pointing pipe. Measurements were taken by instruments located on pontoons placed in arcs around the point release. Two trials were carried out, one with liquefied propane gas (LPG) and one with LNG. Most of the tests were continuous releases. Thirteen continuous LNG releases were performed presented in Table 5.

Table 5. Maplin Sands test summary (Puttock, et al., 1982)

Trial Number	*Volume (m^3)*	*Rate (m^3/min)*	*Duration (s)*	*Wind velocity (m/s)*
Continuous LNG release				
9	-	1.6	300	8.9
12	-	0.7-1.1	340	1.5
15	-	2.9	285	3.6
27	-	3.2	160	5.5
29	-	4.1	225	7.4
34	-	3.0	95	8.6
35	-	3.8	135	9.8
37	-	4.1	230	4.7
39	-	4.7	60	4.1
56	-	2.5	80	5.1
Instantaneous LNG release				
22	12	-	-	5.5
23	8.5	-	-	6.6

2.4.3 Coyote series 1981(Goldwire, et al., 1893)

Coyote Series tests were performed at China Lake. The setup was the same as the Burro test series presented earlier; however, more equipment was added to the array. The main purpose of this test series was to study the RPT. Partial data is available for vapor dispersion modeling presented in Table 6.

Table 6. Coyote series test summary(Goldwire, et al., 1893)

Test Name	*Release Volume (m^3)*	*Release Rate (m^3/min)*	*Average Wind velocity (m/s)*	*Atmospheric Stability*
Coyote 3	14.6	13.5	6.0	C
Coyote 5	28.0	17.1	9.7	C
Coyote 6	22.8	16.6	4.6	D

2.4.4 Falcon series 1987(Shin, et al., 1991)

The Falcon Tests were performed at the Frenchman Flat in Nevada by LLNL and sponsored by Gas Research Institute and Department of transportation (DOT). The objectives were to obtain a set of data for vapor dispersion involving an obstacle and study of the effectiveness of this barrier. The data available is presented in Table 7.

Table 7. Summary of Falcon series test(Shin, et al., 1991)

Trial Number	*Volume (m3)*	*Rate (m3/min)*	*Wind velocity (m/s)*
Falcon 1	66.4	28.7	1.7
Falcon 2	20.6	15.9	4.7
Falcon 3	50.7	18.9	4.1
Falcon 4	44.9	8.7	5.2
Falcon 5	43.9	30.3	2.8

2.5 Simulation work

The first approach to model dense gas was to modify conventional models, based on the conservation of species equation and use of an ad hoc equation to estimate the downwind profile. Even though the Gaussian model was modified, it was not suitable for dense gas modeling. Ermak, et al. demonstrated that the modified Gaussian model was not suitable for negative buoyancy vapor cloud (Ermak, et al., 1982). Cox's work also demonstrated the need for negative buoyancy models (Cox, 1980).

From the failure to represent dense gas phenomena with modified Gaussian models, new models were required to be developed to assess LNG vapor dispersion. Hence, DEGADIS and SLAB were then developed. Most of these models are in agreement with the experimental data available for releases into the atmosphere with a flat terrain(Hanna, et al., 1993). These models become obsolete when the simulation required assessment of obstacles. The first model capable to assess the obstacles was FEM3 CFD, which was modified from the FEM3 CFD presented. FEM3 CFD accounts for more atmospheric phenomena than the box-model prediction(Chan, 1997). For instance, all these software packages, including CFD, include dense gas effects with atmospheric boundary layer, non smooth surfaces, and heat transfer. But CFD also accounts for vapor holdup with a dike or vapor fence with 2^{nd} order closure, obstacles (non-uniform) with heights greater than cloud depth and for terrain effects on cloud path as well as dispersion. FEM3 CFD is used by LLNL (Brown, et al., 1990, Chan, 1992, Ermak, et al., 1982) and Jerry havens (Havens & Spicer, 2005, Havens, et al., 1994, Havens, et al., 2004). Manuals and updated literature (Chan, 1983, Chan, 1984, Chan, 1994, McCallen, 1988) are available. Only research organizations use this software effectively (e.g., Ohba paper(Ohba, et al., 2004), LLNL, and MKOPSC (Cormier, et al., 2006)).

A few years after the development of FEM3 CFD, LNG became less attractive resulting in a slowdown in the development of FEM3 CFD in early 1980. Today, due to high price in energy, LNG reemerged as an attractive resource. New CFD modeling such as FLEUNT and CFX has proven to be viable for other areas of research. Recently, FEM3 CFD was presented in a paper from Luketa-Hanlin, to illustrate the capability for FEM3 CFD(Luketa-Hanlin, et al., 2007). The validation presented in this paper for FEM3 CFD was from the previous work. The FEM3 CFD validation covers Burro(Ermak, et al., 1982), Thorney island(Chan, et al., 1987) and Falcon(Chan, 1990).

Sklavounos and Rigas' work (Sklavounos & Rigas, 2005, Sklavounos & Rigas, 2006, Sklavounos & Rigas, 2004) used CFX as air dispersion modeling and compared it with experimental data. They compared CFX's capability with LNG and hydrogen releases in the atmosphere. The model showed a general good agreement with the experimental data. The model was tested against obstacle-free experimental data.

Gavelli published simulation results using FLUENT (Gavelli, et al., 2008, Gavelli, et al., 2006). His results show the real capability of using CFD incorporating obstacles. The first paper in 2006 was about simulation involving impoundment and the second paper compared Falcon experimental data for a vapor fence. In both cases, the simulation shows good relationship to the experimental data.

FLACS was developed in the early 1980's. Like FEM3 CFD, FLACS is software specifically developed for consequence modeling. It was originally developed for explosion prediction for the off-shore industry. As with the codes for CFD, FLACS uses conservation equations for mass, energy, and momentum with a Cartesian grid using the finite-volume method. FLACS also uses the two-model turbulence equation, k and epsilon. The atmospheric boundary layer is based on Monin-Obukhov length. Several validation studies have been done for explosion calculations and dispersion (Dharmavaram, et al., 2005, Hanna, et al., 2004))

2.6 Gaps

A literature review had been performed to better understand the current state of LNG vapor dispersion modeling research. Studying the current models also helped identify the gaps in the current work and key parameters needed to improve these models. After reviewing LNG vapor dispersion modeling literature, it primarily fell into two different categories, source term and vapor dispersion. It was essential to study both phenomena to understand the overall process.

The literature review revealed a new interest in CFD models rather than "box" models for consequence modeling mainly due to the need to assess complex scenarios. The assessment of complex scenarios requires a three-dimensional capability. The consensus of the literature was that CFD modeling has strong capabilities as an impact assessment tool for chemical releases in complex urban scenarios under atmospheric conditions. Even though the use of CFD is becoming more widely accepted, there is no study on the sensitivity of the key parameters. Most of the research for LNG vapor dispersion modeling (including CFD) has been focused either on the vapor dispersion or the source term as two separate problems. The literature review also showed an over-simplification of the source term in the vapor dispersion. The current source term in vapor dispersion is represented as a mean upward gas phase velocity, excluding all the turbulence effects. This over-simplification limits the range of validity for the

current consequence modeling. The methodology for this research was (i) to refine the source term (ii) to incorporate it into the vapor dispersion.

The second objective of this research is to provide a workable version of a CFD model reachable by industry specifically for LNG vapor dispersion behaviors. The benefit of CFD is not only an improved source term but also the introduction of obstacles such as dike or storage tank. The combination of optimization methods and consequence modeling will be a useful tool to industry. This tool will be important for supporting decision making in facility siting because it has the ability to accommodate all types of obstructions. A working model will help industry implement the use of CFD models for consequence models in daily engineering life.

2.6.1 Source term

The first remark is, as a big picture, LNG vapor cloud should include source modeling to obtain a better definition of the source term. The literature review also reveals a certain uncertainties in the estimation of boil off rate. Table 8 summarizes the difference in the estimation of evaporation rate for LNG release onto unconfined water space from different well-recognized sources.

Table 8. Evaporation rate for LNG release onto unconfined water

Source	*Mass evaporation rate kg/m^2 s*	*Estimation/Conditions*
Bureau of Mines(Burgess, et al., 1970)	0.181	Pond scale
Bureau of Mines(Burgess, et al., 1972)	0.155	Pond scale
Shell Ltd(Hightower, et al., 2004)	0.024 to 0.195	Laboratory scale
Esso(Hightower, et al., 2004)	0.195	Matagorda bay
Burro(Hanna, et al., 1991)	0.085	Visual estimation
Ospchoor (Opschoor, 1977)	0.04 and 0.17	Theoretical values
DNV(PHAST)(Baik, et al., 2006)	0.182	Software
ABS(Baik, et al., 2006)	0.072	Software
Quest(Baik, et al., 2006)	0.2	Software

Even though the available literature showed significant progress with the CFD model in consequence modeling with dense gas, the current methodology only has a narrow range of validity against experimental data. This may be due to the poor definition of the source term in the vapor dispersion modeling. The source term only is modeled with a mean evaporation rate

over time (in the transient case) or a constant mean value (in the continuous case) with pool geometry (usually a circle) or a point source. The typical values of mean evaporation velocity are between 0.08 to 0.10 m/s (using $\rho_{LNG(110K)}$: 1.78 kg/m^3 for 0.15 to 0.185 kg/m^2 s). These mean values do not reflect the turbulence created during the release, fluid velocity or the flashing effects. Hissong reported that it may increase the evaporation rate by a factor of 8 to 10. In other words, the evaporation velocity may be as high as 0.8 to 1 m/s at the release area. Gavelli reported from the analysis of the Falcon series (Gavelli, et al., 2008), the gas phase velocity calculated to be 6.3 m/s at the release point (compare to 0.1 m/s for recommended value). The research approach was to study the gas phase velocity of the pool by performing testing of LNG released onto water. The gas phase velocity may be obtained by investigating the heat transfer through the water, the gas cloud formed about the water, and pool area for a released volume. The pool area for a release volume consists of measuring the area of the pool and the liquid flow rate during a release. This will give mean values of the evaporation rate at a given time. The measurement of the heat transfer through the water gives the heat flux profile from the cryogenic pool to the water. Thermocouples placed in the water at different heights provide measurements of the heat flux through the water. A mass evaporation rate may be estimated from the heat flux for any location at a given time.

This physical effect of high localized gas velocity may be also diminished for medium to high wind velocities, where current models usually obtain the validation. The case where the wind velocity is low, this data may be the key. For instance during Burro 8, the wind velocities were relative low (mean value of 1.8 m/s, and from 1 to 3.5 m/s over the historical time). The gas phase velocity may have strong consequences on the vapor dispersion modeling as shown in Figure 10. The low wind velocity may increase the effect of gas phase velocity until the wind entrains the vapor. Burro 8 showed high concentrations, up to 40-45% of methane as compared to 15-20 % with other tests (Koopman, et al., 1982).

The Falcon series had interesting source term issues (Brown, et al., 1990). The Falcon series had a pond inside of a vapor fence where LNG was released onto water with a fluid velocity near of 60 m/s and with a wind velocity from 1.7 to 5.2 m/s. The wind velocity had a limited

effect on the release area since it was surrounded by the vapor fence. As the wind velocity was reduced, the concentration levels downwind were higher.

2.6.2 Vapor dispersion

Another area of consensus in the literature review was that CFD modeling is the next, if it is not already, accessible tool for consequence modeling and risk assessment. As of today, there are several software packages commercially available: FEM3 CFD, FLACS, FLUENT, STAR-CD(Olvera & Choudhuri, 2006), and CFX. After reviewing most of the papers regarding LNG vapor dispersion, FEM3A seems to have the widest range of validity for the models presented. FEM3 CFD is a code for consequence modeling for chemical releases, especially LNG, but like any other software, it has limits. FEM3 CFD was developed as a research tools and it never become to be used intensively in the industry. Only a handful of people are capable to use FEM3 CFD and perform the simulation, which makes it difficult to meet industrial needs. Today a need exists for CFD modeling to be used as consequence modeling. FLACS, FLUENT and CFX seem to be the logical choice for LNG vapor dispersion modeling because of the common knowledge in the engineering community of these programs as compared to FEM3 CFD. FLACS is a consequence modeling software as compared to FLUENT and CFX which are more general purpose CFD codes. These CFD models have been seen in the publications and validation work has been done for a certain range.

For the purpose of this research, FLUENT and CFX are more attractive software packages because they are more general purpose tools and have a large users community. FLACS is a consequence model, so by definition, specific to consequence modeling and not flexible enough for this work. Due to the robustness of FEM3A and the large difficulties to deviate from the original example, it does not seem appropriate for this research while other software appear much more practical. FLACS, FLUENT and CFX are generally user-friendly which makes them more desirable for industrial use.

CHAPTER III

FIELD TESTS*

A series of five medium-sized field tests were performed at the Texas A&M University's BFTF for the benefit of this research. The total volume of LNG released was up to 41 m^3 with a range of release rate from 0.2 to 1 m^3/min, the wind velocity from 0.5 to 7 m/s. An array of instrumentation was deployed at the release area and at different distances downwind of the release area. Wind velocity, wind direction, temperature, humidity, gas concentration, heat flux, pressure gauge, level indicator, and flow rates were measured. Gas concentration and temperature measurements at different locations, distances and elevations were recorded. The wind, temperature and concentration data were analyzed to advance the understanding of the source term (pool formation and evaporation).

The series of five tests started in October 2005 until March 2008. MKOPSC LNG team was only involved in analyzing the data for October 2005. The four other tests, April 1006, October 2007, November 2007 and March 2008, were developed and implemented by the LNG team with the help of various vendors. The data for October 2005, April 2006, and November 2007 had significant data for the purpose of this dissertation; therefore they were presented in this section.

BFTF is located in College Station, Texas as part of the Texas A&M University System (TAMUS). One of the primary missions for the BFTF is to educate firefighters understanding LNG behavior and the strategy to handle vapor dispersion and pool fire hazards. In supporting this effort, LNG props were developed funding provided by BP to create four scenarios for firefighters. The props were composed of three pits and one trench. TAMUS used the facility to carry out BP-supported LNG release tests. The three concrete pits noted above are shown in Figure 16. The pits include:

---

*Part of this chapter is reprinted from *Process Safety and Environmental Protection*, Benjamin Cormier, Jaffee Suardin, Morshed Rana, Yingchun Zhang and M. Sam Mannan, Analysis of LNG releases on water with vapor fence, Copyright (2008) with permission from Elsevier.

- Two 1.3-meter deep pits with the area of 3.3 m x 3.3 m (10 ft x 10 ft) and 10 m x 6.6 m (33 ft x 22 ft) called small and large pit, respectively (located on the right of Figure 16).
- One 2.6 meters deep pit with the area of 6.6 m x 6.6 m (22 ft x 22 ft) called marine pit. This pit includes a simulation of a high dike wall, typical of the containment facilities used during LNG offloading (located on the left of Figure 16).
- One L-shaped pit to simulate the trenches used to divert any LNG releases into containment pits (In between the large and marine pit).

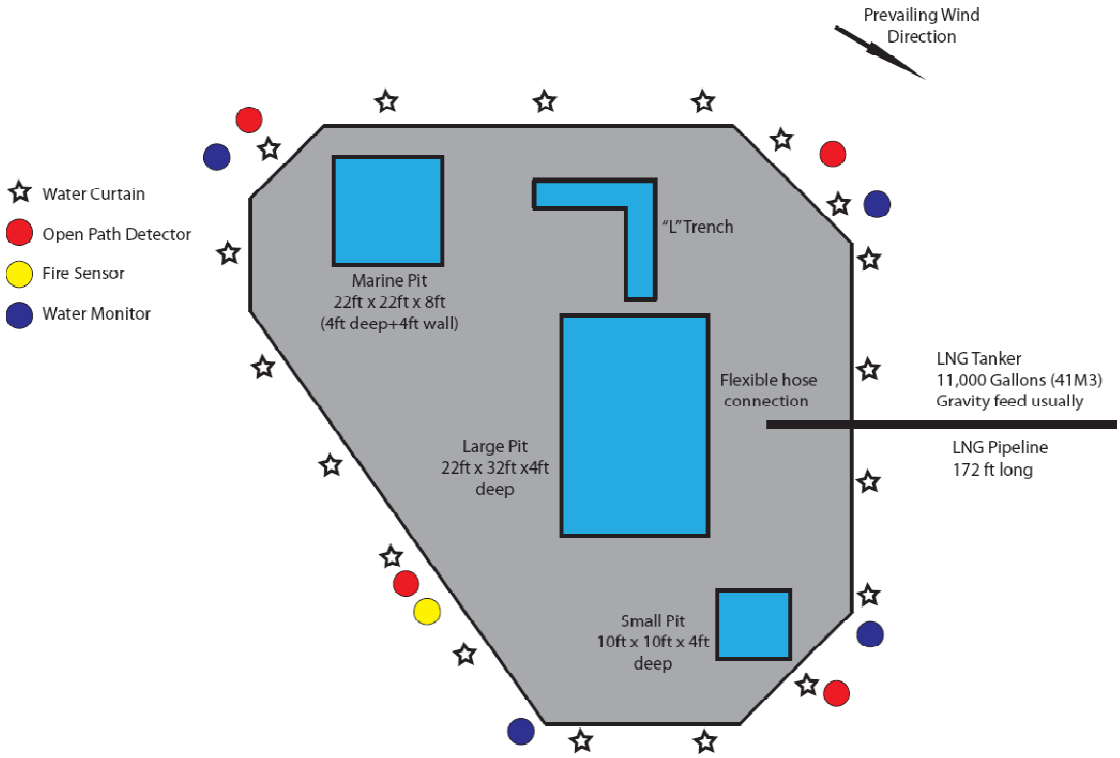

Figure 16. BFTF site description

Around the site, a series of water curtains are deployed to control the dispersion of released LNG. The water monitors are located at three locations around the site. The cryogenic delivery

system is composed of a release line of 60 meters long and flexible hoses. During any release, LNG tanker truck connected to the further side of the delivery line. The volume of the LNG tanker is approximately 41 m^3 (11,000 gallons).

Figure 17 presents the configuration of the LNG delivery system at the fire school. For LNG liquid flow measurement purpose, a flow meter is added to the tanker discharge line, not at the discharge line at the pit. At BTFT, from the bottom of the tanker, LNG will travel through a 2.5-inch diameter at the bottom of the tanker, then through a 3-inch pipeline. A series of 3-inch flexible hose are used to redirect the flow to the desired pit. Finally, a rigid aluminum pipe with a reducer from 3 inch to 2.5 inch is used to deliver LNG into the pit with 45-degree angle.

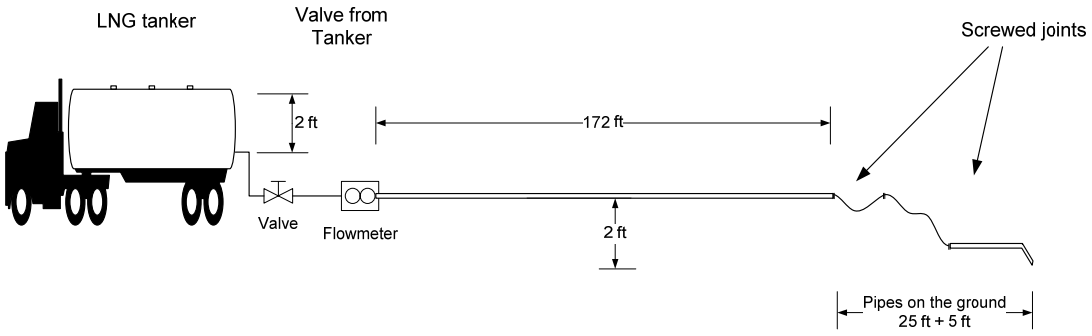

Figure 17. LNG delivery system at the BFTF at Texas A&M University

LNG flow-rate in the delivery line is gravity pressure driven from the tanker. Normal practice is to add a few psi pressures inside the truck up to velocity up the process of discharge. The added pressure is obtained by evaporation LNG inside the tanker. The release is controlled by the valve at the bottom of the LNG tanker. There is no cooling system to pre-cool the delivery line prior to a release.

3.1 October 2005 and April 2006 tests

3.1.1 Instrumentation

ABB Inc., Flameout Controls, and Honeywell Analytics provided the devices and instruments required to measure gas cloud characteristics and record data during LNG releases.

Angus fire provided its latest Turbex fixed high expansion foam generator specifically designed to control LNG releases and fires. The Turbex is capable of up to a 500-to-1 expansion rate. Tests will be conducted using high expansion foam. Angus also provided the instruments and devices necessary to measure foam application rate and thermal radiance to gauge its effectiveness.

3.1.1.1 Gas-concentration sensors

The BFTF has four fixed open path sensors (excel optima) built around the field. Honeywell Analytics provided eighteen portable hydrocarbon point gas sensors (gas point optima) for each test. The placement and number of gas sensors per movable tripod varied with the experimental plan for each test.

Each open path sensor is constituted of two poles. One pole is sending a laser beam to a receiver on another pole. Because a laser beam is used, the poles have to be fixed. Any hydrocarbon gas crossing the path will change the intensity of the laser beam and was used to estimate the linear concentration along the open beam path. The open path sensors record the LFL percentage per meter range. The open-path sensors were covered with fire-proof blankets before any fire is started, during which the sensor reports “fault” due to beam blockage. They will automatically reset back to the actual gas level after they are uncovered. The controller is able to see these readings and interprets them as appropriate. Gas sensors are likely to be saturated as well, and the reading will show as over-scale and not as a fault. Necessary calibration was performed before the test started.

The hydrocarbon point gas sensors on tripod were mounted on a movable tripod. Each hydrocarbon point gas sensor was connected with a 3-wire 4-20mA source output to the ABB AC800xA controller. They required about 5 watts of power each. Gas sensors monitored in the range of 0 to 100% LFL. The gas sensors were calibrated with a 50% methane gas. An

approximation of a gas cloud %LFL based on content and size were obtained. An ABB AC800xA data acquisition system records each sensor signal throughout the test period. It was intended to coordinate this with the hydrocarbon cameras and color cameras provided by Flameout Control to characterize the LNG vapor dispersion behaviors.

3.1.1.2 Thermocouples

In order to measure the heat transfer from the water to the LNG layer, thermocouples were installed and properly distributed within the water. The measurement of the water temperature profile was crucial in determining heat flux from the water to the LNG pool on top of the water surface to support LNG evaporation. Two extra thermocouples were installed above the pit to measure the temperature above the pit.

3.1.1.3 Weather station

In 2005, temperature, wind direction, humidity and atmospheric pressure were measured with a Kestrel 4100 portable weather instrument taken every thirty seconds. In 2006, a weather station was provided by Texas Mesonet at TAMU. Wind direction and wind velocity were measured at the height of two and ten meters. Humidity and atmospheric pressure were collected as well. The data were collected and stored every three seconds.

3.1.2 Tests procedure in October 2005

In October 2005, 38 m^3 (10,000 gallons) of LNG was used. The vapor dispersion measurement and data collection were performed in parallel with Angus foam test. The LNG was characterized as 98% methane. However, no LNG samples were archived for later analysis.

3.1.2.1 Test 1

The Angus test required a minimal five inch depth LNG pool in the large pit, shown in Figure 16. Six tripods with three gas sensors were placed along the path of the open path sensors. On each tripod, the first sensor was placed at the height of the infrared beam path of the open path sensors. The second sensor was at two feet above the infrared beam. Finally, the third sensor was between five and seven feet above the infrared beam depending on wind. The vapor dispersion data was recorded over one hour and twenty six minutes period while the

pool was filling up. The data collection was stopped and the gas sensors were removed once the fire test started. The placement of the hydrocarbon point gas sensors is shown in Figure 19.

3.1.2.2 Test 2 a and b

The second test was performed during the afternoon. The second pit was again filled to a five inch depth of LNG. Six tripods, with three point gas sensors on each, were placed around the pit during the filling. The gas sensors were later relocated for the foam test, as shown in Figure 19. Two applications of high expansion foam were provided by Angus. Then the gas sensors were removed before the beginning of the fire test. LNG was released into the pit at ground level with a hose pointing downward with 45 degree angle. The position of the discharge pipe did not change between the two phases. The prevailing wind was dominant during the test period.

3.1.3 Tests procedure in April 2006

38 m^3 (10,000 gallons) of LNG was used in April 2006 test. This event involved the many different organizations cited previously. On the morning of April 20, 2006, the vapor dispersion tests on water were performed and lasted till mid-day. Then the LNG burning test was executed. The vapor dispersion tests consisted of two phases, called as Test 1 and Test 2.

3.1.3.1 Test 1

Test 1 was a LNG release onto water. The marine pit was filled with water up till the top. LNG is delivered on the top of the water in the middle of the pool. Twelve thermocouples were distributed within the water at different levels to measure heat transfer effects. An underwater camera was installed on the bottom of the pit to analyze the size of the LNG pool on the water surface. Two extra thermocouples and hydrocarbon point gas sensor were placed above the pit. Figure 18 illustrates the configuration of the tripod outside of the pit for Test 1. The hydrocarbon point gas sensors were placed at two different levels, 1 feet and 4 feet respectively.

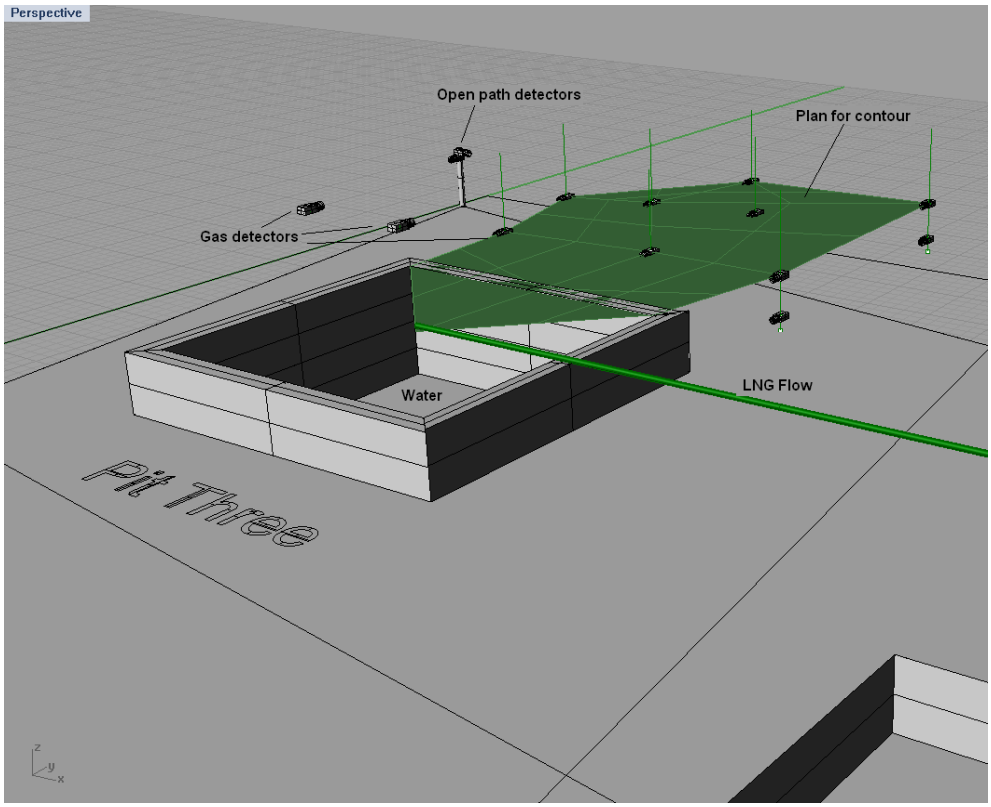

Figure 18. Side view of hydrocarbon point gas sensor position for test one

This figure also shows the plane for gas concentration contours that will be used later on in the preliminary data analysis.

3.1.3.2 Test 2

The second test was designed to study the effectiveness of current methods for LNG release mitigations such as high expansion foam and water curtains. The effectiveness of an upward vertical jet water curtain and high expansion foam on dissipating and controlling the LNG vapor were demonstrated by a decrease in %LFL levels detected with gas detection instruments. The parameters used to characterize water curtain and high expansion foam such as water pressure, water curtain dimensions, foam application pressure, application rate, etc., were recorded during the test. This test was considered to be unconfined LNG release, because the pit geometry did not constrain the vapor cloud migration. The evaporation of LNG was facilitated

due to higher heat transfer from the water. The water curtains were installed all around the pits and along the open path sensors. Data were recorded before and after the water curtains.

3.1.4 Gas concentration analysis

The experiments performed at TAMU spread over the last two year period. Because of time constraint, several scenarios were developed and measured during one day period. The parameters used during these tests are summarized in Table 9.

Table 9. Characteristics of LNG experiments at BFTF, October 2005 and April 2006

Parameter	*Experiments*			
Date	October 2005		April 2006	
Name	Test 1	Test 2 a	Test 1	Test 2
Release type	Ground	Ground	Onto water	Onto water
dQ/dt, kg/min	91.2	91.2	91.2	91.2
Duration, min	86	64	13	12
Wind velocity, m/s	1.1 to 5.3	3.9 to 5.1	1.3 to 5.3	1.3 to 5.3
Height above ground, m	2	2	2 and 10	2 and 10
Relative humidity, %	58 to 48	44 to 31	NA	NA
Temperature atmospheric, F	88.5	84.5	NA	NA
Pit location	Large	Large	Marine	Marine
Area of release, m^2	67.5	67.5	43.6	43.6

Figure 19 shows the placement of the gas sensor tripods for different test scenarios performed at BFTF. In 2005, six tripods with three hydrocarbon point sensors each were used. In 2006, eight tripods with two sensors each were used and two extra hydrocarbon point gas sensors were placed above the pit.

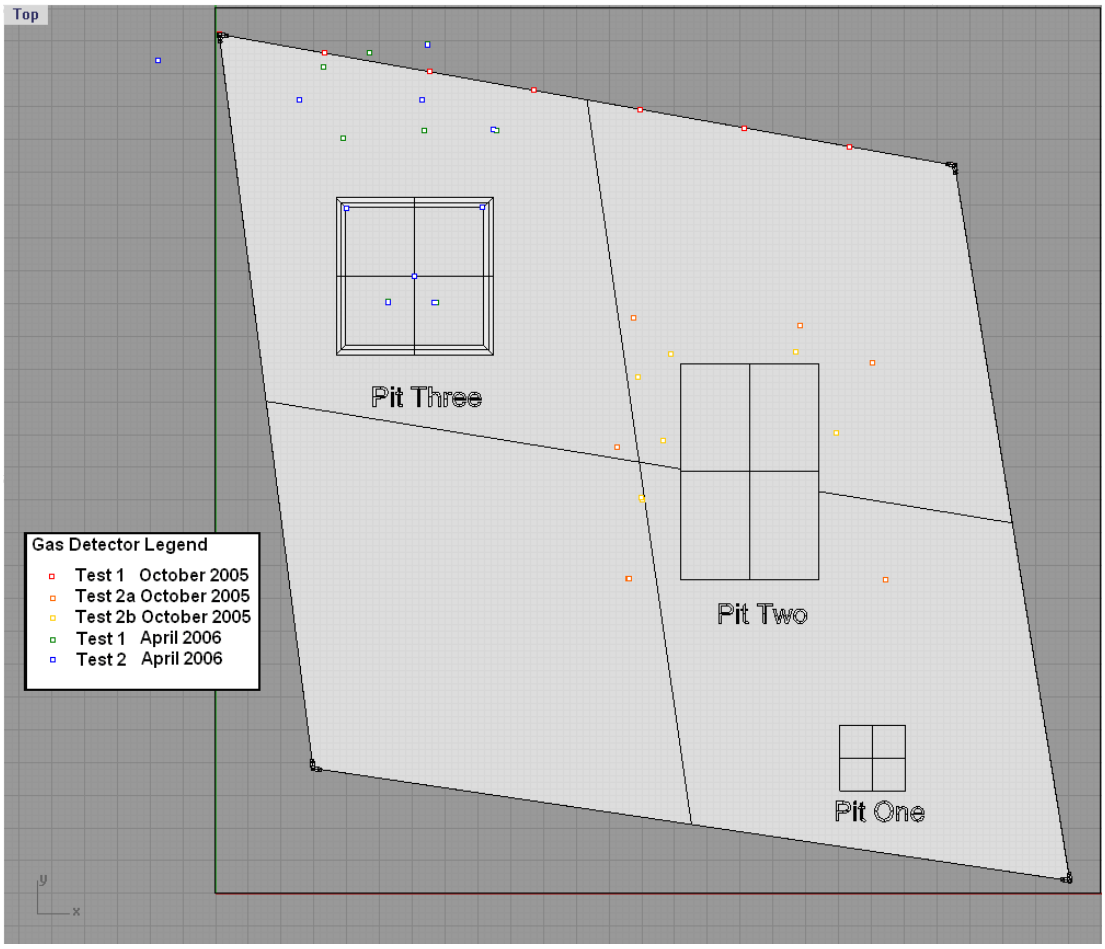

Figure 19. Top view of gas sensors location for each test

For the first test in 2005, the hydrocarbon point gas sensors were placed along the open path sensors. It also shows the placement of the sensors evenly distributed along the beam of the open path sensors marked as red on the figure. For the second test in 2005, the vaporization effect was studied. The sensors were placed around the large pit, marked as orange. Then they were moved closer to the pit for the foam test, marked as yellow. High expansion foam was applied twice and data were recorded.

In 2006 test, LNG was released onto water surface. The configuration of hydrocarbon point gas sensor was designed differently than it was previously. The pit configuration was run with several vapor dispersion models and an optimal location was chosen for each tripod. The

predicted concentration area was divided in three sections: LFL, 1/2 LFL and behind the water curtain. Two extra gas sensors were placed above the pit to observe the change in LNG vaporization due to application of high expansion foam during the last phase of this test. Due to change in wind direction, the hydrocarbon point gas sensors were moved to optimize data collection, as marked in Figure 19.

During the experiments, the gas concentration was measured and collected at two or three points of each tripod. Several points on the same level form a horizontal plane where the interpolation and gas concentration contours were done. In 2005, the data were collected at 1.3, 1.9, and 2.7/3.6 meters high (i.e. 4, 6, and 9/11 feet high). In 2006, the configuration of gas sensors was developed using the predicted results from two-dimensional simulation software such as PHAST, DEGADIS, and CANARY. These results were used to define zones of effect for LFL, 1/2 LFL and 1/5 LFL, respectively. The height of the gas sensors was determined similarly. The hydrocarbon point gas sensors were set at 0.3 and 1.3 meter high (i.e. 1 and 4 feet high).

The measured gas concentration data was used to plot the concentration contours of methane with Matlab® program. The program connected the points on the same plane and performed interpolation between two points. The primary interpolation was creating a connection between the source point and the sensor on the same plane. Then a second interpolation created centerline between the sensors. Then the last interpolation, a lateral interpolation, is performed between centerlines on the lateral planes.

3.1.4.1 October 2005

3.1.4.1.1 Test 1

A five inch depth of LNG in the pit took one hour and twenty six minutes to achieve. Then the LNG was ignited in the burn and foam test. During the analysis of the data, several observations were made. The data revealed while the pit is filled, it goes through three stages:

- Pipe cooling – 15 minutes
- Unsteady state – 55~60 minutes
- Steady state – 35~40 minutes

Naturally, LNG will flash to cool down the pipe originally at ambient temperature. Energy balance showed that it will take no longer than 20 minutes to cool down the pipe with LNG (strongly depending on the flow rate). During the pipe cooling, the hydrocarbon point gas sensors show the highest activity during the entire time period. Then once LNG came out, the pit starts cooling down. During the pit cooling, the gas sensors record a high activity as much as while the pipe was cooling down. It was observed that after three inch depth of LNG in the pit, the evaporation rate seems to reach a steady state. Over time, the activity of the gas sensors slows down approaching a steady state.

During this test, Flameout used a hydrocarbon camera to illustrate the difference between the hydrocarbon cloud and the condensate vapor cloud called white cloud. These images are taken through new technology utilizing Ultraviolet/Infrared video imaging which detects hydrocarbons in real time utilizing the same absorption techniques which allow for open path gas detection. Figure 20 shows the different between the condensate vapor cloud can be seen and the really extend of the carbon cloud.

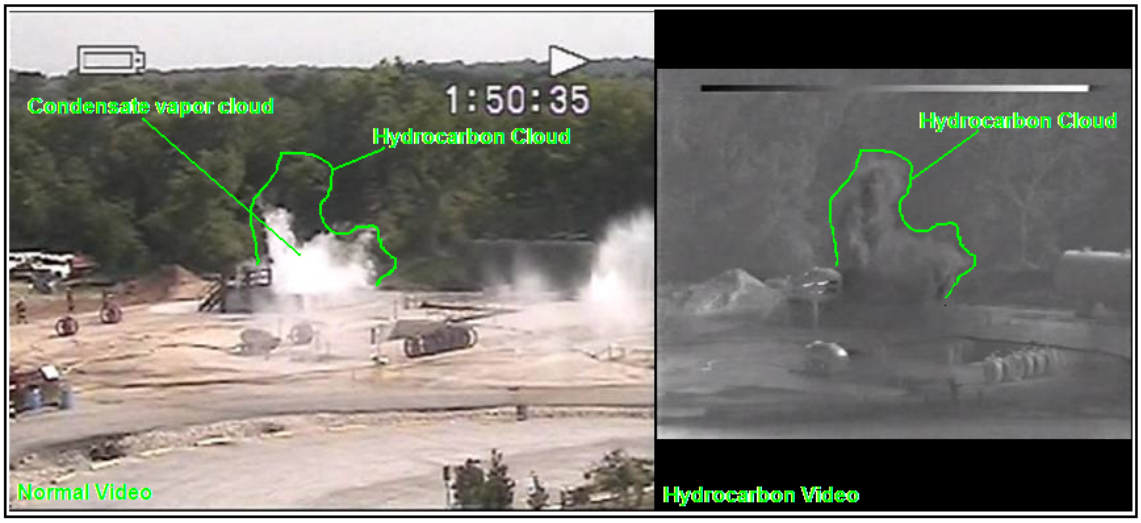

Figure 20. Comparison between condensate and hydrocarbon vapor cloud (Courtesy of Michael Moore, Flameout)

3.1.4.1.2 Test 2 a and b

As described, Test 2 was divided in two phases, “a” and “b”. The first phase is to fill the second pit and the second phase is foam application with no LNG feed. The test last for two hours and ten minutes. The data shows the same behaviors stated in the previous analysis, but with a different weather conditions. Once the pit was filled with five inches of LNG, high expansion foam was deployed. Figure 21 shows the behavior of the concentration of LNG along the centerline during the entire test.

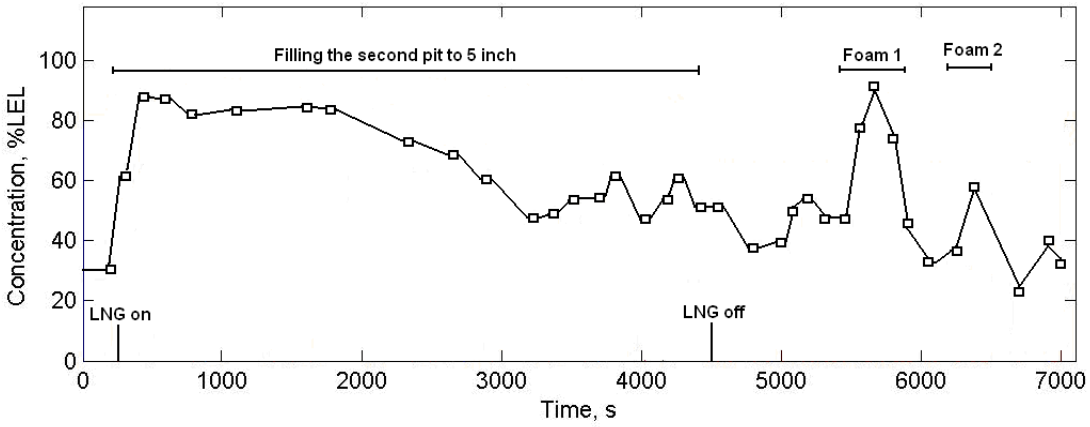

Figure 21. Concentration profile at fixed point along the centerline

This figure may be separated in six sections:

- Unsteady state with high evaporation rate, from 200 (i.e. LNG on) to ~1500 seconds
- Approaching steady state with the concentration level lowering down (i.e. evaporation lowering down), form ~1500 to ~3100 seconds
- Steady state with constant low evaporation rate, from ~3100 to 4600 seconds (i.e. LNG off)
- Steady state with no LNG feeding, from 4600 to ~5500 seconds (i.e. before foam applications)
- Increased evaporation rate at the first foam application at ~5700 seconds
- Another increased evaporate rate at the second foam application at ~6300 seconds

3.1.4.2 April 2006

During the April 2006 tests, weather condition changed, especially wind direction prompted the team to change the position of the tripods. Figure 22 shows also the coverage of the hydrocarbon point gas sensors for Test 1 and 2.

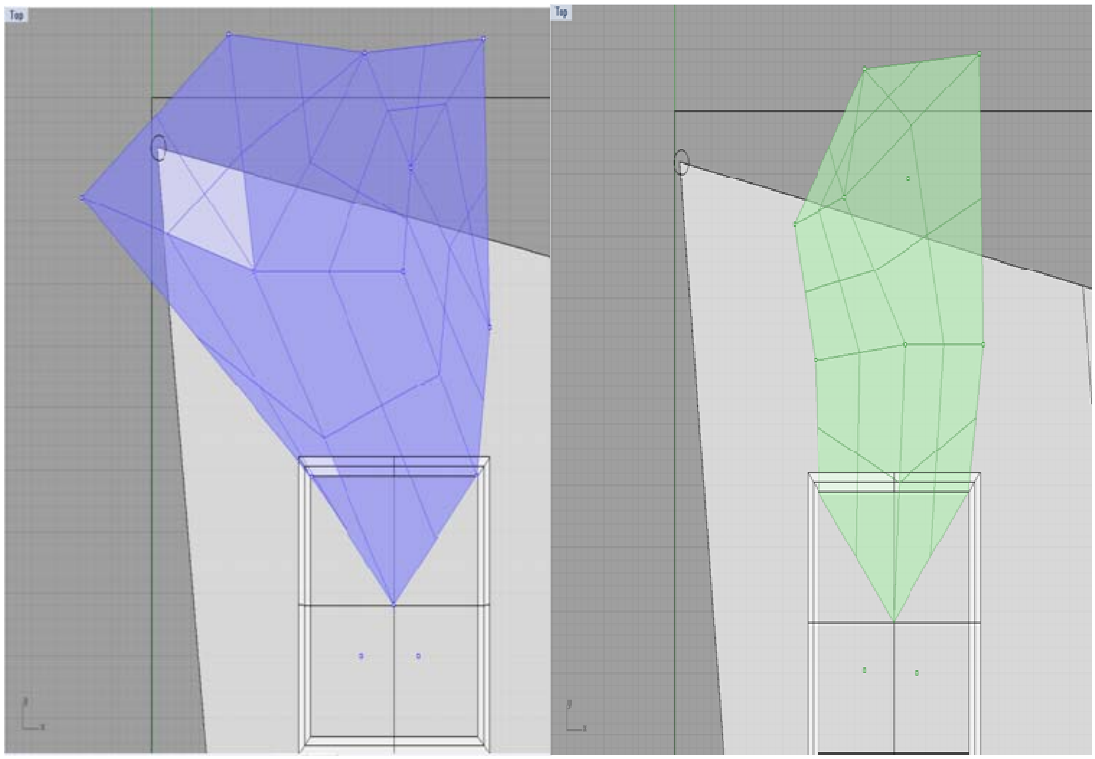

Figure 22. Top view of gas sensor coverage area for April 2006 test 1 and test 2

This top views give the coverage area of the vapor cloud dispersion for interpolation domain for gas concentration contours. The simulations helped to estimate the ranges and zones of the dispersion. The gas sensors at the same level form a plane where the data may be interpreted and plotted.

An interesting observation was made during the LNG release onto water in April 2006. During the Release onto water, Ice was formed on the top of water. Figure 23 illustrates this phenomenon.

Figure 23. Illustration of ice formation on water after test one

3.1.4.2.1 Test 1

The first test was to measure the gas dispersion and verify the two dimensional simulations performed previously. During the LNG release onto water, the formation of an eight-foot diameter pool was almost instantly. The LNG pool went to steady state rapidly in 1-2 minutes. Figure 24 presents the concentration contour in % LFL at four feet for LNG release onto water.

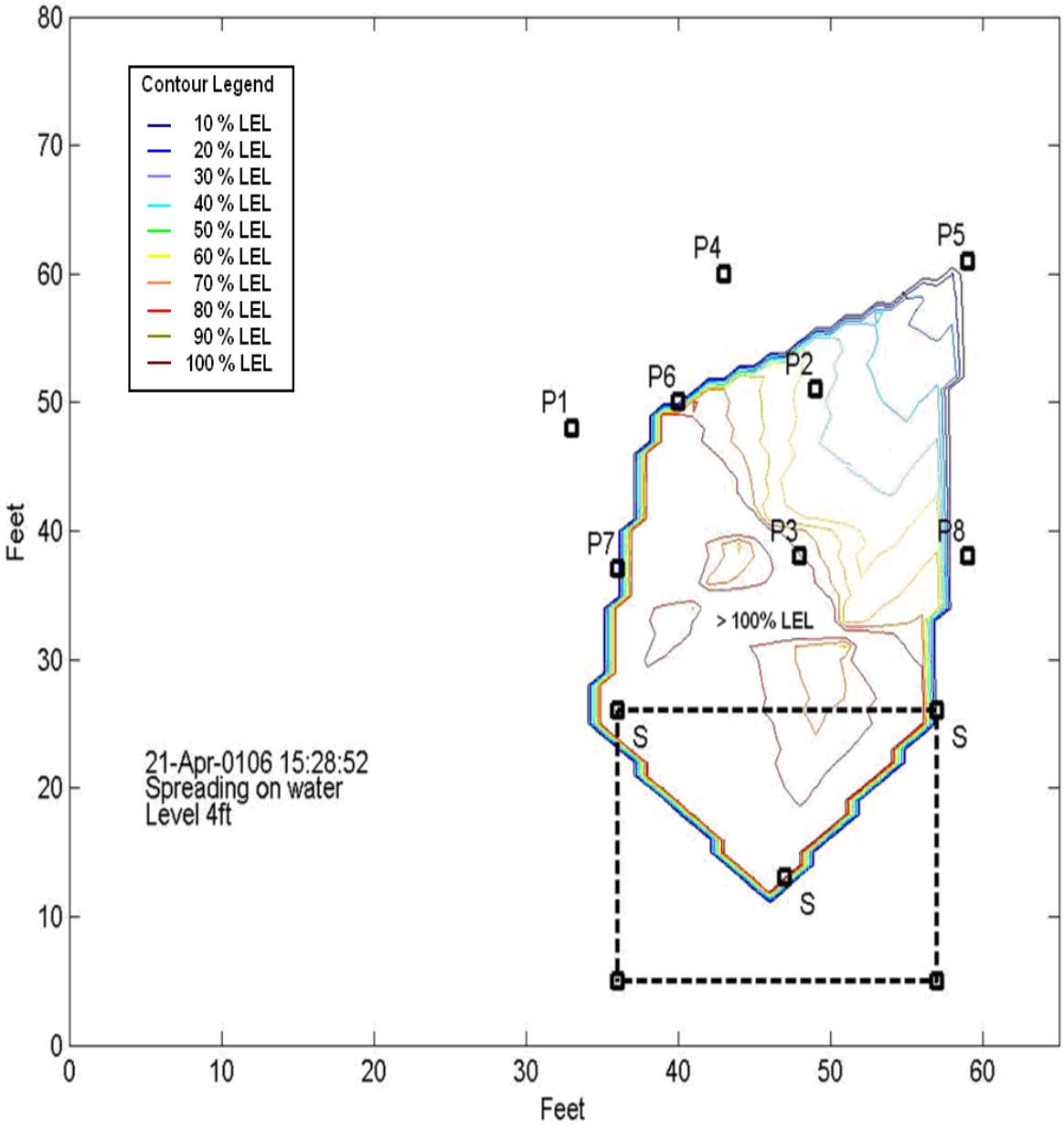

Figure 24. Concentration contour at four feet high during LNG release onto water with no mitigation systems

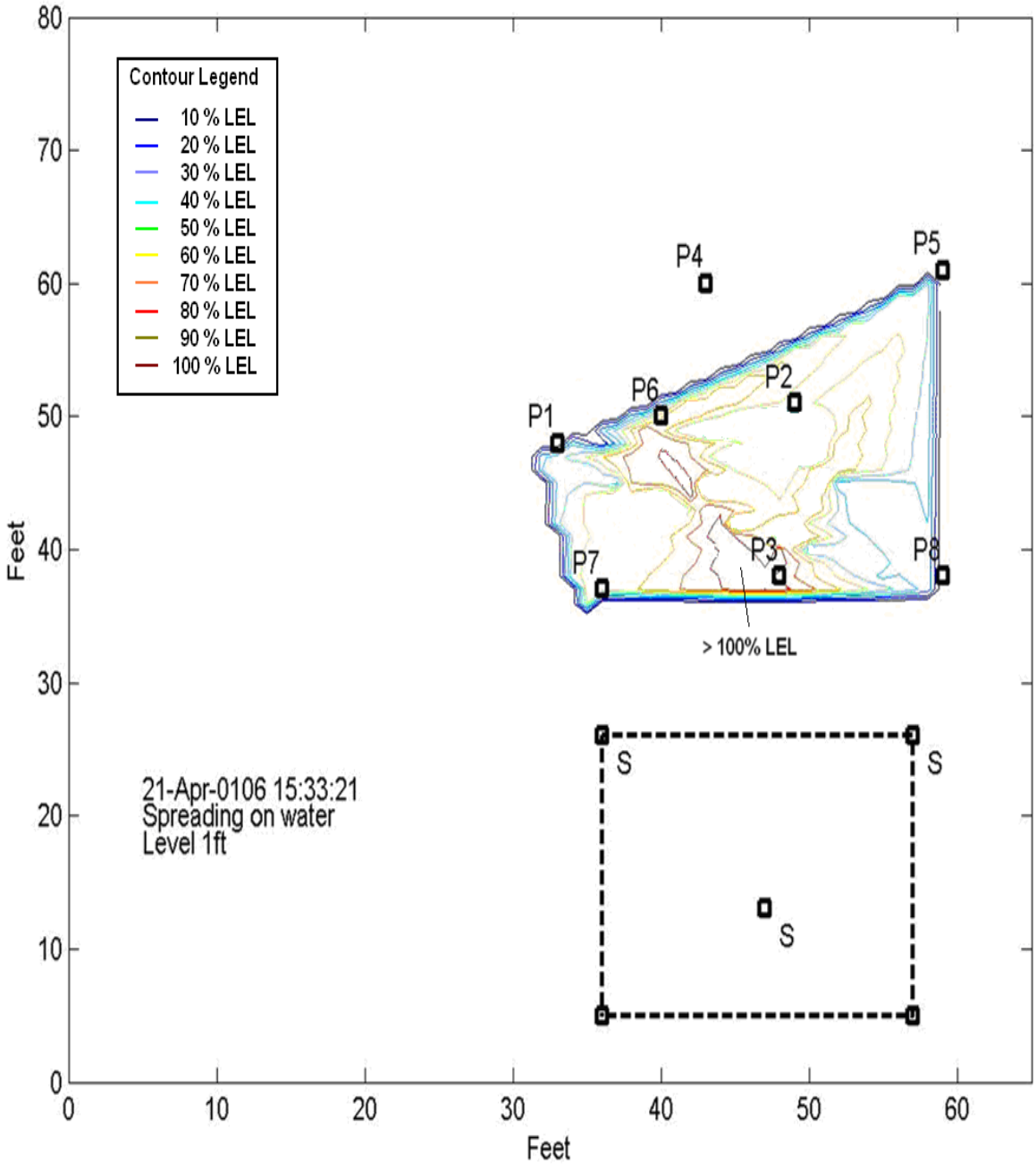

Figure 25. Concentration contour at one foot high for LNG release onto water with no mitigation system

Figure 25 present the concentration contours in % LFL at two levels, one foot and two feet. During the LNG release onto water, the gas sensor at P6, P7 and P3 recorded a concentration of 100 % LFL at four feet. P6 and P3 recorded a concentration of 100 % LFL at one foot. This illustration shows that the vapor cloud left the top of the water surface and felt down to the ground traveling horizontally until the gas cloud was warmed up sufficiently (i.e. expanded) and raised.

3.1.4.2.2 Test 2

For Test 2, while LNG was release on the top of water, water curtain and high expansion foam were applied subsequently. Figure 26 shows the concentration contour at four feet high with the water curtains on as well as the water curtains location. Figure 26 shows P7 and P6 were still recording 100% LFL. The comparison between Figure 24 and Figure 26 showed that the water curtains reduced the downwind distance by air entrainment. Figure 27 shows the gas concentration contour once the foam was applied.

The comparison between Figure 26 and Figure 27 shows that once the foam is applied, the levels of % LFL dropped at four feet high. Only P8 and P7 picked up some small reading of hydrocarbon. This observation was illustrated with LFL distance shown in Figure 28, which presents the LFL distance profile during Test 1 and 2.

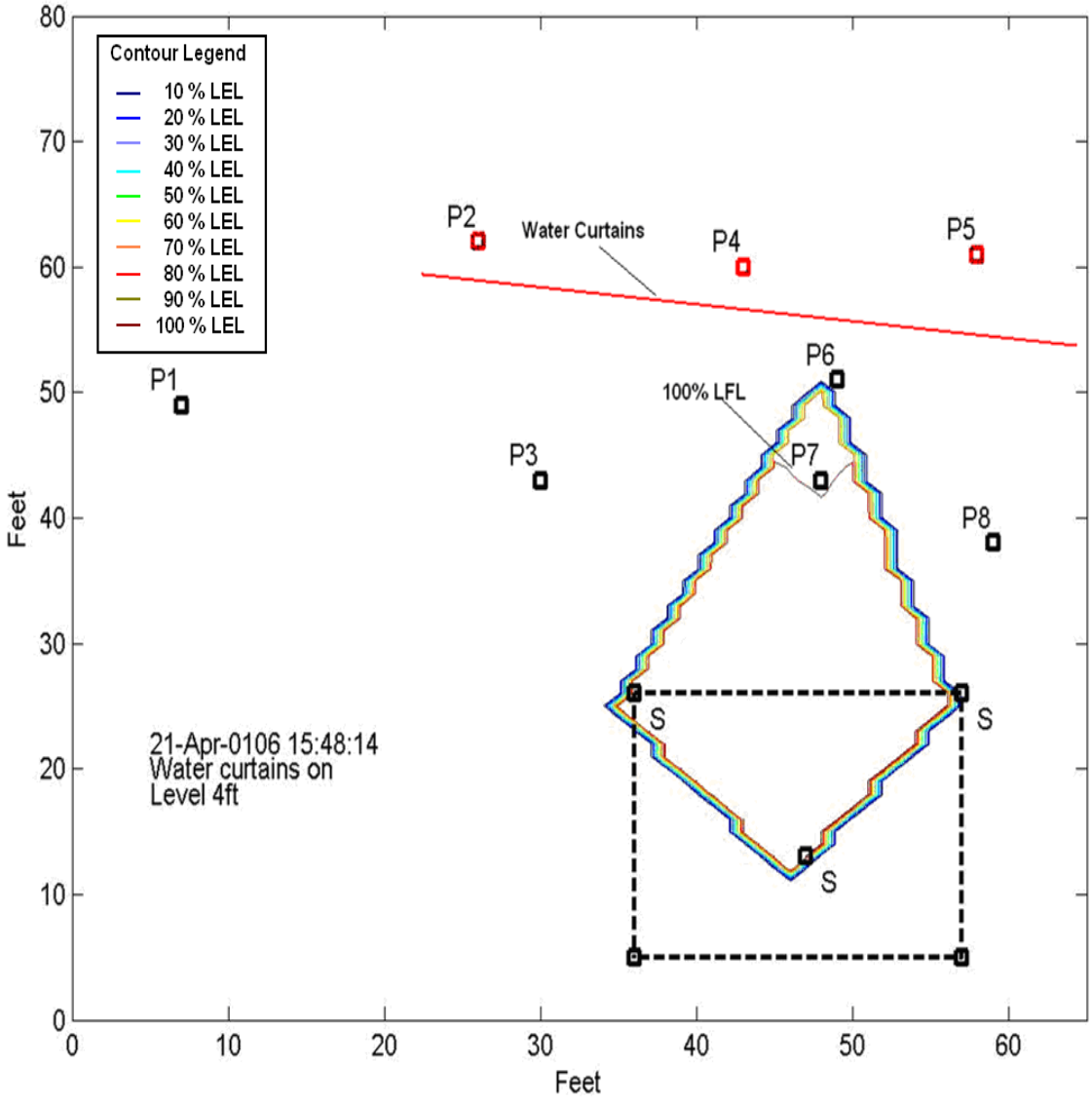

Figure 26. Concentration contour at 4 feet high during water curtains on

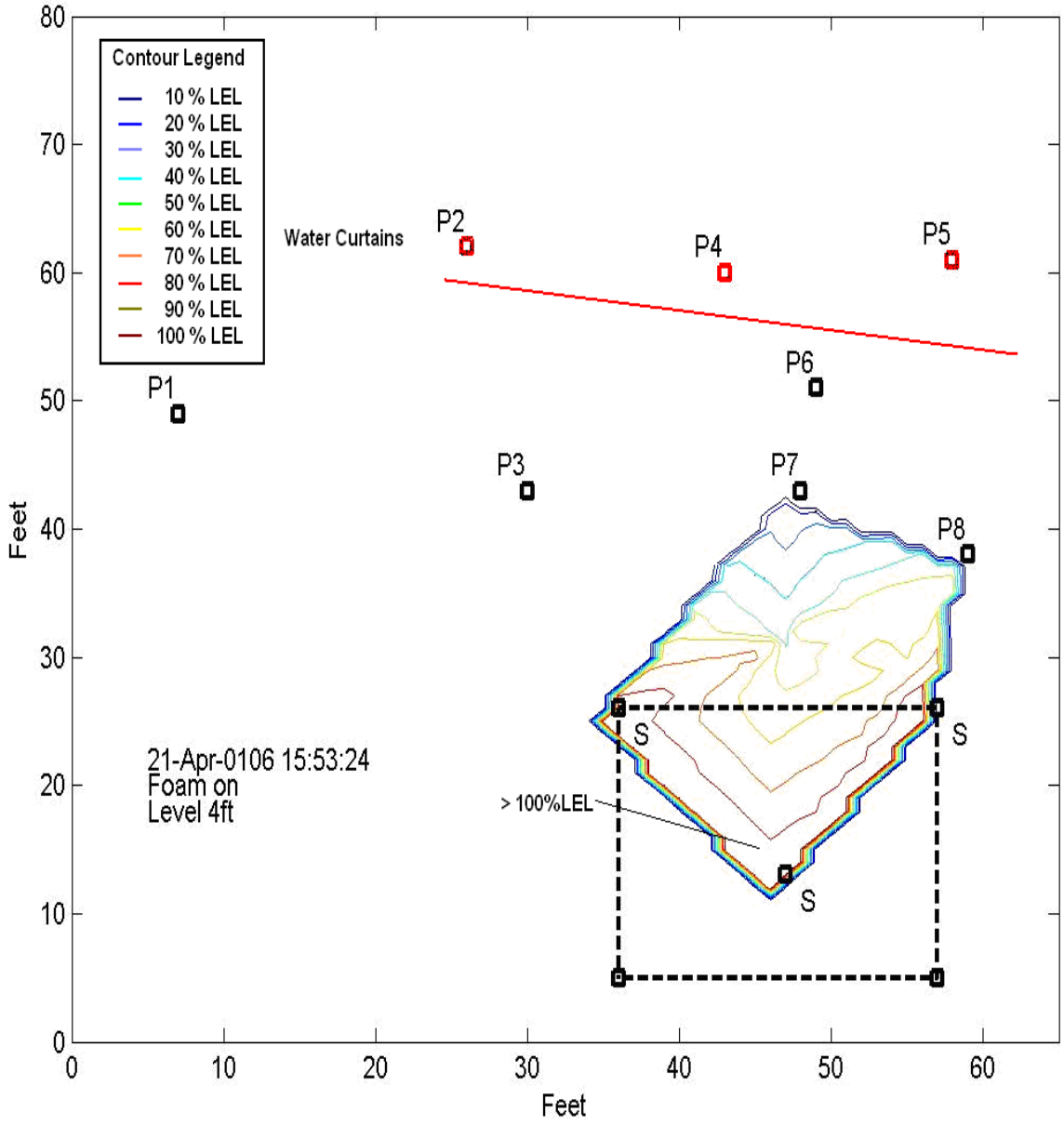

Figure 27. Concentration contour for LNG release onto water with foam application at four feet high

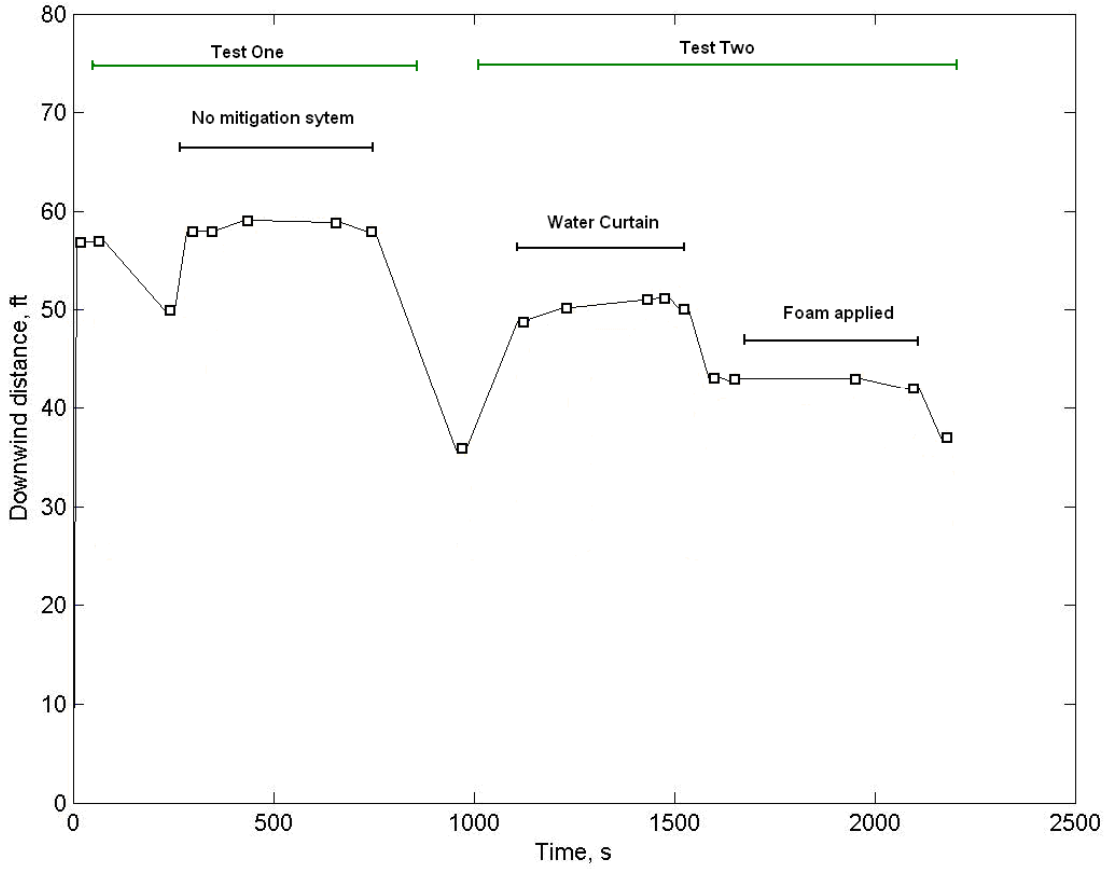

Figure 28. LFL downwind distance during April 2006 tests

Figure 28 shows the reduction of LFL downwind distance during April 2006 tests. The maximum downwind distance observed was 18.2 meters (60 feet). Once the water curtain was applied, the downwind distance was reduced to 15 meters (50 feet). The downwind distance was further reduced to about 12 meters (40 feet) when the foam was applied.

3.1.5 Temperature analysis

Temperature sensors were distributed in the water in order to record the temperature of the bulk. The main purpose of these sensors was to capture the heat transfer within the water while LNG was released. Because of fast evaporation and vapor cloud formation, the temperature sensors within the water are able to capture the heat transferred to the LNG layer

to estimate the mass evaporation rate. Twelve temperature sensors were used and placed in the water underneath the LNG layer. The placement of the temperature sensors is presented in Figure 29. The LNG release point is with a 45^{o} angle of 2-inch aluminum pipe. As shown in Figure 29, four sets of three sensors were placed around the release point to obtain a three dimensional representation of the water temperature profile.

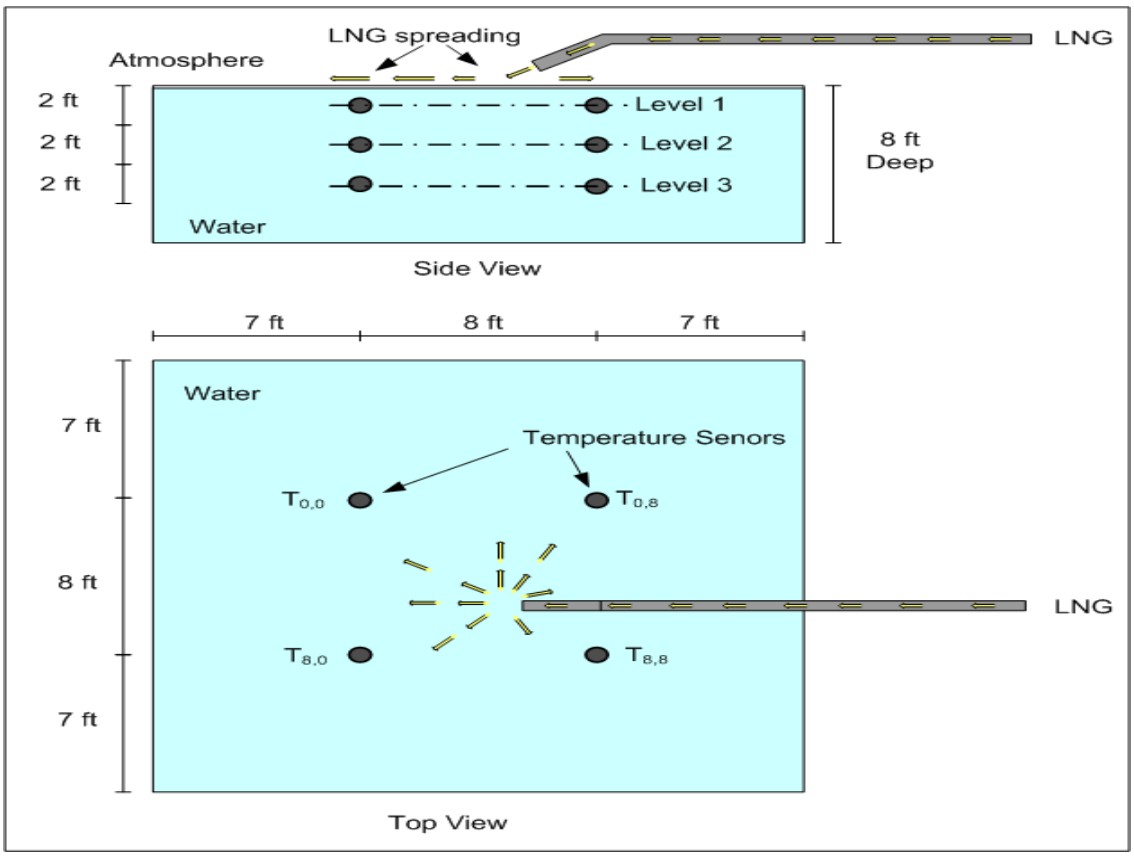

Figure 29. Placement of the temperature sensors in the water, top and side view

During the day, two runs of approximately ten and twenty minutes were performed. The LNG flow rate was estimated at 56 GPM from the release point. Some of the LNG flashes before reaching the surface of the water. LNG composition was about 99% methane.

The temperature data was collected every second and analyzed. The temperature profile may be used to estimate the heat transfer from and to the LNG layer. An algorithm was developed to analyze the temperature profile of the water.

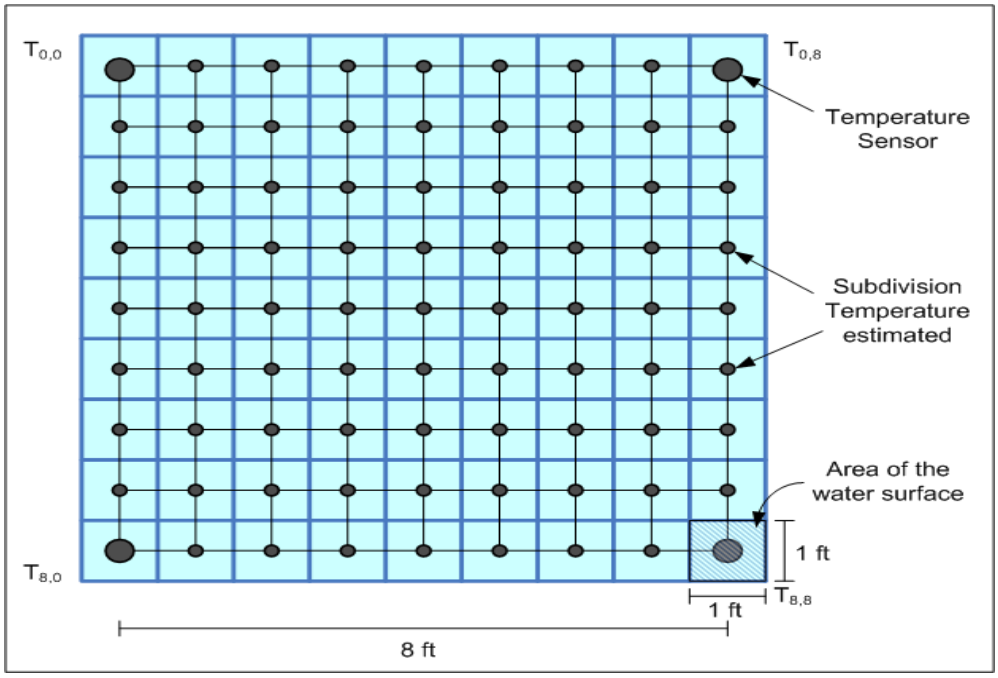

Figure 30. Configuration of the grid at level one

Figure 30 shows the configuration of the grids for level one of temperature sensors. This same grid was developed for the two other levels. The temperature profile may be determined as presented in Figure 30. Each point is represented algebraically by using the following notation:

$T_{j,k}(t)$ with *j*=0…8 and *k*=0…8 at instance *t*.

j and *k* represent the location on the grid. $T_{0,0}$, $T_{0,8}$, $T_{8,0}$ and $T_{8,8}$ represents the location where the thermocouples are located. The distance between each sensor was eight feet. This distance was divided into eight subdivisions. Each surface created by the subdivisions has an area of one square foot. The points from each subdivision are estimated by using a linear

interpolation with respect to the thermocouples. The heat transferred to the water from the LNG layer can be formulated by the following:

$$Q_{j,k}(t)=mC_p\Delta T_{j,k}(t) \quad (53)$$

$$\Delta T_{j,k}(t)=T_{j,k}(t+1)-T_{j,k}(t) \quad (54)$$

m represents the mass of water present around the temperature sensors. This volume is constant over time and it is 0.056 m^3 (or two cubic feet). The heat capacity, C_p is also constant, 4.185 kJ/kg K for water. The only variable is the temperature change. Similarly, the heat transferred to the water at each level can be estimated. The total heat transferred to the layer is calculated with following equations:

$$Q(t)=\sum_{j=0}^{8}\sum_{k=0}^{8}Q_{j,k}(t)=mC_p\sum_{j=0}^{8}\sum_{k=0}^{8}\Delta T_{j,k}(t)=mC_p\sum_{j=0}^{8}\sum_{k=0}^{8}\left(T_{j,k}(t+1)-T_{j,k}(t)\right) \quad (55)$$

The calculation of the heat transferred was performed using an algorithm and implemented in MATLAB®.

Heat transfer phenomenon within the water when LNG is released on the top is studied using the collected data. The temperature profile shows the effects of the cryogenic liquid release onto the water. A layer of LNG was formed and some ice formation was observed on the edge. From the data analysis, LNG boil-off rate was estimated at four different locations. The water is constrained into a pit, the wall of the pit are made of special concrete developed by the fire school. During this analysis, the heat input was considered to come only from the LNG layer because the wall of the pit does not provide any heat input to the water. Therefore the total heat input from the LNG layer should be equal to the total heat transferred into the water. By using Equation 53, the lost of heat to the surrounding was calculated over the period of the test.

$$Q_{in}-Q_{out}=Q_{surrounding} \quad (56)$$

Where Q_{in} is the negative heat input due to the LNG layer and Q_{out} is the positive heat input resulting from mixing to reach equilibrium temperature. The positive heat input is the response for the temperature change due to negative heat input. $Q_{surrounding}$ is either energy

lost to the surrounding or data lost during the recording. The data shows $Q_{surrounding}$ (i.e. energy lost) is less than 4%.

Figure 31 shows the total heat transferred at level 1 using Equation 53. The negative and positive peaks represent a cooling and heating cycle of the layer respectively. In other words, the negative and positive peaks show the decrease and increase in the temperature at the level 1 from the data respectively.

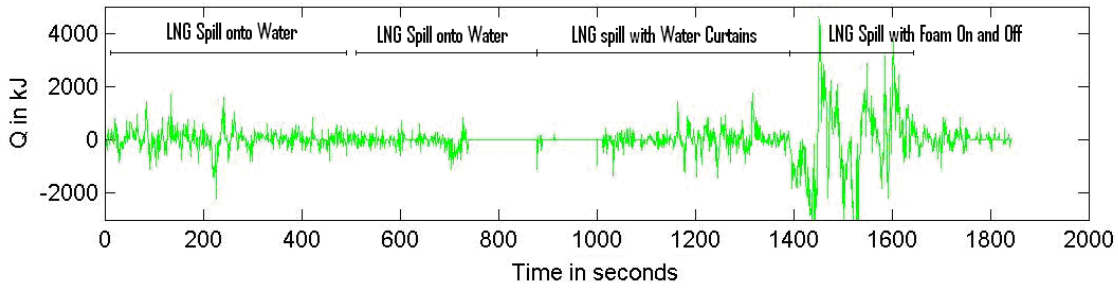

Figure 31. Heat transfer for level 1

Figure 31 has four segments, which is pointed out in the top of the figure. For the first and second segments, LNG is released onto water with no mitigation measures. For the third segment, LNG is released onto water with water curtain application which did not affect the mass evaporation rate since it is independent from LNG evaporation phenomenon. For the fourth segment, LNG is released onto water with foam application. Between 720 and 1000 seconds, the data was lost due to circuit short. The negative and positive peaks are studied further in the following sections.

3.1.5.1 Heat transfer due to convective current

The positive heat transfer peaks were extracted and presented in Figure 32. This figure shows the distribution of this positive heat transfer during the test.

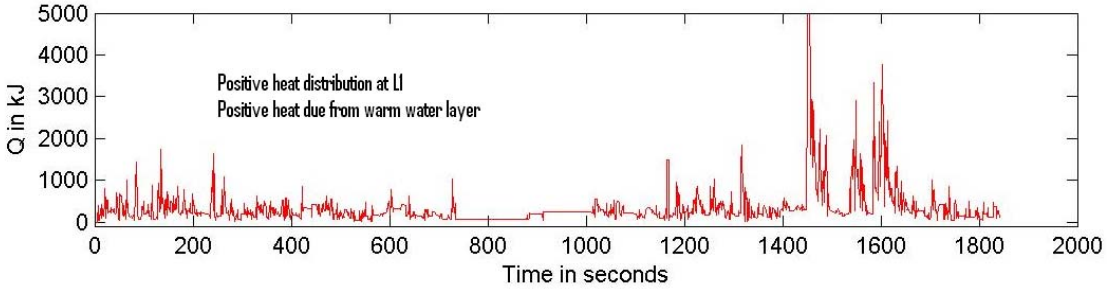

Figure 32. Positive heat transferred due to convective current

The behavior of the positive heat transferred seems to be corresponding to the negative energy input. While LNG layer is applied onto water, heat is provided from water surface close to level 1. Temperature gradient changes the water density and creates a negative buoyancy effect. In other words, the colder water sinks to the bottom of the pit. While the chilled water sinks, it pushes the warm water underneath upward. The warm water is pushed up along the level 3, on to level 2 and then level 1. Figure 33 illustrates this effect.

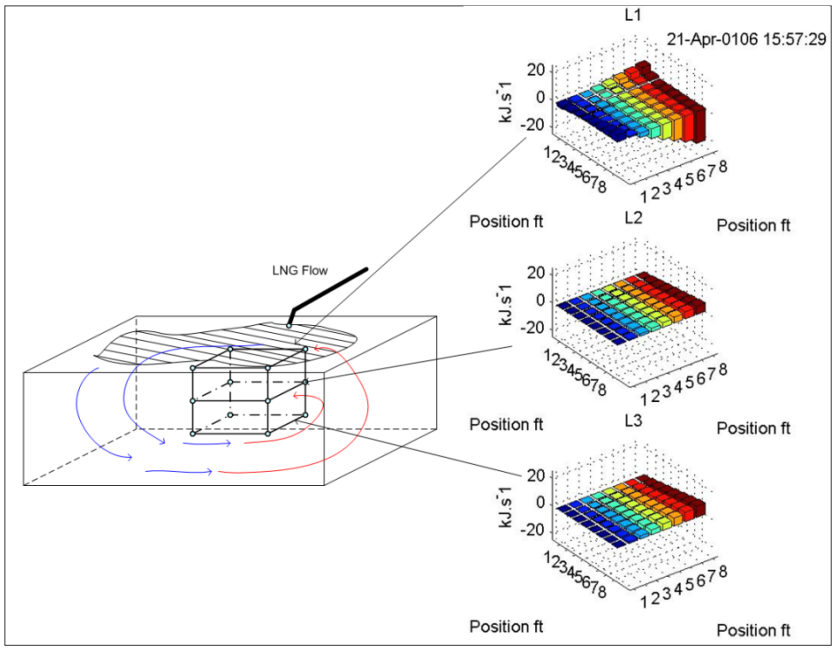

Figure 33. Heat transferred for each layer and current effects

Figure 33 shows the convective current effect and heat transferred to level 1, level 2, and level 3 for an instance. Blue and red arrows represent cold and warm water currents in the pit, respectively. Because of the orientation of the LNG layer, not only vertical convective current is created but also a horizontal current as well. On the left of the figure, the bar-graphs present the heat input at each level and illustrate the effect of the convective current due to the cold LNG layer. While negative heat transfer occurs at level 1, a positive heat transfer is introduced at level 2 and level 3.

3.1.5.2 Mass evaporation rate estimation

From the heat transfer analysis, LNG mass evaporation rates were estimated. Each vertical array of three temperature sensors was placed at different position relative to the incoming LNG hose. The pipe opening was situated about one and half above the water surface. The end of the pipe was open and the LNG was shot directly onto the water surface. $T_{8,8}$ was the closest to the LNG source and $T_{8,0}$ was the next closest. $T_{0,8}$ and $T_{0,0}$ were further down the LNG layer as shown in Figure 29. Because of this configuration, several observations were made from the data analysis. LNG was spread with an initial momentum due to the height between the water surface and end of the pipe. This initial momentum creates a lot of turbulence near the landing area, located next to $T_{8,8}$. Because of the uneven distribution of the poles compared to the incoming LNG, the estimated mass evaporation rates at the spots (0,0), (0,8), (8,0) and (8,8) are not exactly equal to each other. By using equation 55 and the latent heat of methane, the mass evaporation rate was estimated and presented in Table 10.

Table 10. Summary of estimated LNG mass evaporation rate

	$T_{8,8}$	$T_{0,8}$	$T_{8,0}$	$T_{0,0}$
Layer State	Unsteady	Steady	Meta steady	Steady
Mass evaporation rate Calculated, kg/m^2 s	0.50 to 0.80	0.25 to 0.30	0.40 to 0.50	0.25 to 0.30

Table 10 presents the mass evaporation rates at different location in the pit. $T_{0,8}$ and $T_{0,0}$ represent the steadiest results, while $T_{8,8}$ shows the most instability due to the high turbulence created by the initial momentum of the release. This behavior is also illustrated in Figure 34.

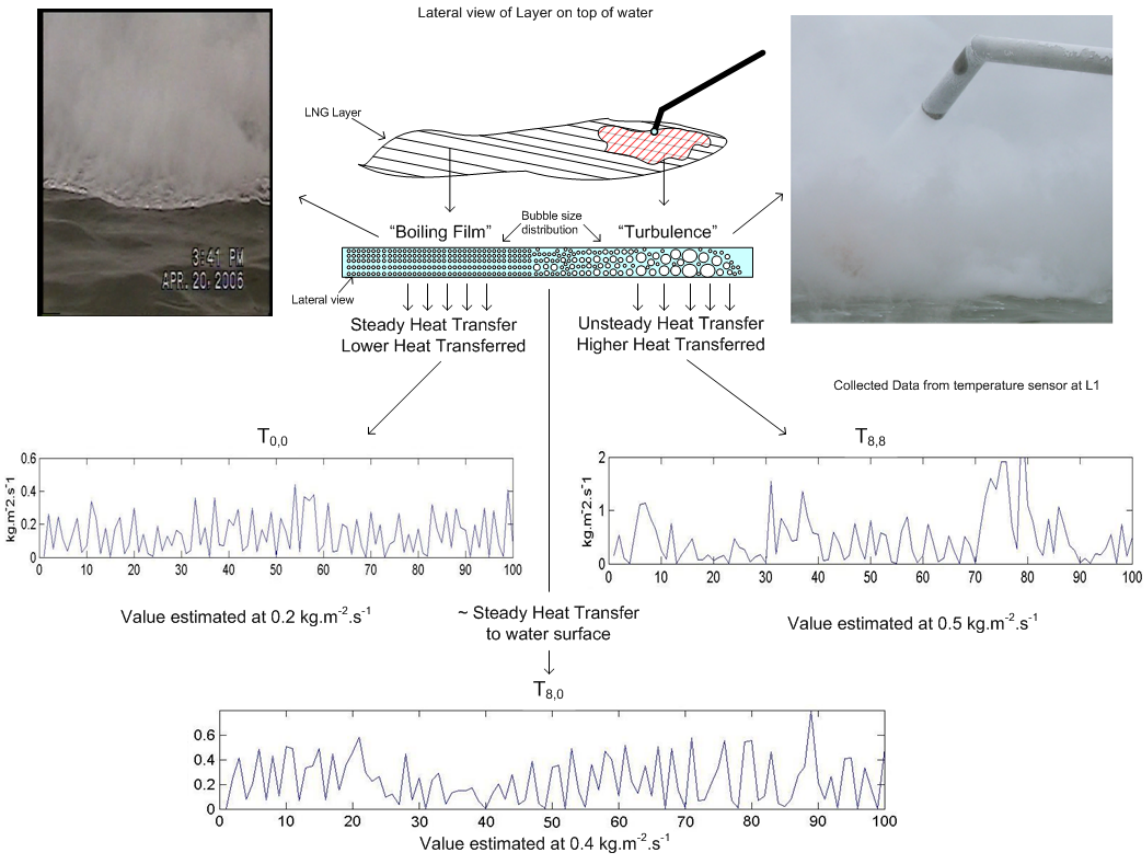

Figure 34. Lateral view of LNG layer and behavior description of mass evaporation rate

Figure 34 shows the lateral view of LNG Layer and the change in the mass evaporation rate with respect to the states of the layers. The interface is characterized by the contact between LNG and water, this contact is then translated into heat transferred. There are three main regions noticed:

- The unsteady region (i.e. landing area near the LNG source), the momentum created a stronger mixing effect between the water and the LNG, thus leading to the formation of bubbles and a high fluctuation in the estimated mass evaporation rate (i.e. increase of surface area) , as shown in the graph $T_{8,8}$.

- The meta-stable region, the transition phase between the unsteady and steady region, where the LNG layer is becoming more calm and start spreading out better. Therefore the evaporation is more steady and reducing as shown in graph $T_{8,0}$.
- The steady region, where the film evaporation is formed, reducing the heat transfer, therefore the mass evaporation rate is more stable as shown in the graph $T_{0,0}$.

3.1.6 Conclusions

It was observed during the filling a LNG pit, the mass evaporation rate changes over time. The release of LNG onto warm concrete results in a higher mass evaporation rate. While the pit is cooled, the mass evaporation rate slowed down to a steady mass evaporation rate as demonstrated in Figure 21. The foam test in 2005 revealed that the foam applied on the top of LNG initially increases the mass evaporation rate. It was observed that high expansion foam have a tendency to diminish over a short period time after its application. This could explain the increase of mass evaporation rate. As the foam breaks down into water and solution, the water acts like an agent that warms the LNG under the foam facilitating LNG evaporation off further. The foam tests in 2006 revealed that the foam applied onto LNG spread over water reduces the horizontal % LFL concentration. Therefore it reduces the downwind distance corresponding to LFL shown in Figure 28. A general observation can be derived from the 2005 and 2006 tests. Foam application on LNG increases the mass evaporation rate instantaneously. Then the LFL distance was reduced significantly. In general when LNG is released onto the ground, the LNG vapor cloud initially has negative buoyancy which means that it is denser than air. Therefore the vapor cloud migrates at ground level till its buoyancy becomes positive by absorbing heat. While the methane is traveling through the foam layer, it gets heated, which means that the methane gas expands. The buoyancy of the methane vapor increases through the foam. Once the buoyancy is positive, the vapor cloud goes upward instead of downward or horizontally. Therefore it reduces the LFL distance shown in Figure 27. The water curtains used in April 2006 shows their effectiveness in the reduction of downwind distance for vapor cloud of methane.

The cooled water underneath the LNG layer sinks and pushes up the warmer water to the surface of the pool. This effect creates a current inside the pit and prevents the formation of ice underneath the LNG layer for the LNG flow rate. In the case of confined release, ice formation slows down the mass evaporation rate because the heat transfer is reduced from water to LNG layer. In previous unconfined release tests, a mean mass evaporation rate was estimated through visual control of the pool diameter. During LNG release, the condensate vapor makes this measurement really difficult and inaccurate. During April 2006 test, the temperature profile helped to estimate the mass evaporation rate instead of a visual measurement of the pool diameter. The mass evaporation rate was estimated by calculating heat transferred from the LNG layer to the water. The mass evaporation rate was estimated to be between 0.2 kg/m^2 s and 0.8 kg/m^2 s depending on the region of turbulence. 0.8 kg/m^2 s was estimated almost underneath of the pipe where the LNG was shooting in. 0.2 kg/m^2 s was estimated at the tail of the LNG pool where the LNG is clamed onto the water surface. The previous reported values from the laboratory tests and theoretical calculations agree only when the LNG layer is spreading quietly onto water and the film evaporation is dominant. The momentum created at the discharge hose increased the interaction between gas and water. Therefore the estimated mass evaporation rate was greater than the mean values presented in Table 3, which are from the open literature. Once the LNG was spreading quietly, there was a good agreement with the values estimated during previous tests within the uncertainties of these experiments. Most of the software uses a mass evaporation rate of 0.2 kg/m^2 s that is the mass evaporation rate once the LNG is calmed onto the surface of the water. In case of a large release, the variation in the mass evaporation rate could have a significant impact on subsequent vapor dispersion modeling. Today, most of the simulations assume a constant mass evaporation rate. The use of uniform values does not represent the real behavior of LNG is released onto water. A more realistic source term should be integrated into vapor dispersion modeling

3.2 November 2007 test

After the analysis of April 2006 test, the November 2007 test was designed to assess the source term (mass evaporation rate on water) and the vapor dispersion with obstacles (to be used in

CFD modeling). The BFTF's LNG site was setup as described in Figure 35 to address the areas of interest.

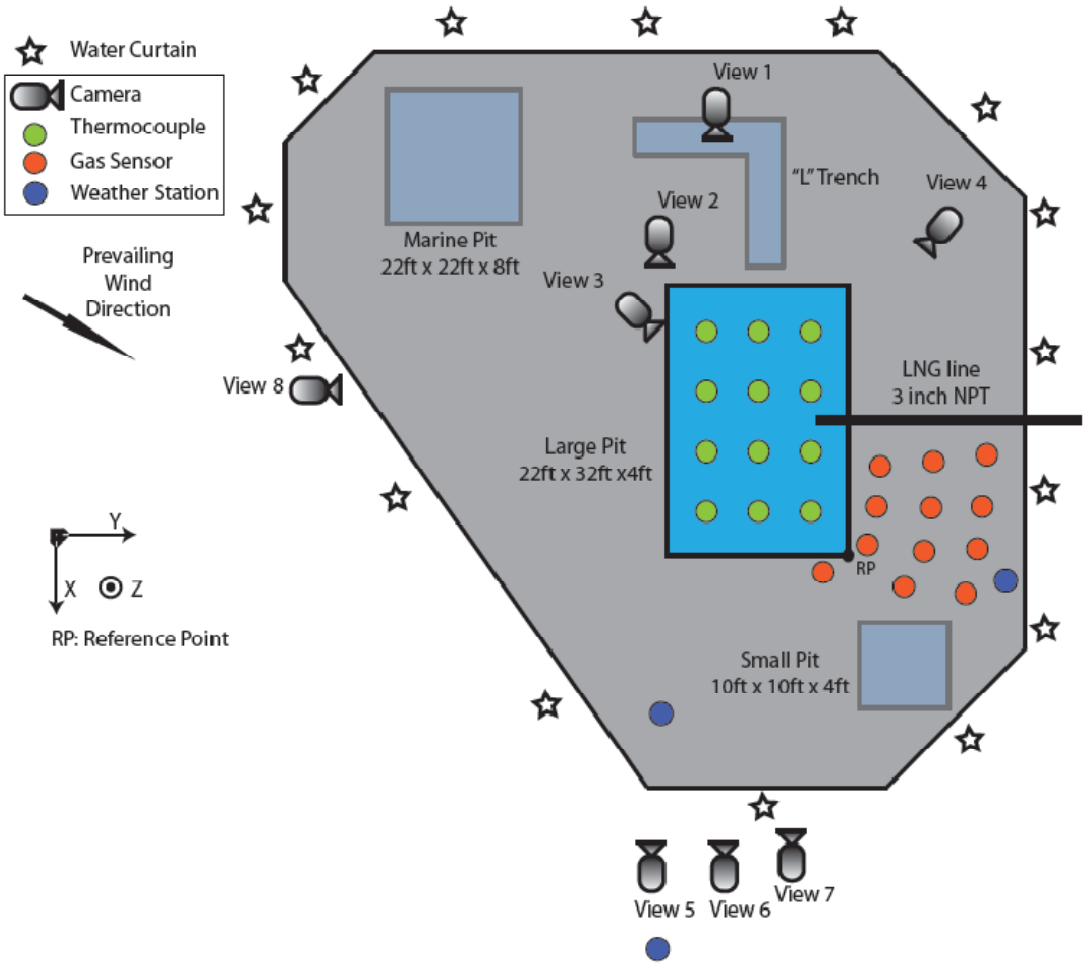

Figure 35. Facility siting at BFTF LNG project

Temperature and concentration were recorded through data acquisition system (DAS) to two computers located on the safe zone, where no personnel protection equipment is required. Various types of cameras were installed around the release area, including thermal imaging, hydrocarbon, regular, and high velocity camera.

The large pit was chosen in order to create a free-spreading LNG pool on water (no interaction with the boundary of the pit). A large quantity of water was needed to simulate an infinite source of heat sink for the LNG pool. Since the pit is only 1.3 meter (4 ft) deep, an additional 1.3 meter (4 ft) high vapor fence was provided with wooden walls to obtain a total of 2.6 meters (8 ft) in depth. The test setup is described in Figure 36. Prior to the release, the pit was filled with 1.3 meter of water.

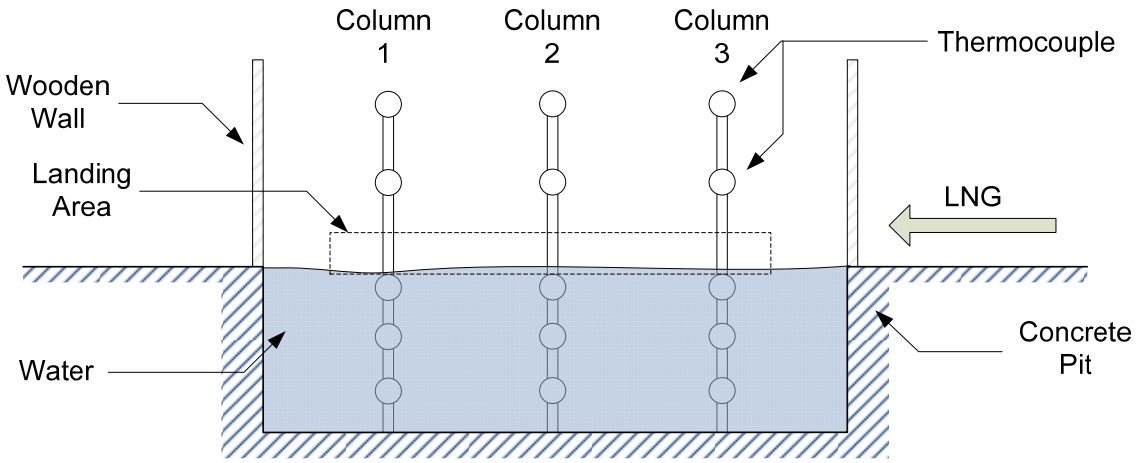

Figure 36. Scenario scheme for release on water in the large pit, TEEX1 and TEEX2

The photographic representation of the site is shown in Figure 37. This picture illustrates the metal frame, the ramp, and the thermocouples used for the pool size estimation. The metal frame was used to install thermocouples inside the pit. The level of the water was very close to the edge of the concrete pit, which covers three out of the five thermocouples on each column and leaving two thermocouples above the water surface to measure the vapor cloud temperature, as illustrated in Figure 36 and Figure 37. The vapor fence was 1.3 meter high above the water surface. The size of the discharge pipe was 3 inch NPT and was positioned at a 45 degree angle. A ramp to reduce vertical the momentum created by the discharge pipe diameter was also added to the site. In addition, thermocouples were placed horizontally close to water surface near to the LNG landing area in order to record the size of the LNG pool. The vapor cloud data was collected downwind from the point of release. Poles (with white and

orange strips) were located in the downwind area and they were used to hold the tube sampling lines for hydrocarbon concentration measurement. Foam generators were placed on the crosswind side in case of any unwanted ignition. One of the three weather stations was located on downwind area with the poles.

Figure 37. Setup for release on water

3.2.1.1 Temperature measurement

The temperature changes inside the pit were recorded with thermocouples on the frame. Because of the quantity of thermocouples in the pit, a numbering system was developed to track the temperature changes at different locations. Table 11 describes the names (identification numbers) and locations of the thermocouples inside the pit.

Table 11. Thermocouples matrix identification number and location on the metal frame

X (m)→	*T1 (-8.6)*			*T2 (-6.2)*			*T3 (-3.8)*			*T4 (-1.4)*		
y (m)→,	*L1-1*	*L1-2*	*L1-3*	*L2-1*	*L2-2*	*L2-3*	*L3-1*	*L3-2*	*L3-3*	*L4-1*	*L4-2*	*L4-3*
	(-5.3)	*(-3.3)*	*(-1.4)*	*(-5.3)*	*(-3.3)*	*(-1.4)*	*(-5.3)*	*(-3.3)*	*(-1.4)*	*(-5.3)*	*(-3.3)*	*(-1.4)*
Z (m)↓												
P5 (-0.6)	5	10	15	5	10	15	5	10	15	5	10	15
P4 (-0.4)	4	9	14	4	9	14	4	9	14	4	9	14
P3 (-0.1)	3	8	13	3	8	13	3	8	13	3	8	13
P2 (0.6)	2	7	12	2	7	12	2	7	12	2	7	12
P1 (1.2)	1	6	11	1	6	11	1	6	11	1	6	11

In this table, the thermocouple name and locations are indicated. This notation is used to describe individual thermocouple, horizontal, vertical plan and column of thermocouples. Four rows (T1 to T4), with 15 thermocouples on each row (numbering from 1 to 15), were used during the test. The number indicated in parentheses is the coordinates in meters in the Cartesian coordinate system using (x, y, z) and the reference point (0, 0, 0) shown in Figure 37, with z-coordinates equal to zero at the ground level. For instance, T3-9 is the thermocouple located at (-3.8, -3.3, 0.6) coordinates frame, in meters. T3-9 is located in column L3-2 and the horizontal plan P-4.

3.2.1.2 Hydrocarbon concentration measurement

Hydrocarbon point gas sensors (model Searchpoint Optima Plus) manufactured by Honeywell Analytics were used for gas concentration sampling. Searchpoint Optima Plus is an infrared point flammable hydrocarbon gas sensor. These gas sensors originally have a range of 0 to 100 % LFL (i.e. 0 to 5 %v/v) of methane, but they were modified to measure of 0 to 100 %v/v of methane for the purpose of this test. Each hydrocarbon point gas sensor is connected with a 3-wire 4-20mA source output to the DAS. The modification of the range increases the uncertainties associated with the low reading (lower than 5 %v/v).

Forty hydrocarbon point gas sensors were used during the test to measure gas concentration. Samples were pulled from the sampling location, with a vacuum pump into the high concentration cell of the gas sensor using 33 meters long Teflon tubing. Figure 38 shows the detail configuration of the gas sensor. This sensor requires about five watts to power the

heater to eliminate any humidity in the cell. Each gas sensor was calibrated with a gas air mixture of 50% methane prior the test and controlled between the tests. The flow rate provided by the vacuum pump was calibrated at 0.3 liter per minutes (LPM) to obtain an accurate reading for each sensor.

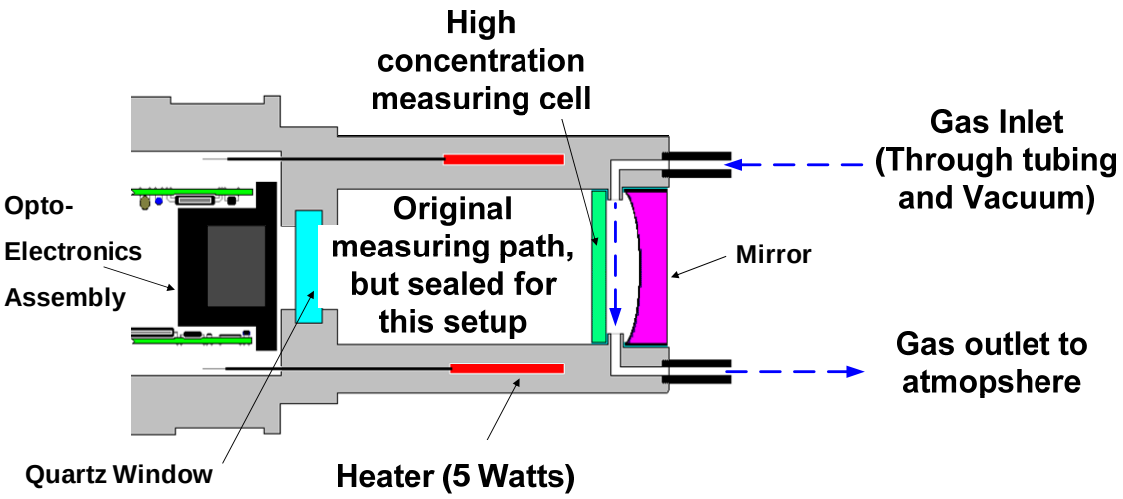

Figure 38. Details on gas sensors, modified from (Honeywell, 2004)

Gas sensors were installed on the poles at different downwind distances from the release pit at different elevations. For the release on water, the location is presented in Table 12. For instance, GD20 was located at (-2.8, 7.4, 1.3) using (x, y, z) coordinates frame at the reference point shown in Figure 35.

Table 12. Location of the array of sensor from the reference point

Pole #	*Gas sensor position*				*Position on grid*	
	Low	*Bottom*	*middle*	*Top*	*X, m*	*Y, m*
Z, m →	*(0.5)*	*(1.3)*	*(2.3)*	*(3.3)*		
GS01	-	GD02	GD01	-	1.2	-1.2
GS02	-	GD05	GD04	GD03	0.4	-0.4
GS03	-	GD08	GD07	GD06	-1.8	0.7
GS04	-	GD10	GD09	-	-3.8	0.8
GS05	-	GD12	GD11	-	6.6	-1.9
GS06	-	GD14	GD 13	-	4.9	-0.2
GS07	-	GD21	GD16	GD15	2.3	2.3
GS08	GD22	GD18	GD17	-	-0.2	4.9
GS09	-	GD20	GD19	-	-2.8	7.4
GS11	-	GD32	GD31	-	8.4	2.9
GS12	-	GD26	GD25	-	5.6	5.6
GS13	-	GD28	GD27	-	3.9	7.3
GS14	-	GD30	GD29	-	1.0	10.3
GS15	-	GD24	GD23	-	5.8	13.5
GS16	-	GD34	GD33	-	7.3	10.3
GS17	-	GD35	GD36	-	10.7	10.7
GS18	-	GD38	GD37	-	13.7	7.7
GS19	-	GD40	GD39	-	17.1	4.3

3.2.1.3 Wind field measurements

The wind field measurements were obtained using commercially available three axis cup and vane anemometers located in several locations. This product is available at Davis Instruments. It was used with three complete weather stations located at 2.3 m (2 units) and 10 m (1 unit) and locations are presented in Figure 35. The weather station included the following parameters, rain collector, temperature, humidity sensors, anemometer, solar radiation sensor, and UV sensor.

3.2.2 Test procedure

Prior to the release, the DAS was started five minutes before. This helped to perform a least equipment check and record variables before the release. Once the system was checked, LNG

valve at the bottom of the truck was opened. Monitoring of the data recording was an important part of the test to evaluate the presence of LNG on the water. Once the LNG pool was noticeable on the water, the release was kept continued for ten minutes. Thermal imaging and hydrocarbon were also started about 15 minutes prior to the test. High velocity camera was only used at the beginning and end of the test to record any LNG pool formation. This test was performed twice with an interval of one hour and the tests were called scenario TEEX1 and TEEX2. The interval between the two tests was essential for the water in the pit to warm up.

3.2.3 Analysis and discussion

The analysis and discussion is separated into wind field, mass balance on LNG, the temperature profile of the water and then the concentration downwind. The wind field is mainly focused on the derivation of the parameters needed for modeling the wind conditions during the tests for the specific site, BFTF. The temperature profile is used to determine the parameters associated with source term such as mass evaporation rate, shape and size of the pool. Finally the last section transits to the formation of the hydrocarbon vapor cloud, and the study of the downwind concentration profile.

3.2.3.1 Wind field

BFS has a designed area for LNG release and it is located further South(S) of the complex. The props are composed of concrete surface surrounding with buildings, a lake and trees. The estimated roughness is 0.00085 m. This value was estimated through the study of the wind profile. On the S of the LNG props, the terrain is composed of flat ground with no/low grass, river and then trees, as shown in Figure 39. The North of this site is composed of parking area and open storage area, which are emptied during any LNG release training.

Figure 39. Aerial view of BFTF (courtesy of Kirk Richardson, TEEX)

Historical data of November shows the range of temperature from 4 degrees Celsius to 24 degrees Celsius with a mean value of 12 degrees Celsius. The range of wind velocity was from 0.0 to 13.0 m/s with a mean value of 3.4 m/s along with a prevailing wind from the S. It is been noticed in the case of low wind velocity that the wind direction is inconsistent. For instance, during TEEX2, the wind was blowing from the S to E making the hydrocarbon vapors going outside of the array of sensors.

The location of the weather stations is presented in Figure 37. The data were averaged every minute. By using the following equations, the parameters are estimated for each period of interest, TEEX1, and TEEX2. This data is presented in Table 13.

Table 13. Mean values for weather conditions summary

Test Name	*TEEX1*	*TEEX2*
Mean Wind Velocity @ 2.3 m, m/s	1.2±0.38	2.3±0.23
Mean Wind Direction @ 2.3 m, m/s	160±18	140±34
Wind profile		
At 2.3 m	1.2±0.38	2.3±0.23
At 10 m	1.9±0.58	3.3±0.78
u_*, *m/s*	0.053	0.175
Temperature Profile		
At 2.3 m	15.9±0.26	16.5±0.61
At 10 m	15.9±0.19	16.8±0.71
$T_0(z) - T_w$, ^oC	0.024	0.10
Absolute air pressure, bar	1.013±0.001	1.012±0.001
Relative Humidity, %	32.6±1.6	31.2±1.2
Dew Point, ^oC	30.8±0.98	31.8±0.97
Stability Class (judged)	B	C
Solar Radiation, W/m^2	593.7±48.9	704.4±10.4
Sensible heat flux, W/m^2 *with Eq. (36)*	1.54	44.8
Heat diffusivity @ 2.3 m with Eq. (38)	0.024	0.30
Momentum diffusivity @ 2.3 m with Eq. (37)	0.021	0.30
Richardson Number @ 2 m with Eq. (39)	0.24	0.026
Monin-Obukhov length, m with Eq. (34)	8.3	85.8
Roughness length, m	0.00085	0.00085

The friction velocity, scaling potential temperature, zero level temperature, and the Monin-Obukhov length are determined from a least square fitting of the wind velocity profile and potential temperature profile data to the assumed velocity profile function (Davies & Singh, 1985). Following equations based on Monin-Obukhov (Panofsky & Dutton, 1984) formulation, the atmospheric conditions for the wind velocity and temperature may be derived as function of vertical axis.

The values presented in Table 13 are mean values. For the purpose of simulating a transient profile with a computational fluid dynamics code for the temperature and the concentration downwind, the mean values may not be appropriate. The wind profile should be determined from the data collected and its variability should be expressed through a function of time.

3.2.3.2 Material balance

LNG is brought by a 41 m^3 LNG tanker to BFTF each time a training or test is required. A stainless steel pipeline is used to deliver LNG from the tanker to the LNG props. Then flexible

hoses are used to discharge the LNG into the pit of interest. The LNG composition in the tanker truck is 99.8% methane (commercially available), hereby the hydrocarbon vapors are mainly composed of methane. The temperature and pressure are kept at 1 bar and 110 K in the tanker truck.

Due to the specification of this discharge line, some of the LNG flashes before reaching the discharge hose. Study (Cormier, 2007) has shown that 5 to 15 % hydrocarbon vapors may be produced along the pipeline due to heat transfer from the pipeline. This number will be assumed constant for the rest of analysis since this fraction was not measured during the test. Therefore the velocity of the fluid may be estimated for the liquid and for the flashing gas in Table 14. For TEEX1 and TEEX2, a ramp was used to eliminate the vertical liquid phase velocity that may result in increasing the heat transfer at the impact area when penetrating and mixing with water. On the other hand, the horizontal liquid phase velocity was conserved.

A cryogenic flow meter (turbine type) was placed at LNG tanker to record the LNG flow. The turbine was placed at the beginning of the pipeline where the hydrocarbon vapor was minimal from the flash effect. High volume of gas will create turbulence in the reading or even false the reading. Table 4 shows the summary of LNG flow during these two tests. The flow was controlled by gravity inside of the tank and the pressure above the liquid. As the level of LNG was changing in the tank, the output flow was varying, creating some turbulence in the reading. Hereby mean values are presented in the table.

Table 14. Summary of LNG flow

Test name	*TEEX1*	*TEEX2*
Mean flow rate, m^3/min	0.75 ± 0.09	0.63*
Valve open time, sec	619	763
Quantity Release, m^3	7.7	8.1

*No Data, estimated from total volume

3.2.3.3 Water temperature profile

3.2.3.3.1 Pool size and shape

The pool size and shape was determined by using the thermocouples at the water surface. The thermocouples, on P-3 according to Table 11, were placed on the metal frame, and the coordinates are shown in Table 11. In addition, twenty thermocouples were installed horizontally between L2-2 and L3-2 (noted TN-1 through TN-20), to provide more details on the pool formation. Thermocouples noted TW, were on the edge of the pool in the vapor fence at different heights. The temperature contour of the water surface was derived by using interpolation among the locations of thermocouples (blue dots). Figure 40 shows the results from the contour during TEEX1 and TEEX2 when the pool reached the steady state.

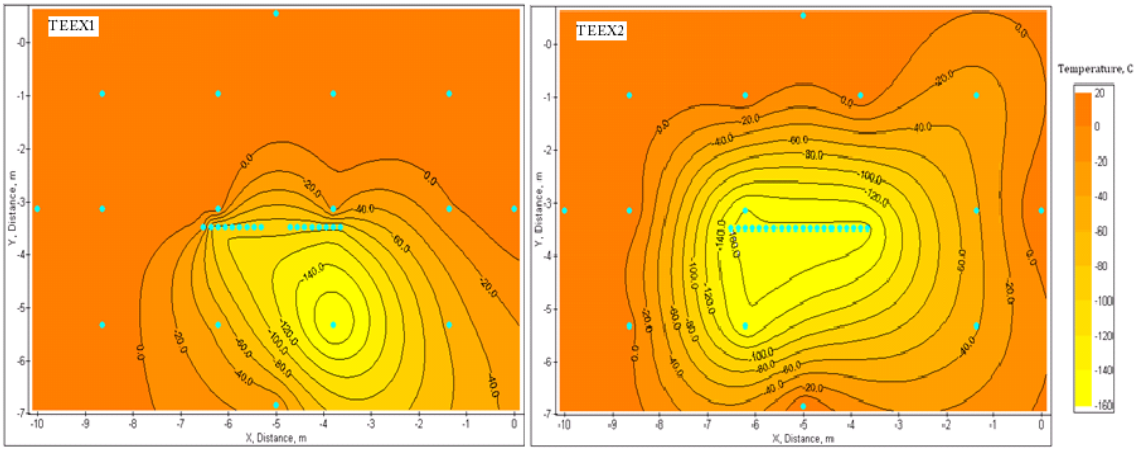

Figure 40. Temperature profile at the interface between LNG and water for TEEX1 and TEEX2

The LNG pool size was estimated by assuming that LNG was present for the values less than zero degree Celsius. By definition, water at standard conditions freezes when the temperature goes under zero degree Celsius. Between TEEX1 and TEEX2, some thermocouples did not work right. In the case where the data were missing, the dot marking location was removed and no data were computed into the interpolation. For TEEX1, the center of the pool was located at L3-1 rather than in between L2-2 and L3-2 as predicted. For TEEX2, the center of the pool was

located mainly in center of the pit, between L2-2 and L3-2 and the LNG pool was more evenly spread over the surface area.

Figure 41 shows the pool area estimation based on the temperature contours. On both test data, experiment times were adjusted for easy comparison. Unfortunately some of TEEX1 data were lost at the beginning of the test. The size of the LNG pool was larger in case of TEEX2 compared to TEEX1.

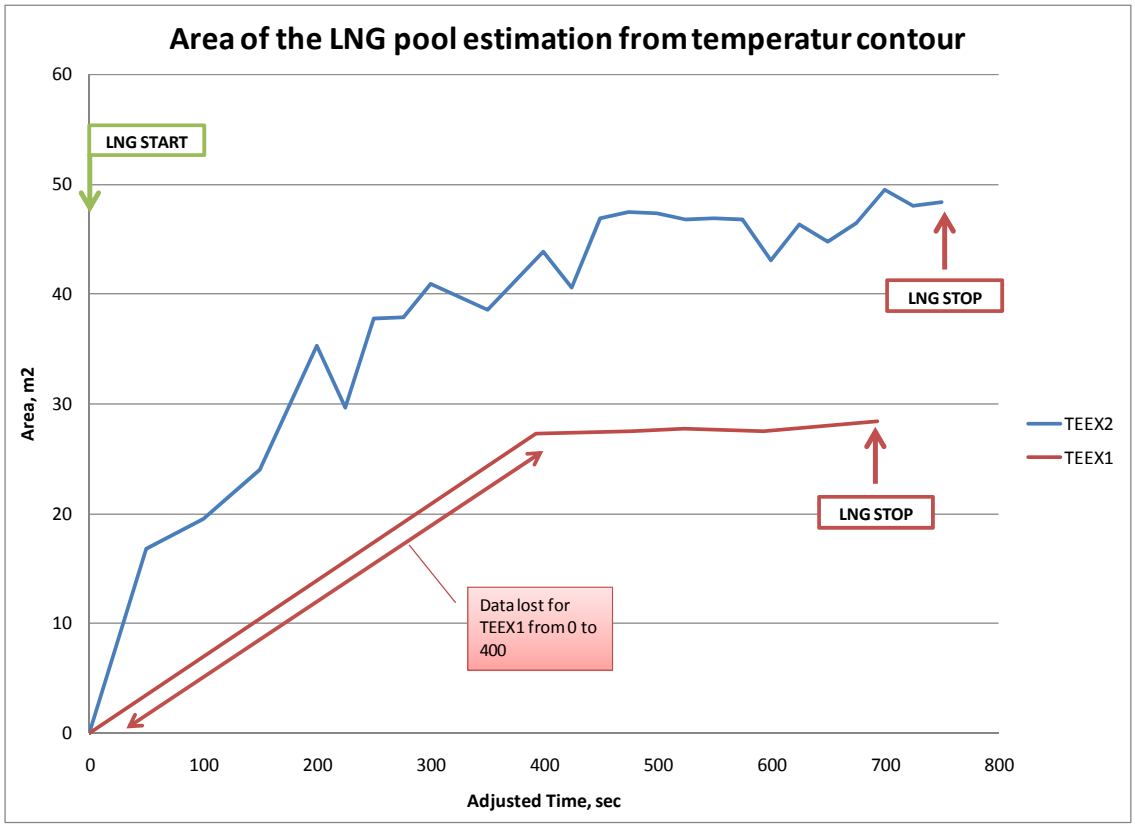

Figure 41. Area of the pool based on temperature profile

Figure 41 shows the area of the pool over the time of the release for each run. The total water surface is 67.5 m^2. TEEX1 reached a steady pool area of 27.6 ± 0.4 m^2 for a period of 300 seconds (from 400 to 700 seconds). On the other hand, TEEX2 reached a steady pool area of

46.8 ± 1.6m^2 for a period of 200 seconds (from 450 to 650 seconds) and slowly increased to 49 m^2.

Two possible causes might lead to the difference in location and size of the pool. (1) The pipeline was not pre-cooled before conducting TEEX1, which reduced liquid flow rate at the discharge hose until the pipeline was completed cooled down. (2) The pool location may have been influenced by the formation of a hydrate/ice, shown in Figure 42. The aftermath pictures show the leftover from the pool spreading right after the vapor disappeared. For TEEX1, a LNG pool formed above water; for the moment that the cryogenic pool was present on the water surface, only pieces of hydrate were formed. The LNG pool was moving freely on the water surface due to a gradual increase of the flow rate, the horizontal liquid phase velocity created by the discharge hose and the absence of hydrate formation. The pool was relocated to the upwind wall. For TEEX2, a LNG pool formed more rapidly than in TEEX1 caused by higher liquid flow rate. LNG pool was located in the middle of the pit among L2-2, L2-3, L3-2 and L3-3. As the pieces of hydrate formed on the water surface, the frame poles may have acted as anchor point for the pieces of hydrates. Over time, it created a large hydrate shown in Figure 42.

Figure 42. Picture of the pool area after the release is completed, TEEX1 and TEEX2

In TEEX1, the liquid flow rate out of the discharge hose was gradually increasing as the pipe was cooled down; therefore there was no hydrate formation. In TEEX2, the liquid flow rate out of the discharge was maximized as the discharge hose pipe was already cooled down; and high

liquid rate increased the formation of the hydrate. Small flow rate may only form pieces of hydrate. This indicates in a case of instantaneous large LNG release over large quantity of water, the hydrate may form right away.

3DField Pro has different options in the methodology to interpolate the data in between sensors. The uncertainty associated the methodology employed is shown in Table 15. Two methodologies, Kriging and Triangular, interpolation were used to estimate the uncertainty with the interpolation methodology. The range of estimation may vary by more than 30%. A mean mass evaporation rate was derived from the area and the flow rate. More rigorous analysis of the mass evaporation rate is presented in the next section. The mean values illustrate the effect of the hydrate on the water and the reduction in heat transfer from underneath of the LNG layer. A hydrate may increase the size of the pool. In the case of large release, contribution of hydrate formation to pool formation may be significant.

Table 15. Pool estimation calculation methodology and derived mass evaporation rates

Test Name	*TEEX1*	*TEEX2*
Pool estimation Kriging, m^2	27.6 ± 0.4	46.8 ± 1.6
Pool estimation Triangular, m^2	20.8 ± 0.6	33.0 ± 0.7
Mean mass evaporation rate, kg/m^2 s	0.18 to 0.25	0.09 to 0.13

3.2.3.3.2 Mass evaporation rate profile

Mass evaporation rate was determined by using the pool area and the discharge flow rate. As shown in Table 15, the mean value of the mass evaporation rate depends on the methodology used, which questions the precision of these numbers. Nevertheless this information still gives mean mass evaporation rate estimation and a general feeling of the influence of hydrate.

On the other hand, by considering the heat transfer through the water, the mass evaporation rate at different locations may be determined. Thirty six thermocouples were placed underneath of the water surface to monitor the change of temperature during the release. These data was used to estimate the heat flux from the water to the LNG layer.

The mass flux (or mass evaporation rate, kg/m^2 s) was estimated by measuring the temperature difference in between the bottom two thermocouples on the frame. The distance between the two thermocouples was 0.33 meter (one foot). A mean temperature was estimated for this length by using the two thermocouple readings (thermocouples in P4 and P5 plan, respect to the notation). Mixing effects were created due to the cooled water moving down, thereby the temperature readings showed positive and negative changes. Only cooling effect (negative change) was considered to represent the mass flux from LNG pool. It was also assumed that the cooled water travels vertically (sinking) and not horizontally. The change of temperature was then estimated between time, *t* and time, *t+1* as shown in Equation 58. The mass evaporation rate of LNG pool is calculated with Equation 57 (Incropera & DeWitt, 2002). To reduce the noise in the data, once the mass evaporation rate were estimated from the temperature readings, the mass evaporation rate was averaged.

$$\dot{m}'' = \frac{\rho_w . l}{\lambda} . C_{pw} . \Delta T \tag{57}$$

where

$$\Delta T = \frac{\left[P5(t+1) - P5(t)\right] + \left[P4(t+1) - P4(t)\right]}{2} \tag{58}$$

C_{pw} = the heat capacity for water

ρ_w = the water density

λ = the LNG latent heat

$\dot{m}''$ = the mass evaporation rate

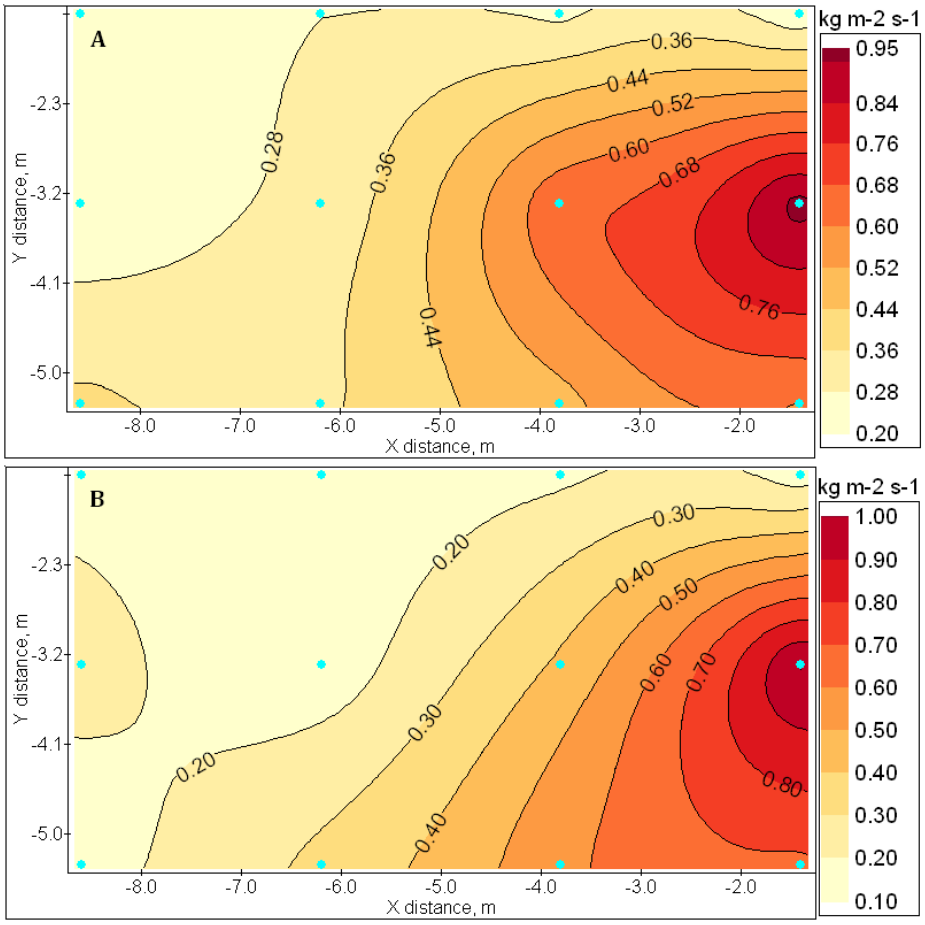

Figure 43. Mass evaporation rate contour for TEEX1, time (A) at 400 and (B) at 700 seconds

During TEEX1, the LNG pool area was stable from 400 and 700 seconds. Figure 43 shows the evaporation rate distribution for time at 400 and at 700 seconds. The mass evaporation rate contour was performed among of the thermocouple on the frame. At both time, the mass evaporation rate had the same features, the low mass evaporation rates were located on the edge of the pool (left side), and the high mass evaporation rates were mainly located on the right of the discharge hose confirming the results for the pool location. The mass evaporation rates values were between 0.20 to 0.95 $kg/m^2 s$ and between 0.1 to 1.0 $kg/m^2 s$ for time at 400 and 700 seconds, respectively.

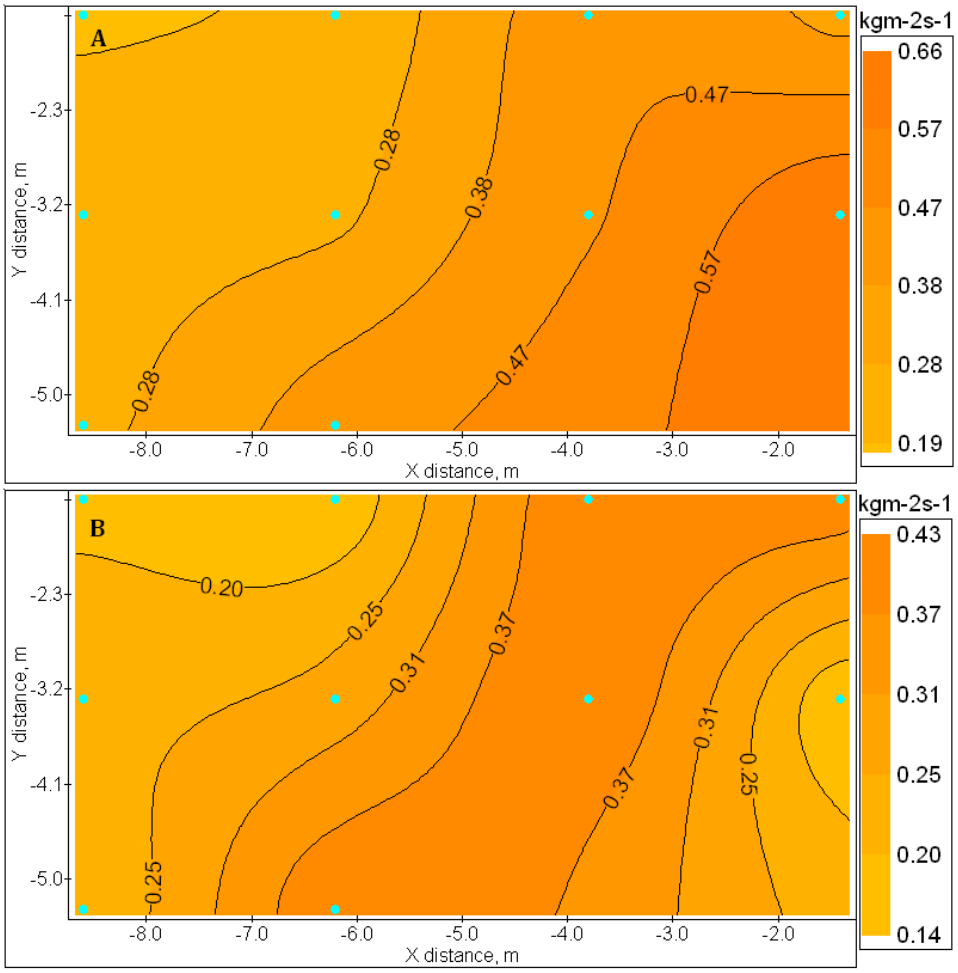

Figure 44. Mass evaporation rate contour for TEEX 2, time (A) at 300 and (B) at 700 seconds

Figure 44 shows the mass evaporation rate profile from the heat transfer calculations at 300 and 700 seconds. The profile had different features. The mass evaporation rates values were between 0.19 to 0.66 kg/m^2 s and between 0.14 to 0.43 kg/m^2 s for time at 400 and 700 seconds, respectively. At the beginning of the release, the high mass evaporation rate was located on the right side of discharge hose as seen in TEEX1. As the release reached 700 seconds, the high mass evaporation rate was re-located to the front of the discharge hose. The Figure 44 A and B illustrates the reduction of heat transfer through the water and relocation of the high mass evaporation rate of the hydrate/ice during the release.

The values presented also account for the sum of the phenomenon happening during the release such as convection heat transfer between gas/bubble and LNG, conduction heat transfer between water and LNG, evaporation and solidification of water/methane creating hydrate. It is also suspected that the horizontal liquid phase velocity may increase the turbulence along the path of spreading. The bottom part of LNG pool on contact with the water surface may break in droplets resulting an increase of heat transfer.

The mass evaporation rate was high during TEEX1 compared to TEEX2, and the physical difference were the hydrate/ice formation between TEEX1 and TEEX2. As the hydrate formed and the heat transfer was reduced (LNG and water contact decrease), the pool was spreading out more to regulate the equilibrium between total evaporation rate and the incoming of LNG onto water. The slow LNG liquid flow rate on water may provide a slow cooling of the water preventing the solidification between the water and LNG during TEEX1. On the other hand, higher liquid flow rate may have provided a fast cooling, which provoked the solidification during TEEX2. The energy used in the solidification may have influenced the temperature profile underneath of the hydrate/ice layer as well as the mass evaporation rate.

In general, the values estimated using the heat flux through the water was higher than the values calculated with the estimation of the pool area and the LNG flow rate. The mean value obtained was in the range of the open literatures. Table 8 summarizes the difference in the estimation of mass evaporation rate for LNG release on unconfined water. The values estimated with heat flux through the water were significantly higher during TEEX1 than TEEX2. They also illustrated an evaporation profile instead of a mean mass evaporation rate.

3.2.3.4 Concentration profile

During the release on water, there are two areas of interest for analysis, in between the wall of the pit above the water, and the downwind area. Only temperature was recorded in the pit area rather than gas concentration. For the sake of this analysis, the temperature is converted to concentration by using a simplified model.

3.2.3.4.1 Inside the pit

As LNG was evaporating off from the water surface, the hydrocarbon vapors were accumulated inside the wall surrounding the pit before be entrained by the wind. Sensors placed above the water surface and around the wall provided valuable information regarding the temperature profile inside the walls. Only temperature data was collected inside the pit. For the purpose of analyzing the behavior of the cloud, the gas concentration inside the pit was determined using the following equation (Incropera & DeWitt, 2002):

$$\chi_{LNG}=\frac{C_{Pair}\Delta T_{air}}{C_{Pair}\Delta T_{air}-C_{PLNG}\Delta T_{LNG}} \quad (59)$$

where

ΔT_{air}: $T-T_{air}$

ΔT_{LNG}: $T-T_{LNG}$

C_{PLNG} = the eat capacity for LNG

T_{Air} = the ambient temperature

T_{LNG} = the LNG temperature

T =- the temperature probe

C_{Pair} = the heat capacity of air

ρ = the density of air

The derivation of the concentration from the temperature is more complex than expressed in Equation 59. The missing information was the temperature of the sample (where a composition may be associated to a density). By using three-dimensional contour plot software and Equation 59, the plot of isosurface at 10 and 25 % v/v is presented in Figure 45. The isosurface represents the surface where the concentration is the same.

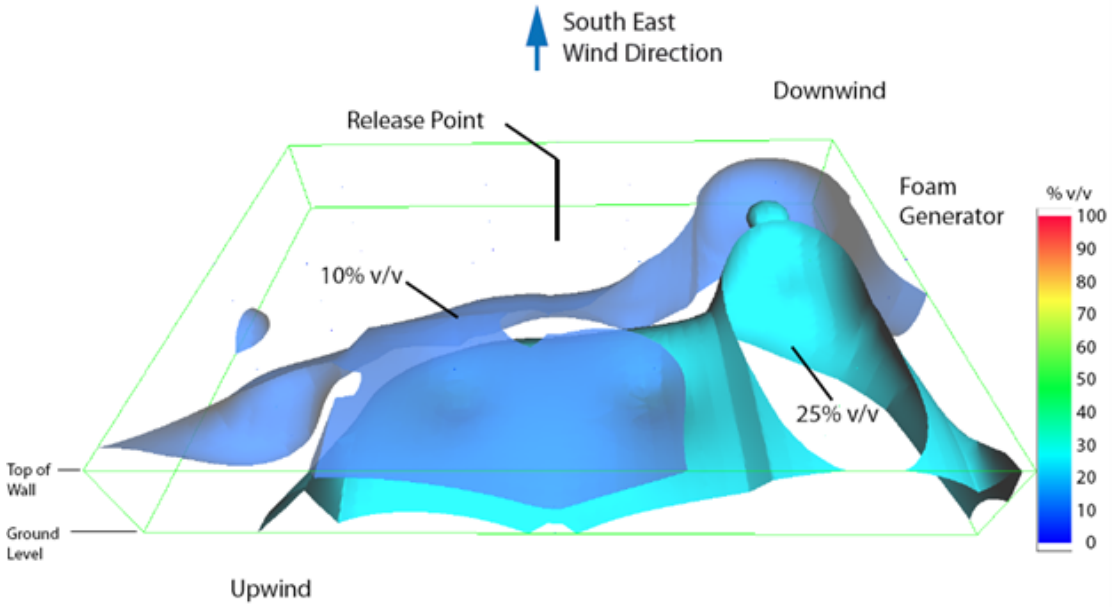

Figure 45. Isosurface inside the pit at 10 and 25 % v/v, TEEX1

Figure 45 shows the concentration profile based on the temperature during TEEX1. The perspective view shows the calculated concentration of methane in between the water line (at the ground level) and the top of the wall. The release point was located in the middle of the downwind wall and about one meter inside the pit at water line. Foam generators were located on the right side of the current view. The wind was blowing from upwind to downwind with a light angle towards the foam generators (S direction).

The two isosufaces represent a high and low concentration cloud. Low concentration isosurface may cover a larger area than a high concentration surface. Thereby, the two selected concentration profile helps the reader to visualize the feature of cloud at the source and from the surroundings.

The high concentration isosurface shows the location of the evaporating pool and also covered the area estimated from the temperature profile at the water surface shown in Figure 40. The geometry of the isosurface shows the cloud rising evenly from left to the right, where the surface reached the top boundary. The "cut" of the 25 % v/v surface shows that the rest of isosurface went beyond the top boundary. This shape may be explained through the high mass

evaporation rates calculated. High mass evaporation created a high gas phase velocity. In the absence of external turbulence, the mass evaporation rate profile will influence the concentration profile. In addition, the foam generators, which were located above this area, may act as a shield from the external turbulences such as the wind.

Low concentration surface may bring up different features from the cloud which are not noticeable with a higher concentration surface. The low concentration surface illustrates the interaction with the wall as the methane gas rises. The hydrocarbon vapors accumulated against the upwind wall, where they were entrained by the wind as the hydrocarbon vapors went above the edge of the upwind wall. According to the isosurface, the main body of the cloud occupied half of the entire volume near the foam generator and the upwind wall. Most of the vapors originated from the upwind wall and entrained by the wind are shown in Figure 46. The white cloud represents the condensate vapors from the humidity in the air which may or may not represent all the hydrocarbon vapors.

Figure 46. Illustration of interaction between the edge of the wall and the condensate cloud

The same perspective for TEEX2 is shown in Figure 47. The isosurfaces chosen are 10 and 30 % v/v. The high concentration surface shows the location of the pool and also corresponds to the estimated area shown in Figure 40. Due to a larger LNG pool formation, the body of the cloud occupied a greater volume than during TEEX1. The high concentration surface was inside the defined domain and it did not get "cut". The evaporation rates were lower and have less variation over the LNG pool (i.e. between 0.14 to 0.43 kg/m^{2}s instead of 0.1 to 1.0 kg/m^{2}s for TEEX1). The low concentration surface had the same trend as TEEX1, where the methane gas accumulated against the upwind wall before to be entrained by the wind.

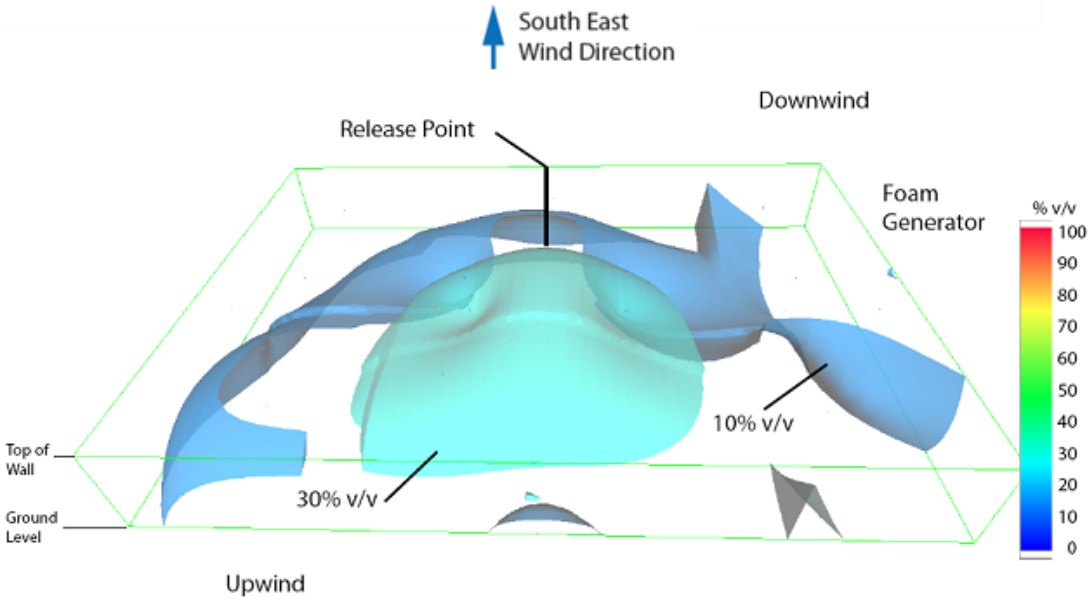

Figure 47. Isosurface inside of the pit for 10 and 30% v/v methane , TEEX2

3.2.3.4.2 Cloud characteristics

TEEX1 was considered to be at the low wind velocity with a class stability judged at B with Pasquill-Gifford class (Pasquill, 1978). The wind was mainly traveling from South East (SE) to S for most of this test period. The array of sensors in the downwind was oriented towards S (180) with an angle of 90 degree, starting at SE (135) to South West (SW, 225). However, the wind shifted resulting in having the edge of the cloud been outside of the sensor area during

the test while the centerline of the cloud was mainly inside the array of gas sensors. During data analysis of the plume characteristics, the LFL cloud stayed inside of the array of sensors. The half LFL cloud was definitely outside of the array of sensors, which indicated that the sensors could have been placed further downwind. The LFL and half LFL distance were obtained by using 3DField Pro. TEEX1 cloud was interesting because of the very low wind velocity condition (below 1 m/s). The absence of strong wind permitted the movements of the cloud due to the gravity and the upward gas phase velocity. It was fairly noticeable the upward gas phase velocity located at the edge of the upwind wall shown in Figure 46. During the "no wind" moment, the initial upward movement, mainly from the gas phase velocity, accumulates a large quantity of condensate white cloud above the release area. This accumulation was then slowly entrained by the wind once the wind velocity increases significantly. During this moment, it was almost noticeable that the cloud movement looked as if as stopped. This effect may be due to the velocity created by the evaporation rate. With a "no-wind" condition, the hydrocarbon vapors moved vertically until the initial upward momentum became neutral (the upward momentum became neutral because of the gravity and the hydrocarbon vapor density was still heavier-than-air), where the cloud looked like it had stopped. Once the wind picked up again, the accumulated cloud moved downwind and downward.

This phenomenon created a large cloud above the release area, illustrated in Figure 48. The approximate height was between 5 and 6 meters above the ground level and most of the cloud is traveling above the sensors. This height was reached partially because of the wall height, which gives a release location at 1.3 meters. The meander of the cloud was visually observable significantly during the release. Concentration of the hydrocarbon vapors were measured by the sensors placed at the ground level as the cloud approached downwind. This demonstrates the negative buoyancy effects associated with LNG release.

Figure 48. East view of the cloud during LNG release on water TEEX1

TEEX2 was considered to be moderate to high wind velocity with a class stability judged at C. During the release the minimum wind velocity was at 3 m/s, it reached a maximum at 7 m/s and decreased to 3 m/s. The flow rate of LNG delivered to the pit during TEEX2 was about 16 % less than the flow rate during TEEX1. The sensor location stayed the same as the ones on TEEX1. The wind shifted from E to S during the test. When the wind was coming from E, the centerline of the cloud is outside the array. When the centerline of the cloud was inside the array, the LFL cloud stayed inside the array of sensors and the half LFL cloud was definitely outside the array of sensors. The effect of the wind is shown in Figure 49. Higher wind have tendency to flatten the cloud shape. None of the "no-wind" effect was noticed during TEEX2. The approximated height of the cloud was about 4 to 5 meters. From the video footage, the white condensate plume of the cloud seems to be shorter than in TEEX1.

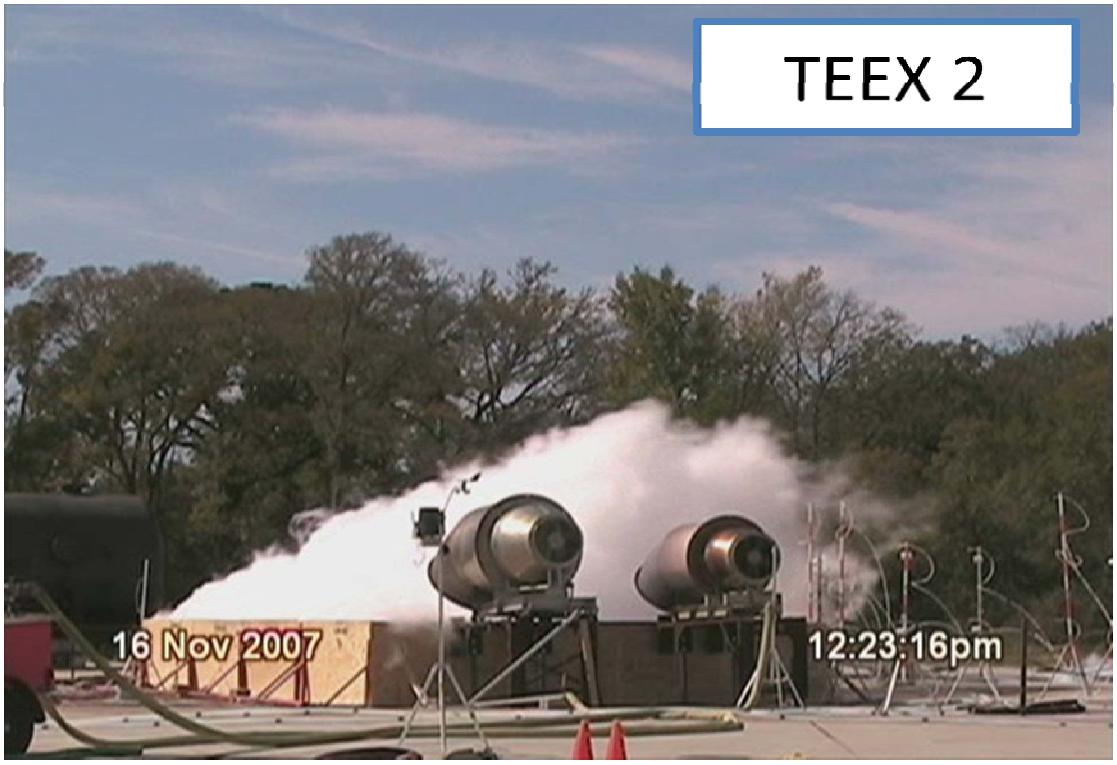

Figure 49. East side view during LNG release on water, TEEX2

A shorter visible plume may be the results of high wind velocity that may increase the mixing between air and cold hydrocarbon vapors while at the same time tilting the cloud. The concentration reading at the ground level was the same compared to TEEX1, up to 8% v/v at GD22.

3.2.3.4.3 Plume description

Before the release, the main wind direction was predicted to be toward S then the array of sensors was placed accordingly. The instability of the wind direction results on two different shapes of plume. The geometry of the wall and the foam generators represents the main obstacles, before the wind entrains the hydrocarbon vapors.

During TEEX1, the wind direction shifted from SE to S. The collected data is represented by using three-dimensional interpolation software. The concentration data was averaged every 10 seconds to reduce the fluctuation in the data. The boundaries of the volume were represented

by the location of the sensors respect to length, wide, and height (i.e. x, y, z). The data was plotted into a volume of 13.5 by 17 by 2.8 meters (from 0.5 to 3.3 meters above the ground). The location of the edge of the pit and the release location at (-4,-2) meters are represented in Figure 50. The data was interpolated between the points in the volume using a Kriging interpolation methodology, as shown in Figure 51. Then the volume was cut into planes along the z axis to obtain horizontal two-dimensional contours. The vertical plane (z direction) at 0.5 meters above the ground is shown in Figure 50.

During the SE wind direction, only part of the cloud was captured by the array of sensors. The shape of the cloud may be described like a typical shape of a plume (with no obstacle effects). The plume was wide in case of low wind (TEEX1) and narrow in case of high wind (TEEX2).

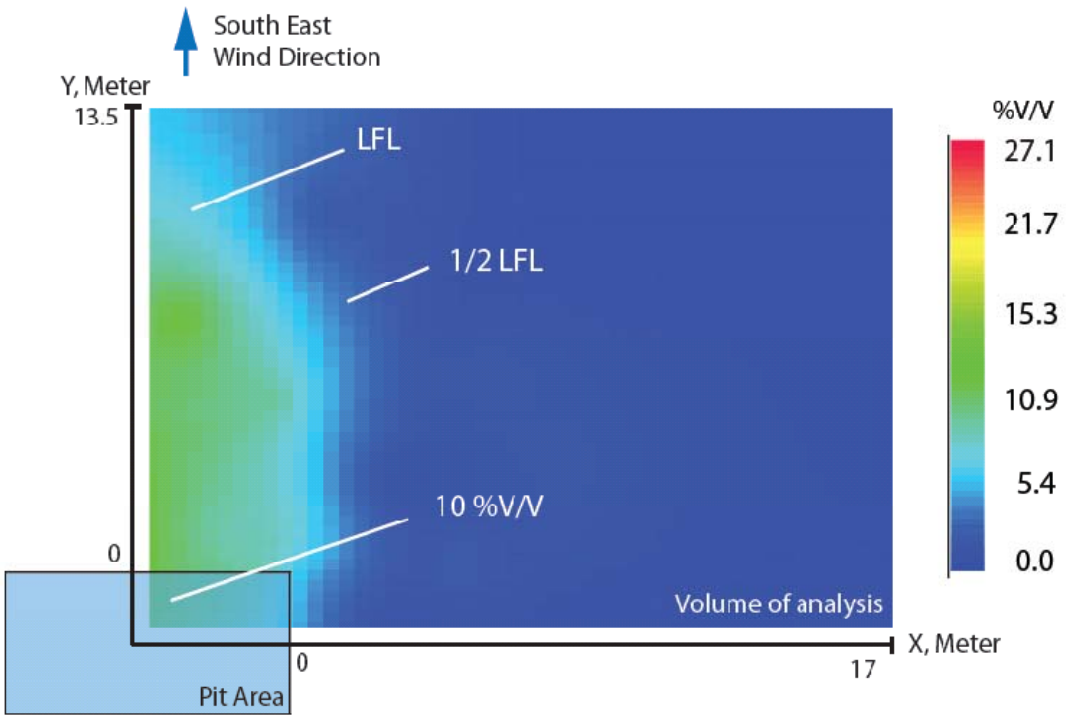

Figure 50. Two dimensional representation at ground level at 476 seconds, TEEX1

The concentration ranged from 0 to 27.1 % v/v with a wind velocity of 3 m/s. From the release point located inside the pit area, the LFL distance was estimated at 15.5 meters using the output file. The half LFL was extending outside of the current array of sensors. Figure 51 shows a three-dimensional representation of the downwind cloud using the same volume shown in Figure 50. The selected isosurface concentrations were 2.5 (half LFL), 5 (LFL) and 10 % v/v. Once the vapors passed over the top part of the wall located at 1.3 meters above the ground, the vapors then fell down to the ground level, at least to 0.5 meter above the ground where the lowest sensor was located. As the vapors progressed downwind, the vapors were diluted up to LFL concentration before leaving the sensors array. The shape of the half LFL cloud may suggest first the vapors falling down (the base of the cloud was larger than the top) and then the vapors were rising (the top of the cloud is wider than the base).

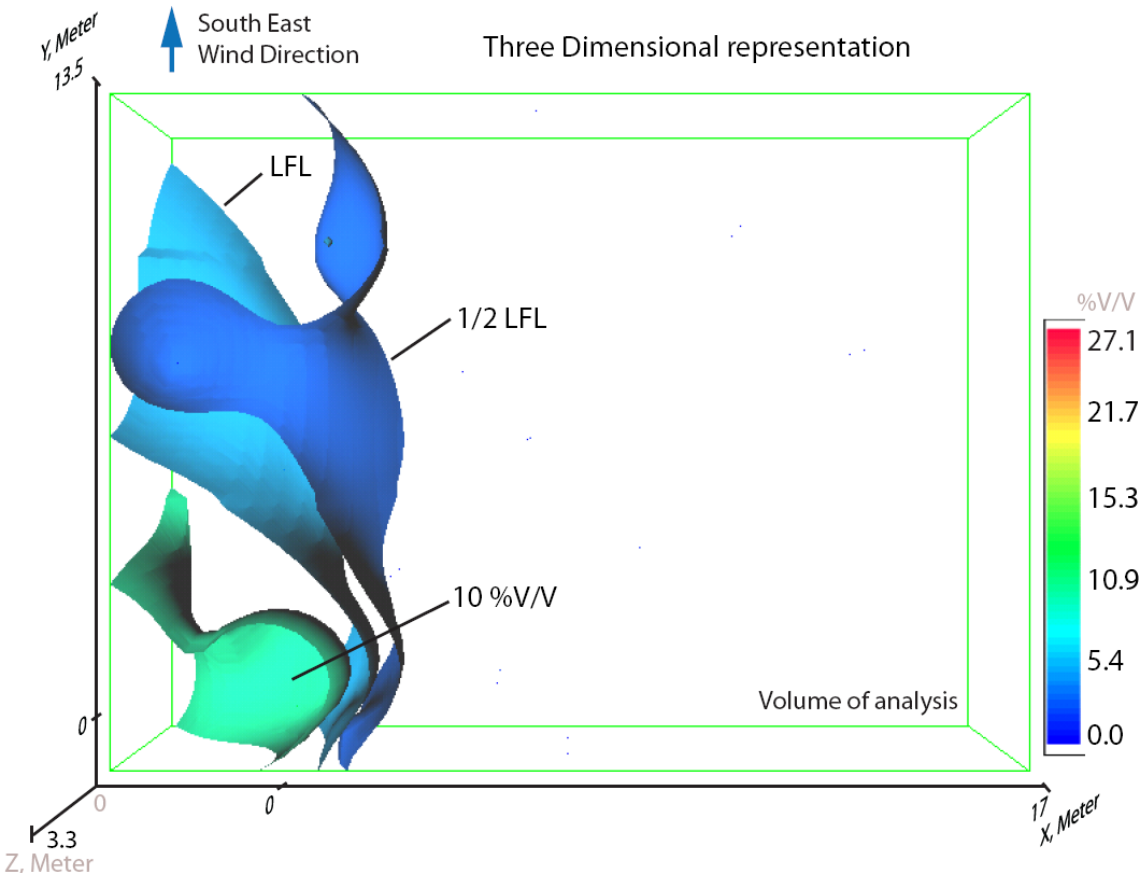

Figure 51. Three dimensional representation at 476 seconds, TEEX1

The data collected with a S wind is shown in Figure 52 and Figure 53, respectively, as two- and three-dimensional representation during TEEX2. The concentrations ranged from 0 to 16 %v/v and the downwind distance was estimated at 15.9 meters from the release point. The shape of the cloud was influenced by the corner/edge of the pit. The S wind approached the corner of the pit and the hydrocarbon vapors were entrained from the corner of the pit to the downwind area. The geometry of the wall and the wind direction influenced the formation of the plume into a cloud with two trails, illustrated in Figure 52. The wind velocity was recorded at 6.8 m/s at 737 seconds.

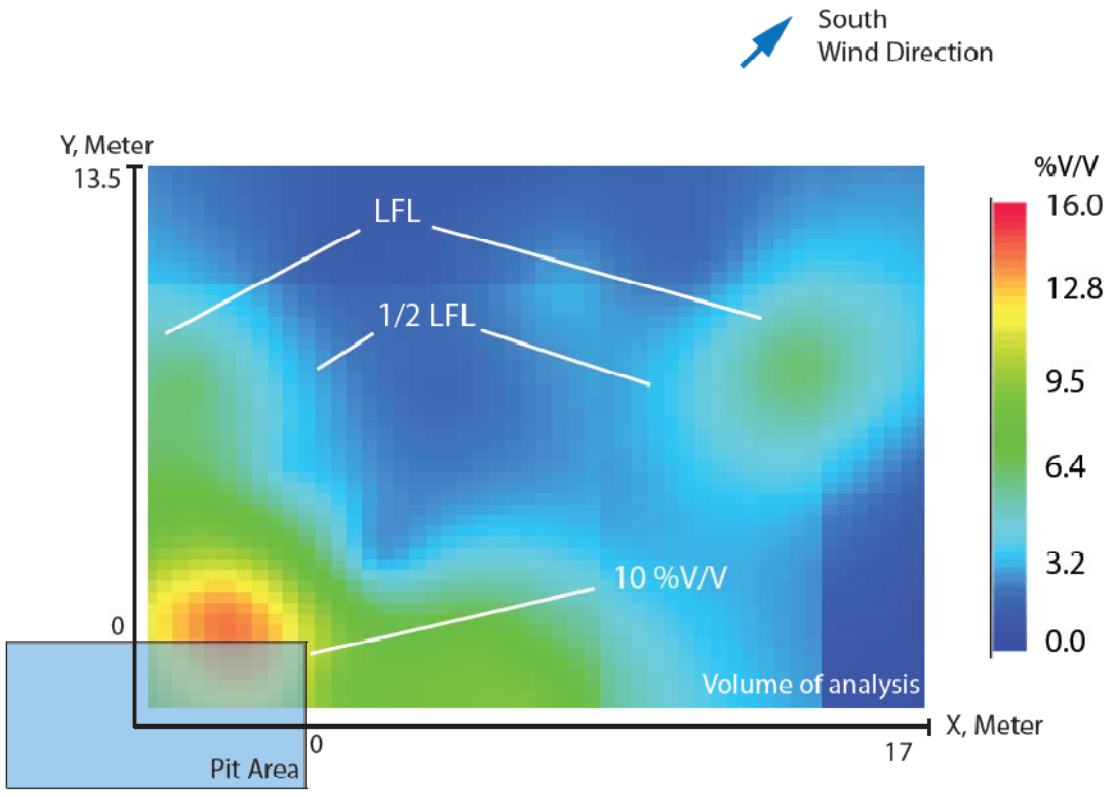

Figure 52. Two dimensional representation at ground level at 737 seconds, TEEX2

The edge of the pit is illustrated by the reference point (0, 0). Several times, the data showed pockets of hydrocarbon concentration leaving the main cloud. This phenomenon may be linked

to the change of wind directions. Figure 53 shows the three-dimensional geometric of the pocket. Two sensors recorded the hydrocarbon concentration at this location. One was above 2.5% v/v and the other one was above 5 %v/v. The three-dimensional representations illustrate the behavior of the cloud as it was traveling downwind. The isosurfaces show the gas falling down, which is one characteristics of dense gas behavior.

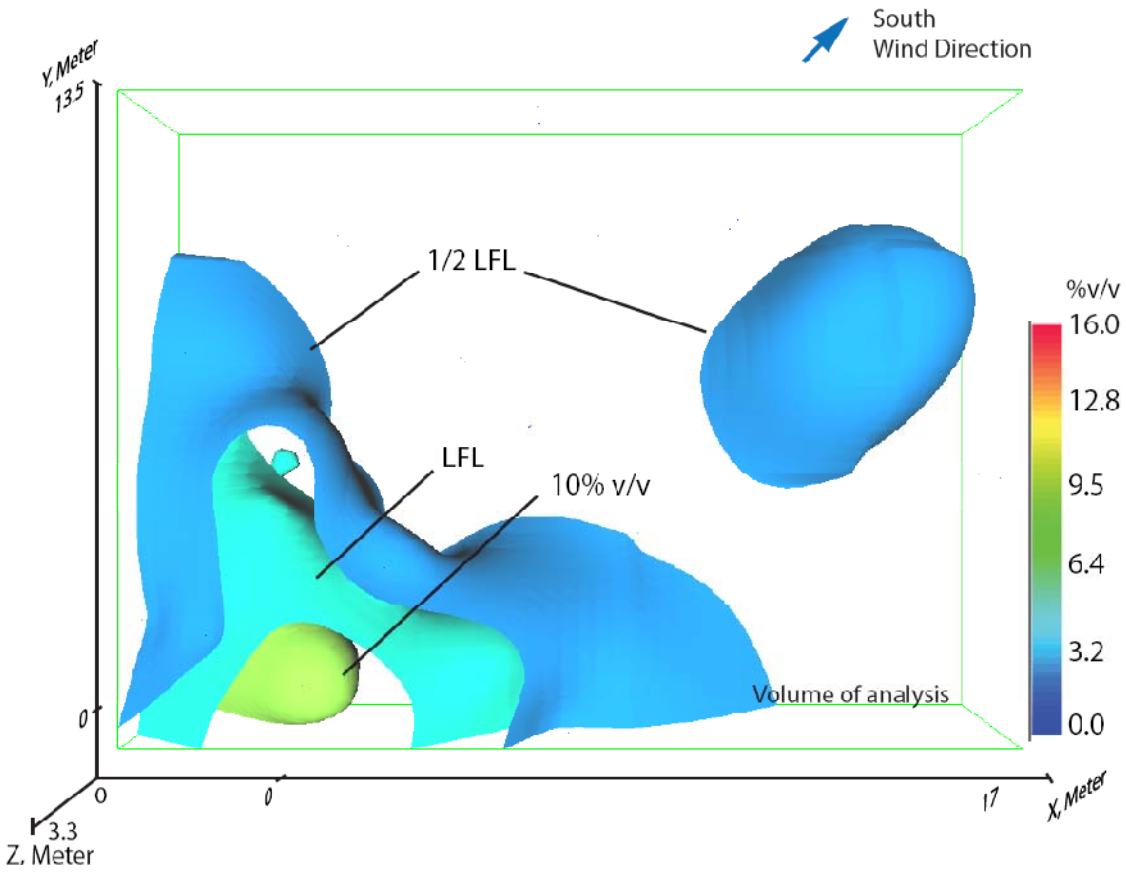

Figure 53. Three dimensional representation at 737seconds, TEEX2

3.2.3.4.4 LFL distance

The LFL distance was estimated using the three-dimensional representation based on average concentration from every 10 seconds. The maximum downwind distance for the array was 21.7 meters for S wind and 13.5 meters for SE wind. The half LFL were not presented because most

of the time, this concentration were outside of the array. The LFL distance is reported in Figure 54. The LNG release starting and ending time is shown on the figure. The wind direction is also indicated to illustrate the behavior of the curve. For TEEX1, the LFL distance was estimated at 11 meters with a SE wind and 15 meters with a S wind. The Figure 41 showed that the pool was not fully formed yet during the SE wind period. Thereby the LFL distance did not reach a steady value between 200 and 350 seconds. On the other hand, TEEX1 seem to have reached a steady value for the LFL distance with a S wind direction.

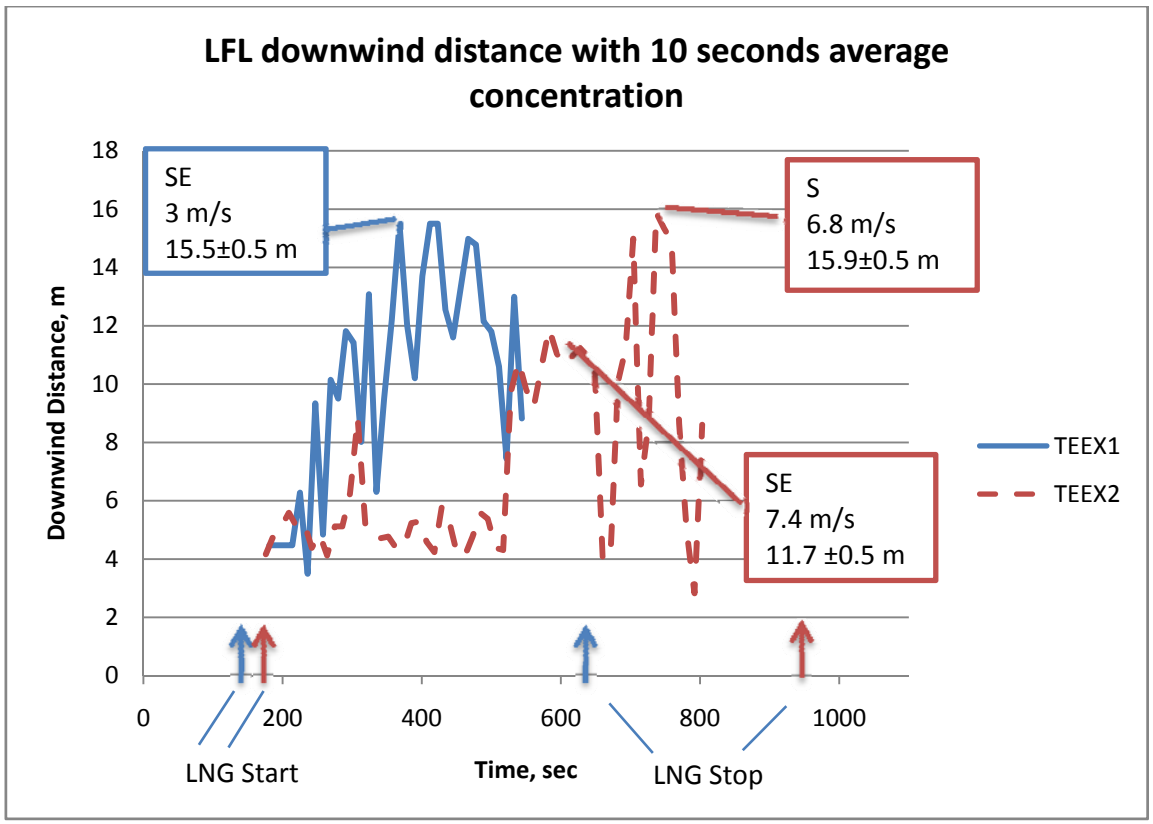

Figure 54. LFL distance estimated from the data collected during TEEX1 and TEEX2

For TEEX2, The wind direction is also shown at the bottom of the curve. During an E wind, the centerline of the cloud was outside the array, therefore the LFL distance were small and not

conclusive. For a SE wind, the distance was also approximately in the same range from 10 to 12 meters. Then finally, for a S wind, the LFL distance almost reached 16 meters.

3.2.3.4.5 2.5 % v/v illustration

NFPA 59A recommends the use of half LFL distance in the estimation of the exclusion zones instead of LFL distance to account for the formation of flammable pockets. Several times during the data analysis, it was noticed that pockets of hydrocarbon vapors were separated from the main cloud. Figure 55 shows a three-dimensional representation at time of 528 second during TEEX2. This pocket occurred when the wind shifted from E to S. The pocket has concentration of hydrocarbon vapors higher than 5 % v/v. Current models may not account for the formation of this flammable pocket of methane. On the other hand, half LFL is covered in this pocket. The conservative approach will be to estimate the half LFL distance to take pockets formation into account.

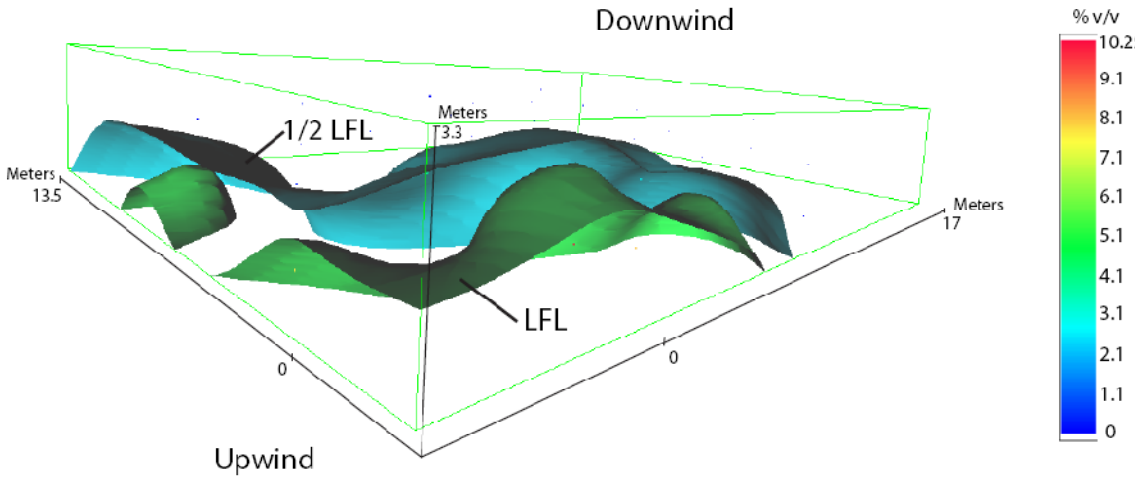

Figure 55. Half LFL illustration

3.2.4 Conclusions

The two tests presented in this paper were performed on the same day at the BFTF in November 2007. Two tests had different conditions. TEEX1 had low wind velocity with a

stability class B. The wind direction shifted from SE to S during the test. TEEX2 had a medium to high wind velocity with a stability class C. The wind had a large wind shift from E to S. LNG was continuously released for at least 10 minutes in each test. The flow rates were different due to the gravity and the pressure inside the LNG tanker, which are difficult to control. The quantity of cryogenic liquid released onto the water was also different, because the pipeline was not pre-cooled at the beginning and TEEX2 had a lower flow rate by 16 % compared to TEEX1.

The wind field, temperature and gas concentration were analyzed in this paper through two- and three-dimensional contours. For TEEX1 and most of TEEX2, the centerline of the hydrocarbon cloud was located within the array of sensors. Most of the features of the cloud were captured in the data presented in this analysis. The LFL concentration was in array of sensors, but the half LFL concentration extended beyond the array of sensors. This test was setup to characterize the source term of the release. The data also enhanced the need to use half LFL in the estimation of the exclusion zones with any models because of the formation of flammable pockets.

The pool size and shape was estimated by using the thermocouple measurements at the water surface. The area of the LNG pool was interpreted using the contour based on temperature interpolation. Knowing the flow rate and the pool size, the mean mass evaporation rate was estimated. To reduce the uncertainties, the mass evaporation (or heat flux) was measured also from the temperature of the water. The analysis of the temperature of the water showed the different mass evaporation rates at different locations. High evaporation rates may be linked to the turbulence associated with liquid phase velocity, the interaction between the bottom of the LNG layer and the water surface and the amount of LNG at that particular point (interact with water). Low evaporation rates are located around the edge of the pool or locations away from the path of the liquid velocity. The hydrocarbon vapors were observed to be turbulent inside the pit and the hydrocarbon vapors are entrained by the wind.

The concentration based on temperature inside the pit showed an accumulation of the high concentration located above the pool formed. The concentrated hydrocarbon vapors covered only part of the available space. High mass evaporation created a high gas phase velocity which

may result in pushing higher concentration upward. The liquid phase velocity influenced the location and shape of the cloud inside the pit, before the cloud was entrained by the wind. The downwind plume has different shape depending on the wind direction. For SE wind, the shape of the plume is typical, the width and the length depend on the wind velocity and LNG flow rate. For E or S wind, the shape is influenced by the geometry of the wall. Indeed, the shape has two ends and it is wider. The length seems to be reduced according to the LFL distance records. Pockets of flammable vapors were also formed leaving the main cloud. Half LFL may account for this phenomenon. This phenomenon seems to occur at the change of wind direction. During the test performed at BFTF, it was obvious that the evaporation phenomenon had significant effect on the vapor generated inside the fence, which affected the downwind concentration vapor cloud. Most of the consequence modeling software use a mean mass evaporation rate as their source term and they do not include turbulence parameters for the source, which may not be significant effects for large wind velocity.

The data collected during November 2007 showed a coherent transition from the water temperature, to the mass evaporation rate at water surface, to the concentration profile inside the pit. Even if the concentration inside the pit was based on the temperature, the data still correlated to the concentration downwind.

CHAPTER IV

CFD FOR LNG VAPOR DISPERSION MODELING*

CFD modeling was performed using CFX, which a commercial CFD code for general purpose. This section demonstrates the capabilities of CFD codes once it is tuned against experimental data collected during November 2007 tests.

This chapter is divided into three main section, parameter effect on vapor dispersion, numerical simulation and sensitivity analysis. In the first section, each parameter describes in chapter II, is reported here and also a short description of its understood effect on vapor dispersion. The second section, numerical simulation, shows the calibration of the CFD codes using the data collected during November 2007 for the release on water and on concrete. The last section presents a sensitivity analysis on selected parameters.

4.1 Parameters effect on vapor dispersion

Part of this chapter is to identify not only the key parameters but also estimate the effect of the parameters on the vapor dispersion. As presented in the previous section, the three sets of parameters are regrouped into models to represent the boundary conditions of the domain. Each parameter has an effect on either the cloud concentration, length or shape. To understand or better yet to control hazard of flammable vapor cloud, it is essential to know what are the effects of the parameter on the vapor cloud. It may be possible to control some of these parameters to diminish the hazard effect through design. Table 16 regroups the parameters discussed in the previous section with their effects on the vapor dispersion if known.

---

*Part of this chapter is reprinted from *Journal of Loss Prevention in Process Industries*, Benjamin Cormier, Geunwoong Yun, Ruifeng Qi, Yingchun Zhang and M. Sam Mannan, Computational fluid dynamics for LNG vapor dispersion modeling: A key parameters study, Copyright (2008) with permission from Elsevier.

Table 16. Effects of parameter on the vapor dispersion

Parameters	*Properties/range/estimation*	*Unknown or known effects*
Release rate	Quantity	Relatively known, increase the size of the cloud as the rate increase
Pool shape	Rectangular, circular	Unknown
Mass evaporation rate	0.029 to 0.185 kg/m^2 s (Luketa-Hanlin, et al., 2007) recommended mean values	Unknown, effects from low or high mean values Unknown effects of mass evaporation rate profile inside of a mean value
Pool area	Estimated from the mass evaporation rate, pool shape, and release rate	Unknown
Turbulence factor due to the release scenario	Referred as turbulence factor, from 1 to 10 (Hissong, 2007)	Unknown
Turbulence intensity due to evaporation phenomena	1 to 10% (Luketa-Hanlin, et al., 2007)	Unknown
Sensible heat flux from surrounding	In the range of hundreds positive or negative	Known, thermal effect to the cloud: Negative sensible heat flux increases the downwind distance by limiting the vertical mixing rate. Positive increases the vertical mixing rate inside the cloud, which reduce the downwind distance
Wind velocity	Atmospheric boundary layer, wind profile respect to height	Known for large wind velocity Unknown for low wind velocity
Temperature ambient	Temperature profile respect to height	Forced thermal mixing with cold LNG vapor Reduction of downwind distance
Surface roughness	Values known (Panofsky & Dutton, 1984)	Known effects for homogeneous roughness terrain (Peterson, 1990)
Obstacles	i.e. passive barrier	Unknown
Wind direction	Obstacles related	Unknown

4.2 Numerical simulation

The numerical simulation was divided into two types of release, on water and on concrete. Both cases were performed during November 2007 at the BFTF. The data collected was used to calibrate the model with respect to a set of conditions, and then a sensitivity analysis were performed on selected parameters. The tests carried out were designed with two objectives, (i) refine the source term (ii) collecting data with obstacles to compare with CFD modeling. Thereby gas and temperature measurements were collected outside and inside the release area. A vapor fence was used around the release area to create the obstacles effect. For the

release onto water, thermocouples were placed underneath of the water to capture the heat transfer to the water.

4.2.1 Release on water with vapor fence

4.2.1.1 Site description and domain definition

The larger pit at the BFTF was filled with 1.3 meters of water and a 1.3 meters vapor fence was installed at the edge of the water, shown in Figure 37. Two foam generators were installed at 1.3 meters above the ground apply high expansion foam (500:1). Foam generators were not utilized during this test but they were a mean of mitigation if necessary. LNG was released on water with the mean of a ramp to ease the vertical velocity, but the horizontal fluid velocity was conserved. The main obstacles of the site were identified as the vapor fence and the foam generators and thereby they were modeled in the domain.

Gas sensors were placed in the downwind direction of the release area. The gas poles are noticeable in the Figure 37 in the back of the release area (white and orange bands). The strip on the pole may be used as a scale, each strip was 0.3 meter. A large domain was developed to enclose the sensors and also to avoid undesirable effects from the boundary conditions on the vapor dispersion. Based on Cartesian coordinates (x, y, z), the size of the domain was a rectangular parallelepiped from (-66, -56, 0) to (55, 88, 15) meters with a reference point (0, 0, 0), shown in Figure 56. Positive y-axis and positive x-axis represented SE and SW direction respectively. Positive z-axis was the height of the site with zero being at the ground level.

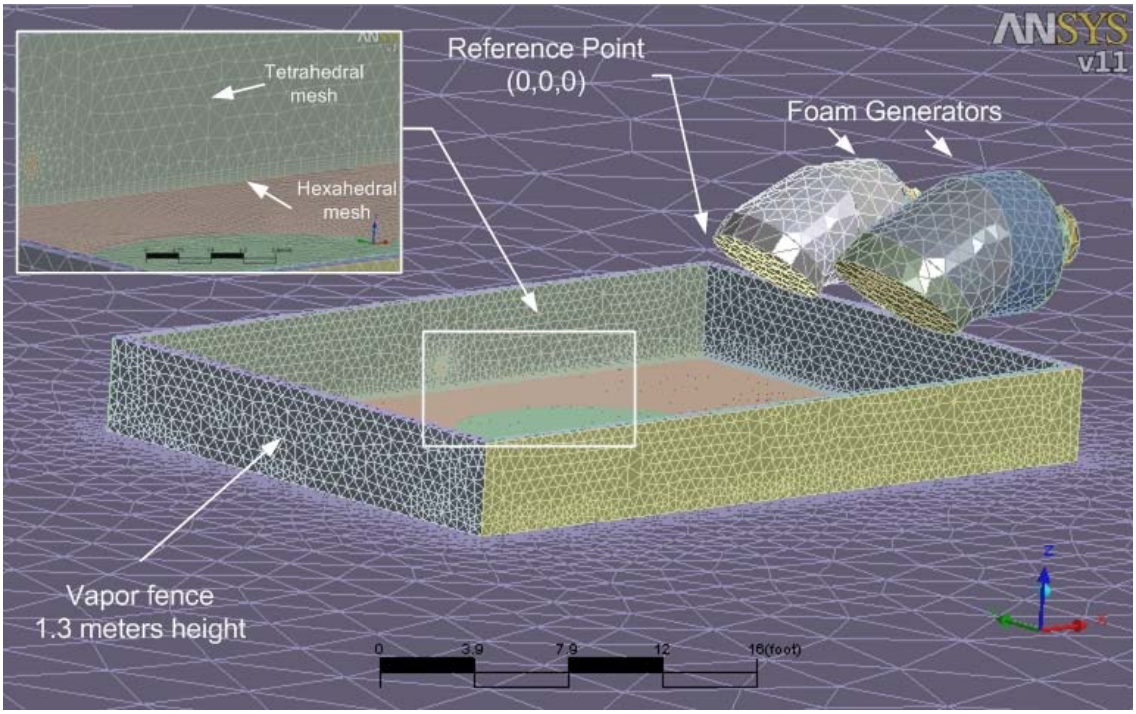

Figure 56. Mesh details and obstacles

Wall boundary conditions were used to simulate the vapor fence, the water surface not covered by LNG, foam generators and concrete ground. The mesh was refined up to 0.024 meter in the area where high gradient were expected (i.e. at the source term). The refinement was high at the source term (i.e. inside the fence), and at the water area, but mild around the foam generators and the vapor fence. A hexahedral mesh was used as an inflation layer above the source term and then a tetrahedral mesh for the rest of the domain, as shown in Figure 56. The foam generators were also included in this refinement procedure due to the circular geometry and their location above the source term. The ground of the domain had a minor refinement to enhance the buoyant effect in the cloud. Several mesh refinements were performed to find the number of elements necessary to obtain an independent grid solution. The optimal meshes was defined to be 730,000 elements for the release on water and the grid independent test is shown in Figure 57. The wind velocity with respect to z axis was used as gird independent test. The values between 730,000 and 1,500,000 elements did not change significantly, therefore a mesh with 730,000 elements was used to reduce the computing time.

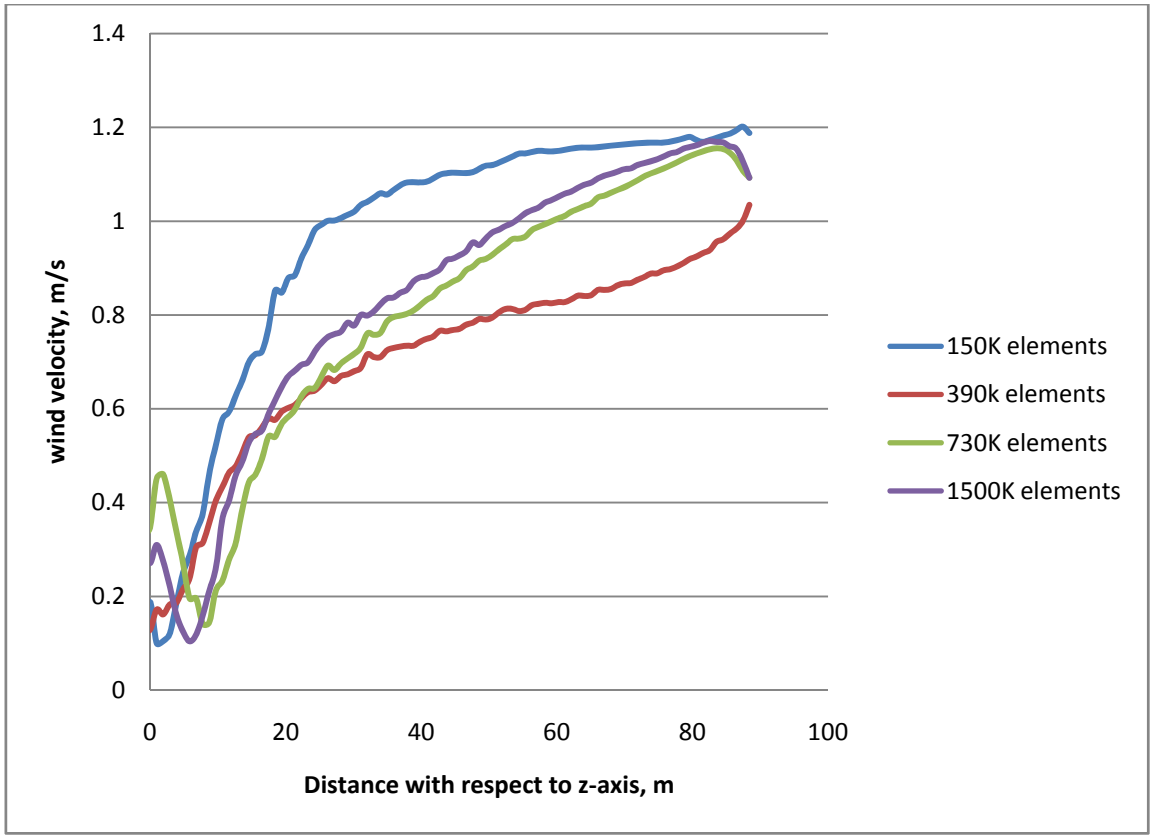

Figure 57. Grid independent test

4.2.1.2 Boundary conditions setup

The boundary conditions setup was based on the data collected during the test. The release onto water test was performed twice at different weather conditions. The characteristics of the tests are presented in Table 13.

The atmospheric boundary condition was set to opening boundary condition. By using Cartesians frame, the wind direction was defined, SE and S were set to 90 and 45 degree as y- and x-axis, respectively. The wind and temperature profile was developed using the Equations (25-26) as a function of the Monin-Obukhov length. The friction velocity, roughness and potential temperature were the only inputs to this model. Other variables presented in Table 13, Monin-Obukhov length, Richardson number, heat and momentum diffusivity, were used to verify the accuracy of the wind profile using the Equations (34, 37-29). The turbulence for the

atmospheric boundary condition was set through the k-ε two-equations turbulence model, where k and followed the Equations (17-18) also related to the Monin-Obukhov length.

The values presented in Table 13 only gave a general description of the conditions for the overall tests. During the TEEX1, the wind velocity at 2.3 meters varied from 1 m/s to 3 m/s and the wind direction varied from SE to S. For a fair comparison with the collected data, the wind velocity and direction were set according to the particular time and then compared. For different wind profile, the friction velocity was adjusted which governed the rest of the variables respect to the time selected.

The source term was defined as inlet boundary condition in the domain. The source term is composed of four elements, geometry, area, gas phase velocity profile, turbulence and location. The test was designed to create a free-obstacle pool formation (i.e. no interaction with the boundary of the pit). Therefore the pool may assume to be a circle. The gas phase velocity profile was derived from the mass evaporation rate data collected, shown in Figure 43 and Figure 44.

This contour was obtained by Kriging interpolation from twelve measured points (dots in the figure). The figure represents the vertical heat transfer through the water located 45 cm underneath of the LNG pool. The mass evaporation rate was found in a range between 0.1 and 1 kg/m^2 s. The pool area was optimized estimated three conditions, (i) flow rate on liquid mass rate of the discharge hose (5.2 kg/s with liquid density of 425 kg/m^3), (ii) mean value of mass evaporation (also estimated from 0.15 to 0.18 kg/m^2 s) and (iii) the mass evaporation rate profile (Figure 43 and Figure 44). Due to uncertainties associated with the data collected and the interpolation methodology used, several iterations of the following method were needed to find the optimal area:

1. The initial area was estimated using the mean mass evaporation rate and the liquid mass rate of the discharge hose.
2. The total liquid evaporation rate was estimated by integrating the mass evaporation profile over the initial area (from step 1)

3. If the integrated mass evaporated was equal to the liquid mass rate of the discharge hose, LNG pool area was optimized. If the integrated mass evaporated was too large, the area of the pool may be reduced and if the integrated mass evaporated was too small compared to liquid discharge hose, and then the pool area was increased.

For TEEX1 and TEEX2, the optimal pool area was found to be 15 and 13 m^2 with the mass evaporation profile. By using the methane gas density, the velocity profile was derived and integrated into the boundary condition. Two other pool geometries were used during this study, circular and rectangular.

A 3-inch diameter pipe was used to release LNG onto water. The horizontal fluid velocity of the discharge hose created turbulence inside the vapor fence. This turbulence was simulated by increasing in the values of turbulence intensity or by incorporating an inlet jet representation the effect of the fluid velocity. A inlet velocity of 4.3 m/s was added to simulate for the steady state fluid velocity (no vapor formation out of the discharge hose).

The ground was set as a wall boundary. Wall boundary is like a solid (impermeable) boundary to fluid flow. It does not let any flow going through but the heat input is allowed. For this model, the ground was set with a surface roughness and sensible heat flux corresponding to the sensible heat flux reported in the Table 13 and using Equation (36). The water surface was set to wall boundary conditions with a measured temperature of 293 K and a surface roughness for water at $4x10^{-4}$ m from the literature (Panofsky & Dutton, 1984). The vapor fence and foam generators were set with a smooth surface and an adiabatic heat source rather than a surface roughness or/and a material temperature.

4.2.1.3 Simulation results

The data collected during November 2007 test provided information to help in the evaluation of the visible behavior/features of cloud. The visual data as well as sensor data were useful in the verification of the output from the simulation results. Figure 58 shows the side view of the release area with two types of camera at the same time frame. The normal camera showed the white condensate cloud, which represents only the condensate moisture in the air due to the cryogenic temperature of LNG vapor. The infrared hydrocarbon camera showed the carbon

molecules, which is commonly used today to detect leaks in hydrocarbon industry. Several detail information are available on this picture, such as the height of the white condensate cloud and the angle of the cloud traveling at the edge of the barrier.

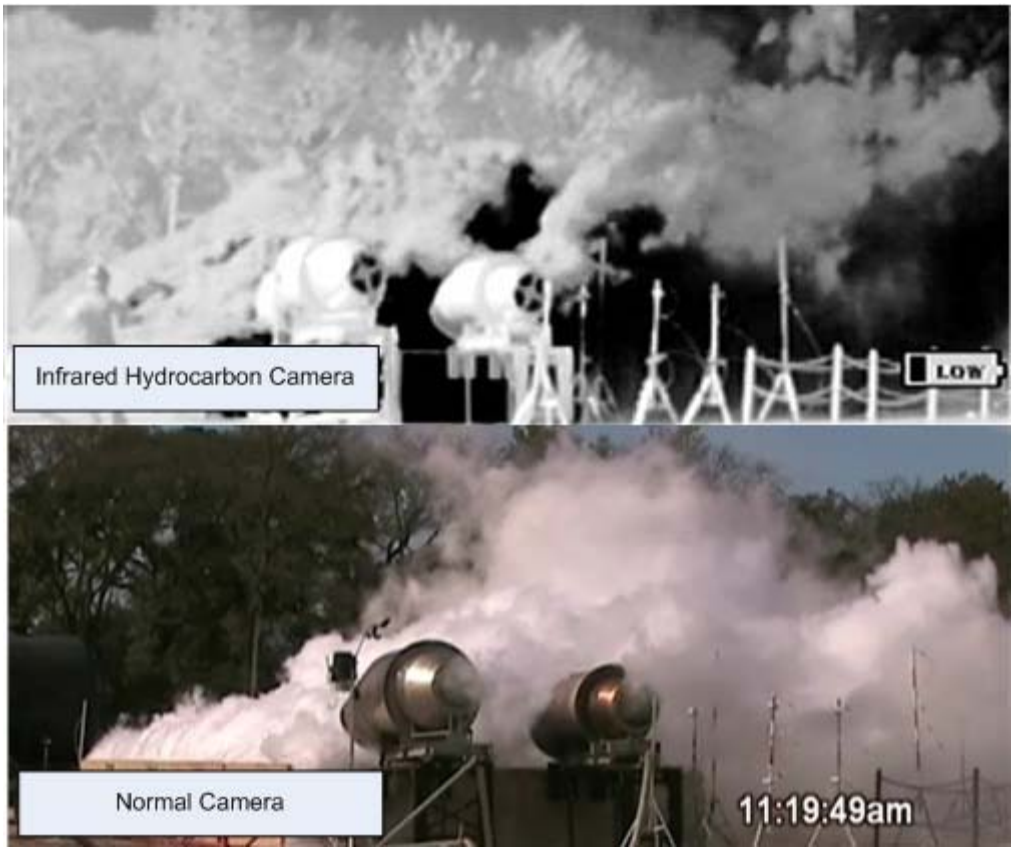

Figure 58. Video pictures of release on water, infrared hydrocarbon camera (top) and normal camera (bottom), TEEX1

In the infrared hydrocarbon camera, the black represents the cold temperature and the carbon molecules; the white represents the warm temperature. Infrared reflections from the sun and the background reflected on the cloud created noise in the capture of the video (increase of white area).

TEEX1 and TEEX2 release on water presented interesting features during the generation of the vapors. High gas phase velocity was noted leaving the release area during the tests indicated a

high turbulence inside the vapor fence. High evaporation of LNG and fluid velocity combined with low wind velocity created a large vapor cloud above the release area (concept illustrated in Figure 10).

To be able to do the data analysis using CFD code, cases were defined and then simulated as a continuous simulation. Continuous simulations represent the steady state for a set of parameters. For TEEX1, the wind velocity was set to 3 m/s at 2.3 meters and wind direction as SE. TEEX2, the wind velocity was set to 7.4 and 6.8 m/s with a wind direction to SE and S respectively, shown in Figure 54.

4.2.1.3.1 TEEX1 simulation results

The friction velocity was modified to accommodate the wind velocity of 3 m/s, but the other parameters were kept the same as shown in Table 13. The gas phase velocity profile was developed following the three steps presented previously to optimize the LNG pool area. Two LNG pool geometries pool were also tested. The LFL was used as monitoring value for the downwind distance at 0.5 meters high (in the z-axis) and at the discharge hose location (with -4.5 meters value in the x-axis) for each run and reported in Table 17.

Table 17. TEEX1 simulation summary for a wind velocity of 3 m/s

Run	*LNG pool geometry shape*	*Turbulence intensity from equation with Eq. (23), %*	*LFL distance SE (-4.5, y, 0.5), m*
TEEX1_1	Rectangular	1	20
TEEX1_2	Rectangular	10	18
TEEX1_3	Rectangular	100	20
TEEX1_4	Rectangular	1,000	21
TEEX1_5	Circular	1	15
TEEX1_6	Circular	10	16
TEEX1_7	Circular	100	15
TEEX1_8	Circular	1,000	16

Several runs were necessary to tune the parameters used in the model. The turbulence intensity and the LNG pool geometry were varied because it was not directly measured during the test. The turbulence intensity had a small effect on the LFL distance but the LNG pool

geometry had a greater effect. The rectangular LNG pool geometry gave higher LFL distance compare to the circular pool geometry. The collected data for November 2007 showed a LFL downwind distance of 15.5 ± 0.5 meters (average value over 10 seconds) for at wind velocity at 3 m/s. The simulation results with a circular LNG pool geometry seem to be on agreement with the collected data. Figure 59 shows the comparison of concentration profile between the simulation results and the data collected during November 2007's tests.

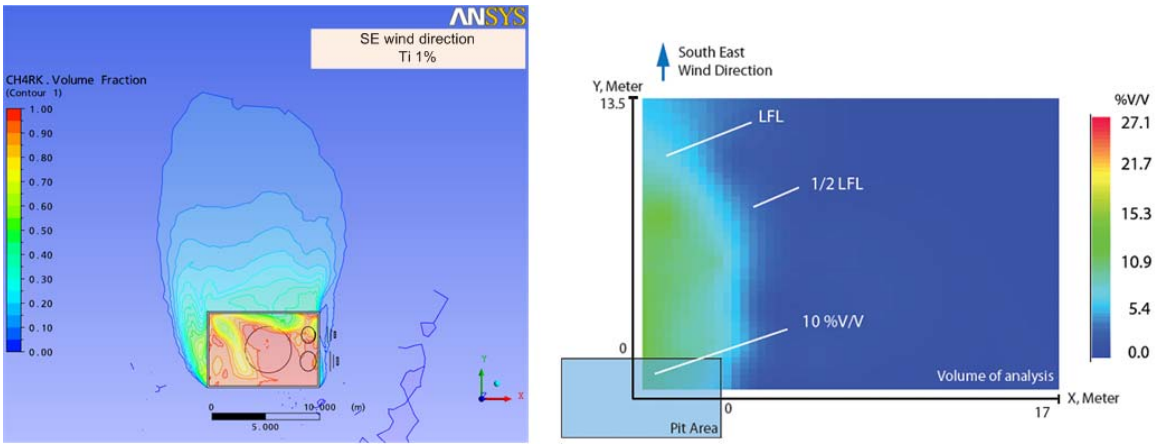

Figure 59. Comparison of concentration profiles at 0.5 meter above the ground level, simulation (left) and collected data (right), TEEX1

The gas sensors were installed for vapor cloud with its centerline in the S direction. As the test proceeded, the wind shifted letting only half cloud within the array of sensors, presented in the right side of Figure 59. For the same location, the highest concentration measured was 27 % v/v during the test, and the simulation showed a concentration level reaching 35 % v/v.

4.2.1.3.2 TEEX2 simulation results

The model was also tested against the data collected for TEEX2. The friction velocity was set to 0.383 and 0.353 m/s for a wind velocity of 7.4 and 6.8 m/s at 2.3 meters above the ground. The potential temperature was kept the same as the value reported in Table 13. The gas phase profile was developed using the same procedure as shown previously. The results are presented in Table 18.

Table 18. TEEX2 simulation results for SE at 7.4 m/s and S at 6.8 m/s

Run	*Wind direction*	*Geometry pool shape*	*Turbulence intensity with Eq. (23), %*	*Wind velocity at 2.3 m, m/s*	*LFL distance SE (-4.5, y, 0.5) S ($\sqrt{x^2+y^2}$, 0.5), m*
TEEX2_1	SE	Rectangular	1	7.4	12
TEEX2_2	SE	Rectangular	10	7.4	12.5
TEEX2_3	SE	Rectangular	100	7.4	12
TEEX2_4	SE	Rectangular	1000	7.4	13
TEEX2_5	SE	Circular	10	7.4	13.5
TEEX2_6	SE	Circular	100	7.4	13.5
TEEX2_7	S	Rectangular	1	6.8	15
TEEX2_8	S	Rectangular	100	6.8	15
TEEX2_9	S	Rectangular	1000	6.8	17
TEEX2_10	S	Circular	10	6.8	17
TEEX2_11	S	Circular	100	6.8	17

The collected data showed a LFL downwind distance of 11.7 ± 0.5 and 15.9 ± 0.5 meters downwind for the high wind velocity of 7.4 m/s for SE and 6.8 m/s for S direction respectively. The numerical results showed a good agreement with the collected data again. There was a slight difference in the LFL distance using different LNG pool geometry, but less significant compared to TEEX1 at 3 m/s. The turbulence intensity did not significantly affect the LFL distance in the TEEX1 and TEEX2. Further investigation of this parameter was performed later. The plume shape is illustrated in Figure 60 for TEEX2.

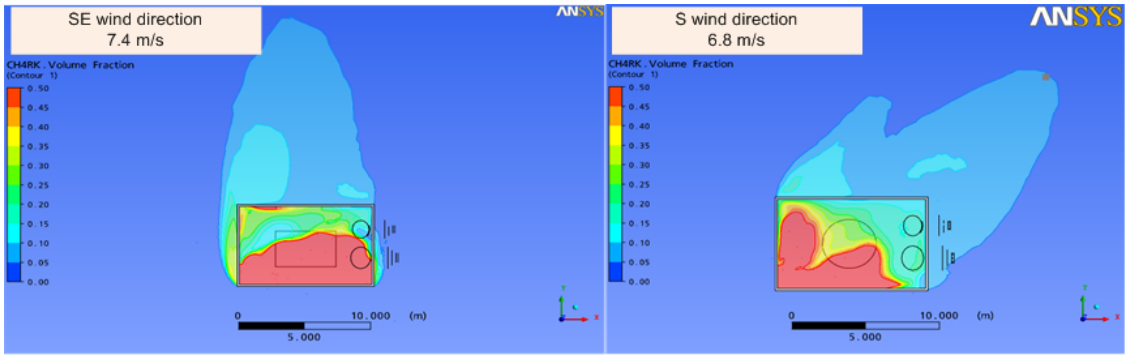

Figure 60. Concentration contour for S and SE wind direction with different turbulence intensity for TEEX2

4.2.2 Release in LNG release on concrete pit

4.2.2.1 Site description and domain definition

The release on concrete scenario, TEEX7, was to fill the pit with LNG to carry out a fire test. The larger pit at the BFTF was filled with 15 cm of LNG and a 1.3 meters vapor fence was installed around at the edge of the pit. The pit was 2.6 meters deep with a fence of 1.3 meters above the ground. Figure 61 shows the mesh definition for this test. The foam generators are the same design presented the previous section.

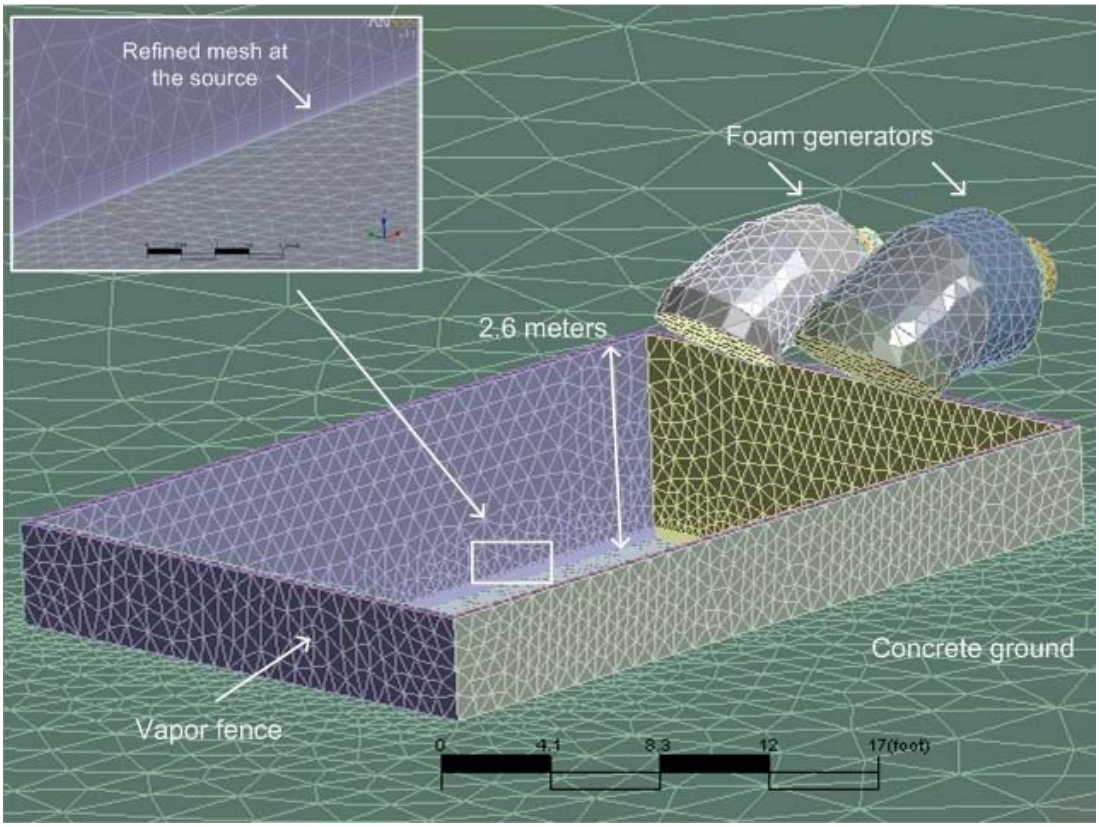

Figure 61. Concrete pit mesh definition

The grid was refined at around the pit area, inside and around the obstacles where a large gradient is expected. At the bottom of the pit, the mesh was also refined using a hexahedral mesh of 60 cm. The domain size was (-43, -35, -1.3) and (34, 60, 16) in a Cartesians

coordinates. The gird independent test was also performed and it was found that the optimal gird size was 750,000 elements.

To setup the source term, the mass evaporation rate has to be determined first. Different from LNG release on water, the heat sink in this scenario is not infinite. The estimation of the mass evaporation rate profile was calculated through theoretical analysis since the level of LNG at the bottom of the pit was not recorded during the test. The study from Briscoe and Shaw (Briscoe & Shaw, 1980) was used to estimate the mass evaporation rate. Since the study is applicable for high flow (i.e. formation of pool is instantaneous), these equations were modified to fit in this study. The heat transfer around the vaporizing liquid pool on land includes the solar radiation, long wave radiation, convection from wind, latent heat loss, and the conduction from concrete. The dominant heat transfer was from the concrete. But as the concrete started cooling due to the contact with cryogenic liquid over time, the heat flux decreased, resulting on reducing the mass evaporation rate. Once the concrete reached a steady state evaporation rate, the contribution of long wave radiation, solar radiation and convection from the wind were only less than 4%. Assuming that radiation and convection heat were ignored, the mass evaporation rate due the concrete heat transfer was given by

$$m_{cond}=\frac{k(T_A-T_B)}{\lambda(\pi\alpha t)^{1/2}} \tag{60}$$

With a low flow rate, the initial flow rate did not cool the pit enough to sustain a pool formation. The pit had to be cooled to the point that the pool will start formatting. The time when the pool starts forming is when the heat flux of the concrete is equivalent to the heat flux of the liquid discharge hose and formulated with the following:

$$t_1=\frac{1}{\pi\alpha}\left(\frac{k(T_{ground}-T_{LNG})A}{m_{LNG}\lambda}\right)^2 \tag{61}$$

$$t_2=\frac{1}{m_{LNG}\lambda}\int_0^{t_1}\frac{k(T_{ground}-T_{LNG})}{(\pi\alpha t)^{1/2}}A\,dt \tag{62}$$

where

A = the surface area of the pit

k = the thermal conductivity of the ground

α = the thermal diffusivity of the ground

m_{LNG} = the mass rate of LNG released

λ = the latent heat for LNG

T_{ground} = the temperature of the surface

T_{LNG} = the temperature of the liquid LNG

t_1 = the relative time required to equalized heat flux of the concrete to the heat flux of the mass released for a continuous release.

t_2 = the actual time to reach the equilibrium for the mass released.

Once the actual time to reach the equilibrium was calculated, the mass evaporation rate may be derived from the following:

$$m_{evap}(t)=\begin{cases} m_{LNG} & t\le t_2 \\ \dfrac{k\left(T_{ground}-T_{LNG}\right)}{\lambda\left(\pi\alpha\left(t_1+(t-t_2)\right)\right)^{1/2}}A, & t>t_2 \end{cases} \quad (63)$$

For the LNG flow rate used in this test, it requires 750 gallons per minute (gpm) (20 kg/s) to form a pool right the way. With a flow rate of 90 gpm (2.4 kg/s) and assuming 15% flashed (not contact with the concrete), it would take one hour to fill the pit up to 15 cm. The pool area used was the total surface area of the pit, 67.5 m^2.

The discharge pipe was placed almost at the bottom with a "sock" to prevent any splash. At the beginning of the release, a large cloud was noticed probably due to the cooling of the pipe. As the cryogenic liquid started building up at the bottom the pit, the visible cloud became smaller. Figure 62 shows the cloud through the normal camera and the infrared hydrocarbon camera and illustrates the size of the cloud as it came out of the vapor fence.

Figure 62. Video picture of release on concrete with normal and infrared hydrocarbon camera

At the beginning of the release, the turbulence intensity should be around its maximum and once the LNG starts building up at the bottom of the pit and reaches the steady state, the turbulence intensity should be at its minimum.

The release on concrete took one hour, while the wind velocity varied from 1 to 0.5 m/s with a constant wind direction SE. Due to low wind velocity, the wind model presented in Equation (15) was not appropriate. Thereby a simple wind profile and, power law correlation, were used (CCPS, 1999):

$$u=u_{10}\left(\frac{z}{10}\right)^{p} \tag{64}$$

where u_{10} is the wind velocity at 10 meters, p the dimensionless parameter, whose value depends upon atmospheric stability category and surface roughness (CCPS, 1999). The power law wind velocity may also be used when the wind profile is not known. With the low wind

velocity and the stable conditions, the judged atmospheric stability was estimated to be a *F* on the Pasquill-Gifford stability classes, therefore the dimensionless parameter, *P*, was set to 0.55.

Table 19. TEEX7 release on concrete parameters

Time	u_{10}, *m/s*	*T, K*	*Wind direction*	*Turbulence intensity, %*
0 to 1800	1 to 0.6	295 to 293	SE	10 to 1
1800 to 3000	0.6	293 to 292	SE	1

For a transient simulation, the gas phase velocity, the wind velocity, and the turbulence intensity were changing during the time of the test. The simulation was separated into two parts and CFX's expression editor was used, shown in Table 19. The expression editor is also linked to the variable of the simulation such as time, z, x, y coordinates. The mass evaporation rate presented in Equation (63) was setup in the expression editor, where it was converted to gas phase velocity:

$$v_g(t)=\frac{m_{evap}(t)}{A\rho_{LNG}} \tag{65}$$

where v_g is the gas phase velocity in m/s, and ρ_{LNG} is the gas density of methane at 110 K. In both cases (continuous and transient mode), the threshold value for the root-mean-square (RMS) of residuals was set equal to 10^{-4}. The RMS is a measure of the local imbalance of each conservative control volume equation and relates directly to whether the equations have been accurately solved.

4.2.2.2 Simulation results

The temperature profile of the pit was converted into a concentration profile shown in Figure 63. The concentration profile showed a layer formation from the evaporating pool at the bottom of the pit. The 15 centimeters at the bottom provided a constant and uniform gas phase velocity. The main observation was that the concentration layers inside the fence were different compared to the release on water. This indicated the absence of turbulence at the source term. Based on this observation, the turbulence intensity was set to zero and the

simulation results are presented in Figure 64. The concentration profile was on agreement with the data collected during TEEX7. The 50 % v/v layers was at the same level in both set of data.

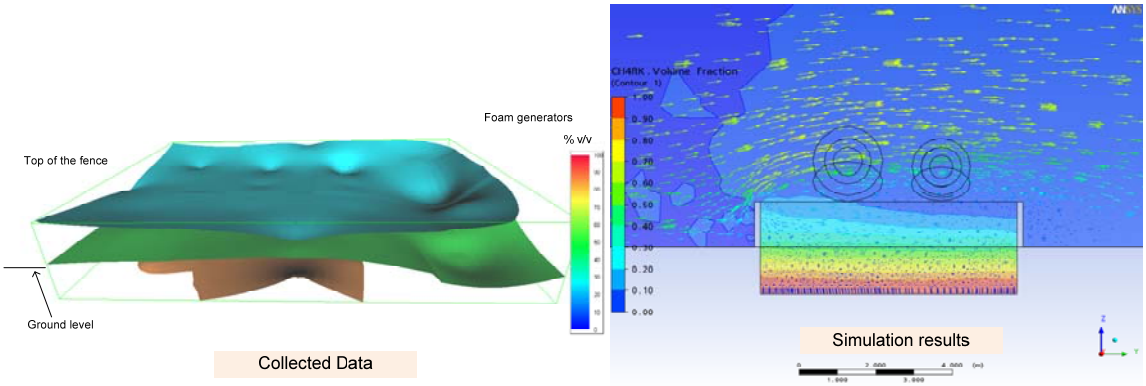

Figure 63. Concentration profile for TEEX7 inside the fence and pit. Collected data (left) and simulation results (right)

The outside visible cloud had a flat shape, illustrated in Figure 62 and Figure 64. At the edge of the fence, it was noticeable the cold LNG vapors falling down to the ground with a wind velocity near close to 0.6 m/s at 2.3 meters, which also meant that wind velocity at the ground level were even lower. This effect increased the present of white cloud around the outside fence. The simulation results, shown on the right side of Figure 64, were set to the same atmospheric conditions.

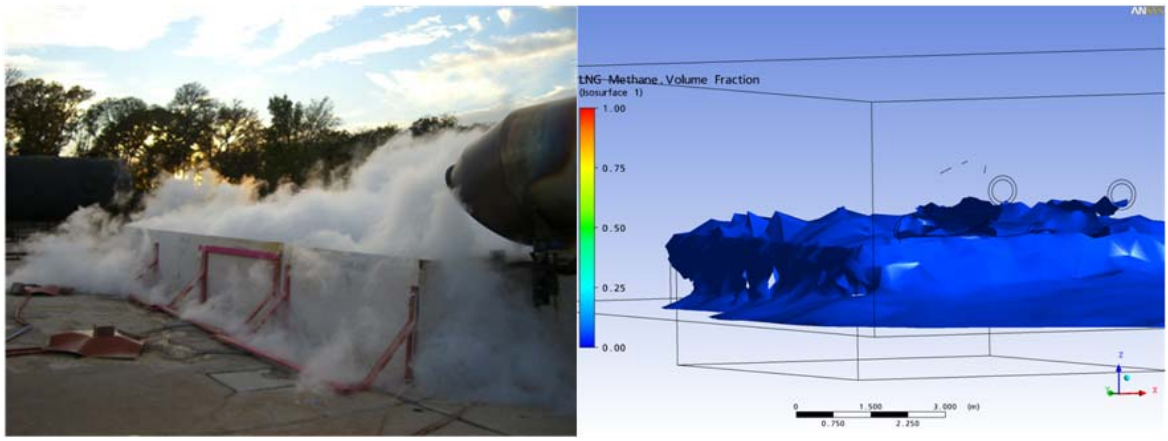

Figure 64. Illustration of the vapor falling down from the edge of the fence. Picture from TEEX7 (right) and Simulation results with no turbulence intensity (right)

The concentration data was plotted against the simulation results from the edge of the fence. The data comparison is presented in Figure 65. The preliminary results showed that the simulation was under predicting the concentration at the edge of the fence towards the end of the time. The delay in the beginning of the curve was due to the mass evaporation profile, which provide an instantaneous mass evaporation rate, but in reality, the flow rate at the liquid discharge rate at the end of the pipe was progressively increasing until the full rate was reached. More simulation work is needed to tune the model, before to perform the sensitivity analysis.

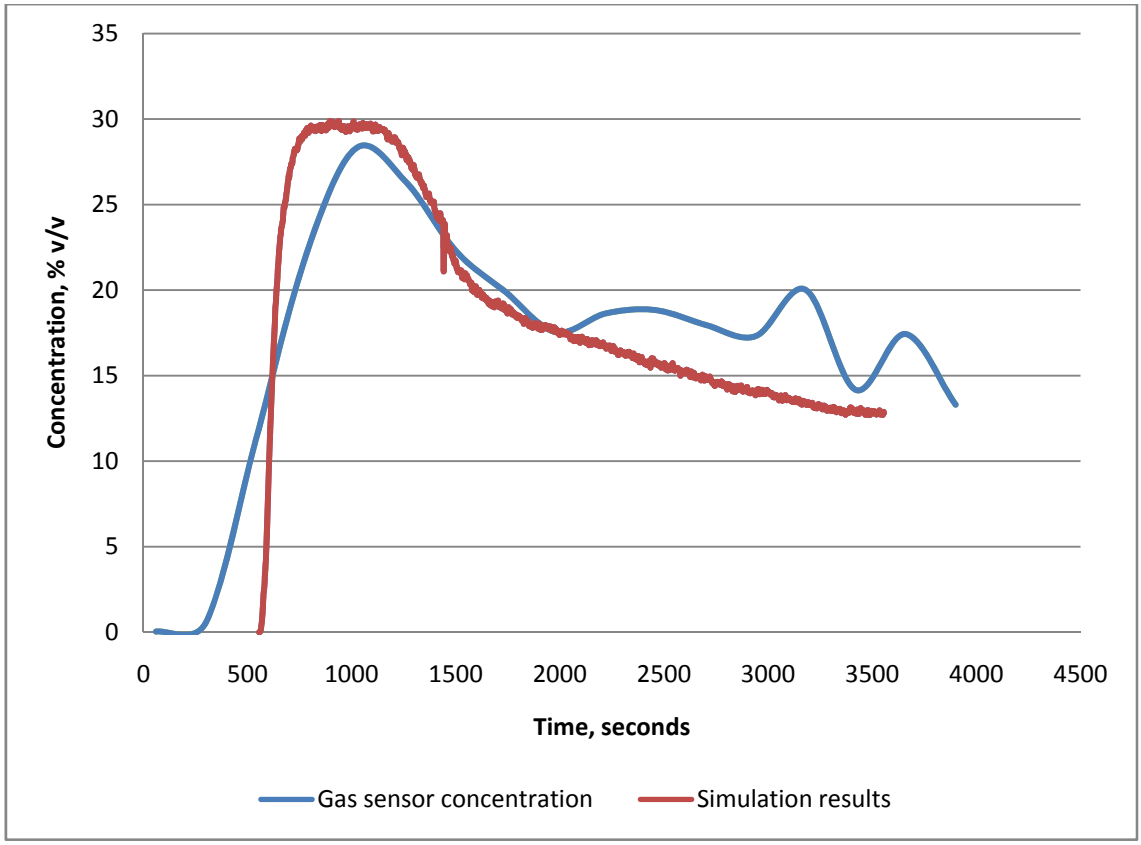

Figure 65. Concentration profile at 1.3 meters above the ground at the edge of the fence

4.3 Sensitivity analysis

4.3.1 Source term effects

Four parameters for the source term were selected and their effect on the LFL distance as well as on the concentration downwind was analyzed. The turbulence intensity at the source, gas phase velocity, pool shape and area were varied one at the time while other parameters were kept constant.

For the first series of runs, the mass released was set to 6.7 kg/s. The mass released was modified (i) to obtain a large cloud in order to increase the difference, and (ii) to obtain a point of comparison to between two mass released rates.

The friction velocity and the potential temperature were set to 0.053 m/s and 0.023 K, which corresponded to low wind velocity, around 1.2 m/s at 2.3 meters. At this condition, the vapor

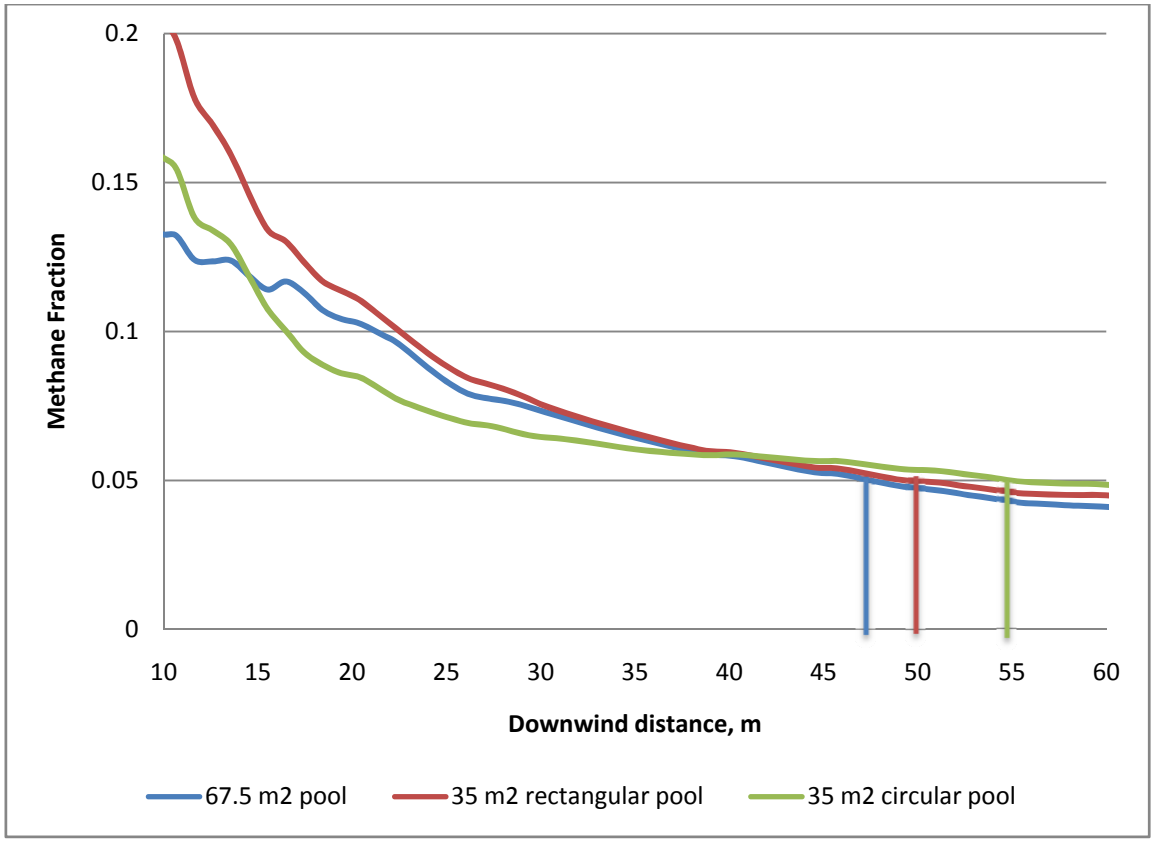

Figure 66. Downwind distance for different LNG pool geometry with *Ti* at 1% v/v

cloud behavior was gravity driven, which increased the effect of the turbulence in the vapor cloud concentration profile. The mass evaporation rate was in the recommended range, between 0.029 to 0.185 kg/m^2 s. With a maximum LNG pool possible of 67.5 m^2, i.e. total water surface area, the minimal possible mass evaporation rate was 0.1 kg/m^2 s. Then with a mass evaporation rate of 0.19 kg/m^2 s, the LNG pool area was set to 35 m^2. The geometry of the pool was also modified from a rectangular shape to a circular shape.

The different LNG pool areas and geometries were simulated using a turbulence intensity of 1%. The downwind concentrations are presented in Figure 66. The methane concentrations were measured at 0.5 meters above the ground and in the centerline of the cloud. At low turbulence, 1%, the small pool area showed a longer LFL downwind distance compared to the

large pool. The small LNG pool had a high gas phase velocity which led to an increase of LFL distance compared to the low gas phase velocity from the large LNG pool.

The LFL downwind distances agreed fairly well, within 10% deviation among them. The second set of runs was to use the same setup but with a turbulence intensity at 100%, shown in Figure 67. The LFL downwind distance for 67.5 m^2 LNG pool did not varied as much as the LFL downwind distance for 35 m^2 pool but the concentration levels were higher for the 67.5 m^2 LNG pool near of the release location. The distance difference between the three cases was larger with *Ti* at 100% than *Ti* at 1%. As the turbulence intensity increased at the source term, the effects in the downwind direction were more pronounced for low wind velocity.

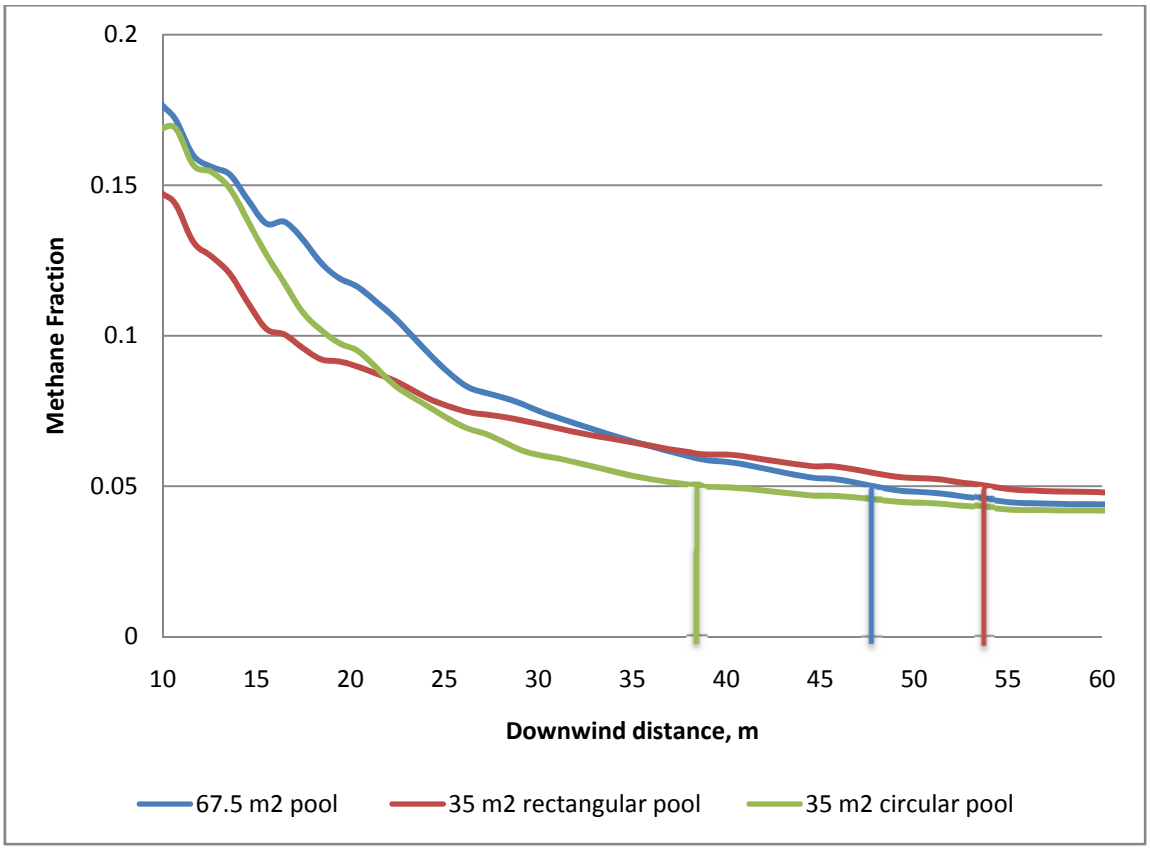

Figure 67. Downwind distance for different LNG pool geometry with *Ti* at 100% v/v

The change in the LFL distances was further analyzed by investigating the vertical concentration profile inside the fence. Figure 68 shows the methane fraction profile for 67.5 m^2 pool, where the turbulence intensity was set to 1 and 100%.

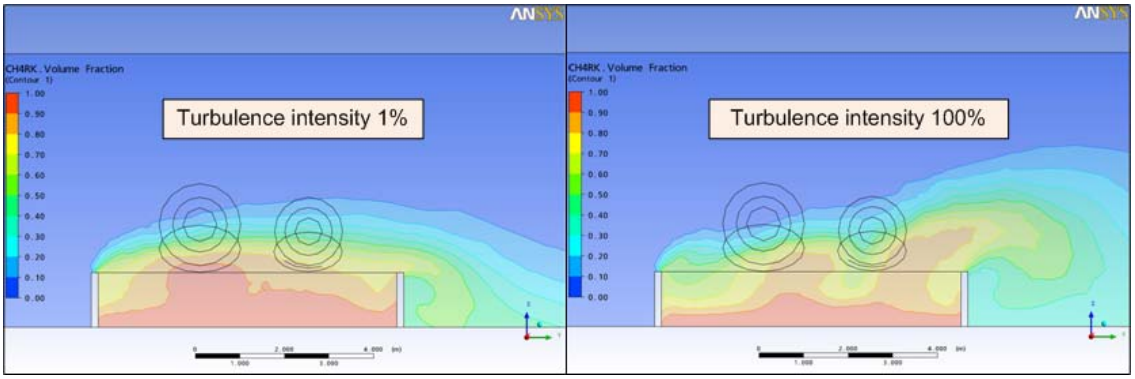

Figure 68. Methane fraction for 67.5 m^2 LNG pool, turbulence intensity 1% and 100%

The reduction of LFL distance may be explained through the height of the cloud created by the turbulence at the source. High turbulence intensity increased the upward movement of the cloud, and part of cloud was mixing with air instead of increase the level concentration at 0.5 meters above the ground level. The shape and height of the cloud with turbulence intensity of 100 % seem to match the Figure 58. The gas sensors also indicated higher concentration level at 1.3 meters than at 0.5 meters. Higher concentrations were pushed upward and outside of the fence instead of falling down to the ground level due to the high turbulence. For the first 25 meters at the downwind direction, the concentration levels of 1% were lower than that of for 100%, illustrated in Figure 66 and Figure 67. The concentration level near the source was higher due to the turbulence intensity.

The left of the Figure 69 shows the velocity profile above the source for a 67.5 and 35 m^2 pool with a turbulence intensity of 1%. The velocity profile near the source term revealed the formation of eddies. Each eddy was marked with a number to identify its location. For the 67.5 m^2 LNG pool, eddies only formed near of the top of the fence, illustrated in Figure 69, which resulted in disturbing only the top part of the concentration levels shown in Figure 68.

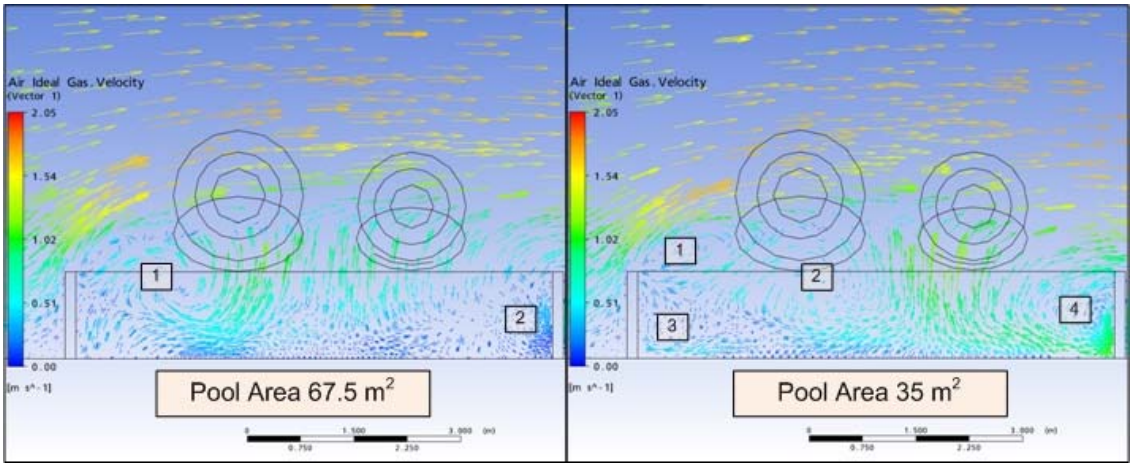

Figure 69. Velocity profile above the source term for a 67.5 (left) and 35 (right) m^2 LNG pool with *Ti* at 1%

In other hand, the velocity profile for 35 m^2 circular LNG pool is shown on the right side of Figure 69. Several eddies (up to four in the vertical plan) were noticeable from the analysis of the simulation results. The eddies increased the mixing effects of the methane vapors with air before the vapors were entrained downwind by air. The difference in the number eddies formed inside the fence was related to the size of the LNG pool. The 67.5 m^2 LNG pool did not have enough room for the eddies to form at the water surface level. This explained the change of concentration level in the downwind direction.

Either with low or high turbulence intensity, it was noticeable that the concentration levels were forming uniformly above the water surface for a 67.5 m^2 LNG pool. This effect was due to the uniform mass evaporation rate used, which created a plug flow effect as the vapors were raising inside the fence. The turbulence intensity changed only after the upper part of the concentration profile in the pit. During the TEEX1, the temperature profile of the pit was measured at 36 locations. Figure 45 shows the concentration estimated from these temperature measurements to provide an idea of the cloud shape inside the fence. The shape of the Figure 45 did not match the shape of the Figure 68. This data indicated that the LNG pool was not covering the entire water surface area. Several eddies and large air pockets inside the fence were noticeable on the video from the test, which confirmed the shape of the pool and the eddies formation observed in the analysis of the simulation.

The three scenarios were modeled against the data collected, the turbulence intensity did not reflect on the results as predicted. The three scenarios had relative high wind velocity that diminished the effect of the turbulence intensity. A low wind velocity was set up according to the data collected for TEEX1 in Table 13. The optimized LNG pool size was used with the gas phase velocity profile. Figure 70 shows the level concentrations along the downwind distance at 0.5 meters above the ground level. The simulation results showed a decrease of the concentration downwind as the turbulence intensity increased up to 1,000%. The change of LFL distance were significant for a turbulence intensity from 100% to 1000%.

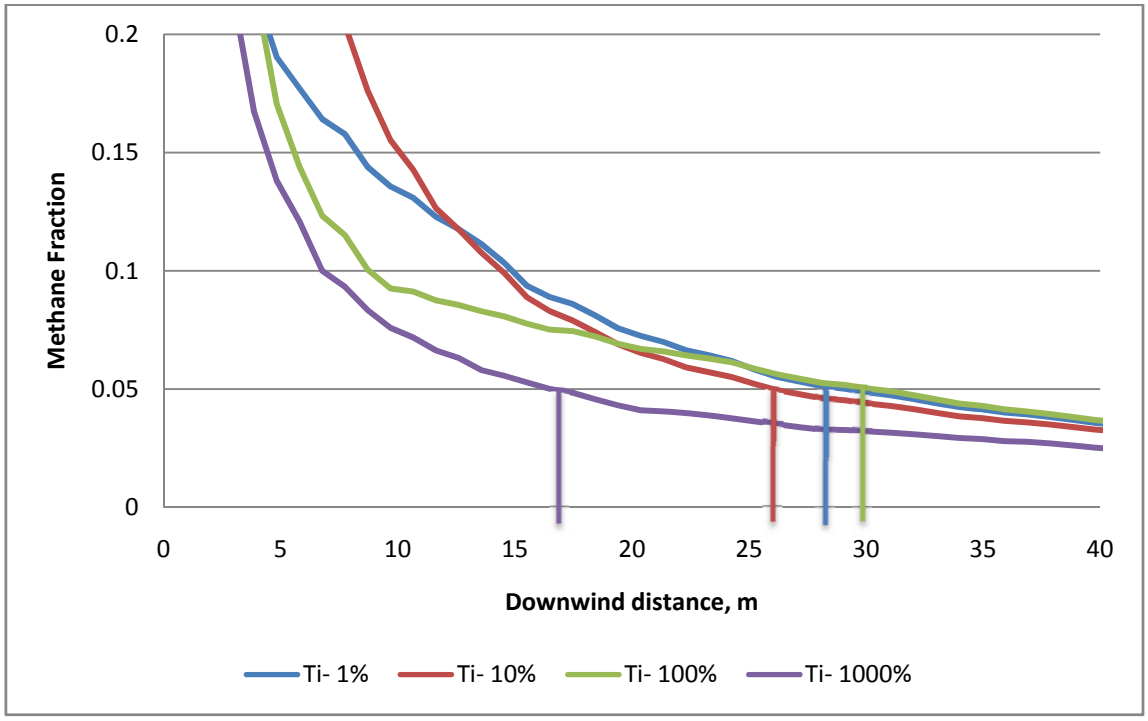

Figure 70. Concentration downwind for 15m^2 LNG pool

The circular LNG pool geometric simulation produced slightly lower LFL distance, but there was no strong evidence to explain the results other than a circular pool will provide more space on the corner of the fence to create larger eddies than with a rectangular shape.

4.3.2 Atmospheric conditions effect

The sensible heat flux and wind velocity influences the thermal mechanism inside the cloud as it travels downwind. The heat flux changes the mixing rate inside the cloud, while the wind entrains and mixes the vapor with air. Both mechanisms affect the shape of the cloud and the length. Low wind velocity will let the cloud being influenced by the gravity, resulting in a wide and large cloud traveling at the ground level. High wind velocity increases the entrainment of the cloud and forces the cloud to dilute quickly. The shape of the cloud will be elongated and narrow. Positive sensible heat flux will increase the mechanical turbulence inside the cloud, which will result on dilution of the cloud. Negative sensible heat flux will suppress the mechanical turbulence inside the cloud, which will lead to stable density profile.

Several runs were performed to study the effect of positive and negative sensible heat flux as well as the wind velocity while keeping other parameters constant. Since the temperature and wind profiles differ when the heat flux is positive or negative, the potential temperature and the velocity friction were modified to kept the same wind profile. The run QwB-001 was used as a reference case to compare the effect of the sensible heat flux and wind velocity on the 10% v/v and LFL distance at 0.5 meters above the ground. The release rate was set to 5 kg/s. The sensible heat flux was increased up to 250 W/m^2 (positive and negative). This heat flux value seems to be reasonable compared to the heat flux from a sunny day, around 800 to 900 W/m^2. The effect of the scenario is reported in Table 20.

Table 20. Summary of test performed on the sensible heat flux.

Run	*Sensible heat flux, W/m^2*	*Added heat flux W/m^2*	*Wind velocity at 2.5 m, m/s*	*LFL distance, (-4.5, y, 0.5), m*	*10% v/v distance, (-4.5, y, 0.5), m*
QwB_001	45	0	6.8	15	1
QwP_001	0	150	6.8	14	1
QwP_002	0	250	6.8	12.5	0.5
QwP_003	0	250	3	14	1
QwP_004	0	250	9	13.5	none
QwN_001	0	-150	6.8	22	9
QwN_002	0	-250	6.8	23	12.5
QwN_003	0	-250	3	26.5	15
QwN_004	0	-250	9	18	1

The results showed a small reduction of the LFL distance when the heat flux from the ground was positive. On the other hand, the negative heat flux created larger LFL distance. High concentration levels were observed in the downwind direction for the negative heat flux compared to the base case. Figure 71 shows the effect of sensible heat flux on the vapor cloud. A negative sensible heat flux increased not only the LFL distance (i.e. 5% v/v contour) but also increase the concentration up to 25 % v/v outside the fence at 0.5 meters above the ground level. The positive sensible heat flux decreases both concentration level and LFL distance.

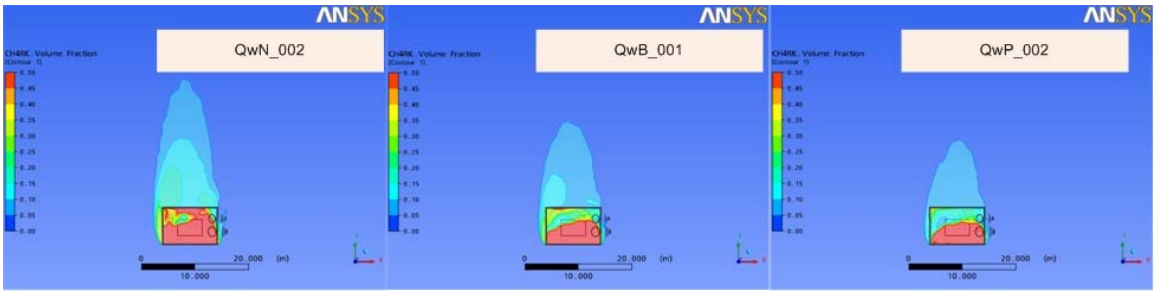

Figure 71. Concentration contour with constant wind velocity of 6.8 m/s, sensible heat flux, - 250, 50 (reference case), and 250 W/m^2

The wind velocity was increased from 3m/s to 9 m/s. Figure 72 shows the concentration profile at 0.5 meters above the ground for a constant negative sensible heat flux of 250 W/m^2. The results in the figure as well as in the Table 20 showed the increase of LFL distance as the wind velocity was reduced. The negative sensible heat flux showed a large gradient change compare to positive sensible heat flux. High wind velocity also showed that in both cases, the plume length was diminished. Figure 72 also showed that with a low wind velocity and negative heat sensible flux, the cloud had high level of concentration and a pronounced wide cloud.

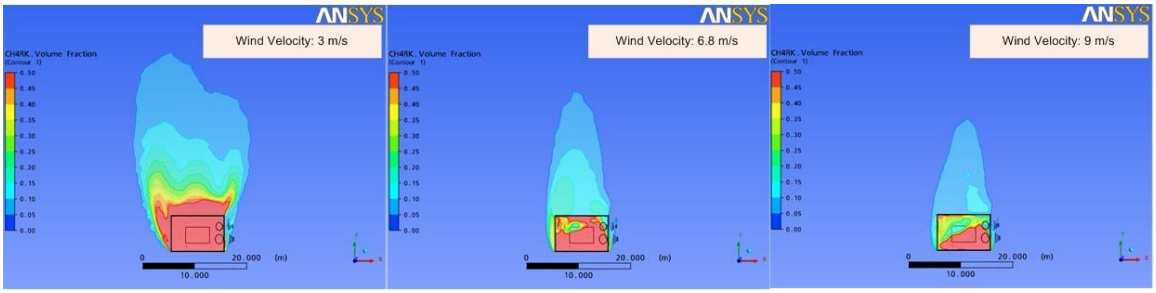

Figure 72. Concentration contour with negative sensible heat flux of 250 W/m^2, wind velocity from 3 to 9 m/s

4.4 Discussion

The wind velocity, obstacles, sensible heat flux and the mass released affected the LFL distance and concentration levels in numerical simulation that were performed in this paper. The increase of wind velocity augmented the mixing effect with vapors and ambient air, which

resulted in a reduction of the LFL distance. The LFL distances were changed by the effects of the obstacles for different wind direction. Negative heat flux increased LFL distance and concentration levels, while the positive heat flux reduced LFL distance and concentration levels. At any level of wind velocity, these parameters influenced LFL distance and concentration levels, but the effects were not linear.

The turbulence at the source, pool geometry and mass evaporation rate parameters seem to be a function of the wind velocity. At large wind velocity (above 2.5 m/s), these parameters had a slightly effects either on LFL distance or concentration levels in the downwind direction. At low wind velocity, the turbulence, pool geometry and mass evaporation rate had a noticeable effect on the downwind distance.

LNG pool area was a key parameter because of change of mass evaporation rate and the turbulence effect inside the fence. With open water surface area, the formation of eddies was limited.

In general, the circular LNG pool geometric simulation produced a slightly lower LFL distance, but there was no strong evidence to explain these results other than a circular pool will provide more space on the corner of the fence to create larger eddies than with a rectangular shape.

The mass evaporation rate seems to have different effects on the LFL distance. An accurate mass evaporation profile may be useful in the estimation of high methane concentration and early strategies to dilute the vapor cloud by water curtains for instance. The difference in LFL distance for each evaporation profile was relative small, but it may be significant for large release.

The turbulence intensity had the main effect on the vapor dispersion compare to any other variable in the source term modeling. This parameter increases the size of the cloud upward, letting the vapors mixing with ambient air. This may result an increase of concentration near the source but decrease in the LFL distance. A value above 100% seems to agree with the height of the cloud from collected data.

A turbulence intensity value of 1,000% seems large during the analysis of the data from CFD modeling. With a *Ti* of 1,000%, the estimated *k* and ε values were 5.8 and 3.6 m^2/s^2 at the source for the results, presented in Figure 70. These values seem to be on agreement with recent CFD simulation results from Gavelli. Gavelli reported a values of 9 m^2/s^2 for k value at the source (calculated from the video feed) for Falcon series with a wind velocity of 1.7 m/s (Gavelli, et al., 2008). These two results may confirm the use of high value for the turbulence intensity in the case of LNG release on water. During the course of these simulations, it was obvious that the wind velocity affected the parameter effect differently. Table 21 shows the classification of importance for each key parameters discussed here. It also provides a range of validity with respect to the wind velocity. For this work, the low wind velocity range was from 0.5 to 2.5 m/s and the large wind velocity range was from 2.5 to 7 m/s, where the observations from Table 21 were made.

Table 21. Estimation of the importance for the key parameters involved in LNG vapor dispersion modeling, release on water

Parameters	*Importance*	*Validity range*
Release rate	High	At large and low wind velocity
Pool shape, geometry	Medium	At low wind velocity
Pool area	High	At low wind velocity
Gas phase velocity profile (derived from the mass evaporation rate)	High	At low wind velocity
Turbulence at the source	High	At low wind velocity
Sensible heat flux from ground	High	At large and low wind velocity
Wind velocity	High	At large and low wind velocity
Temperature ambient	Medium	Not tested here
Surface roughness	Medium	Not tested here
Wind direction	Medium	At large and low wind velocity

LNG release on concrete showed a lower turbulence intensity compared to LNG release on water. The source term developed in the release on concrete seem to agree with the data collected, which confirmed the mass evaporation profile.

4.5 Conclusions

This chapter identified the parameters sensitivity on LNG vapor dispersion. It was found that some of these parameters depend on the level of wind velocity to be relevant to the simulation. For simulation with a low wind velocity, where the gravity effect was dominant, the parameters involving the source term had a significant influence on the downwind concentration.

This paper also intended to provide a methodology to assess releases on water or on concrete (i.e. an impoundment). The CFD model used in this paper gave a good agreement with the experimental data for wind velocity higher than 2.5 m/s (at 2.3 meters above the ground level). This paper provided a qualitative assessment of the parameters on the vapor dispersion. The quantitative assessment of the parameters will be further studied.

Most of the work presented was focusing on LNG release on water, especially the sensitivity analysis. Further work will be performed to perform the same type of analysis for LNG release on concrete and to assess the effect on the exclusion distances.

Computational fluid dynamics (CFD) was used to perform consequence modeling for LNG release. The CFD code showed a good agreement with the data collected during the November's 2007 test performed at BFTF for both LNG release on water and on concrete. This paper showed the setup of this simulation and the comparison with the data collected. Once the model was tuned against experimental data, it was used in a sensitivity analysis to assess the effects on the LFL distance and the concentration levels. The source term and the vapor dispersion parameters were studied. The sources term was composed of the turbulence intensity at the source, LNG pool geometry, mass evaporation rate and LNG pool area. The vapor dispersion parameters were the wind velocity, sensible heat flux, and the obstacles effects. It was concluded that at low wind velocity, the source term parameters influenced the LFL distance and the concentration level. In the other hand, at high wind velocity, the source term parameter had slightly effect on the LFL distance and the concentration levels.

CHAPTER V

CONCLUSIONS AND RECOMMENDATIONS FOR FUTURE RESEARCH

5.1 Conclusions

The study of the key parameters for LNG vapor dispersion through CFD codes has been presented in this dissertation.

The literature review was performed on the phenomenology of vapor dispersion and source term. During the literature review on vapor dispersion modeling, the source appeared simplified to a constant values or a source point. This assumption seemed to be good for the development of box models but in the use of more advance models, a detailed source term seemed more appropriate. The need for a detailed source term had a strong reflection on the simulation results at low wind velocity, where turbulence and various mass evaporation rates have different effects on the concentration level and LFL distance for a LNG vapor cloud.

The MKOPSC was involved in helping collect data during April 2006 tests at the BFTF. The data collected show interesting observation for the release on concrete. As the pit cools, the heat transfer is reduced and the vapor cloud dispersion is diminished. The foam application also relieved an initial increase in the evaporation rate and then it diminished. The release on water showed the high evaporation rate, where a mass evaporation profile was estimated from the heat transfer through the water. The water curtain application showed a reduction of the LFL distance. The foam application showed a reduction of the LFL distance and in the concentration level horizontally.

Based on the observation of the literature and the April 2006 test, the November 2007 test was designed to assess the effect of the source term on vapor dispersion with obstacles. This was improved during March 2008. The data collected was significant in the development of a source term for CFD application. New observations were made from LNG release on water. A hydrate/ice was formed at the location of the LNG pool reducing the mass evaporation. These effects increased the LNG pool diameter. The analysis showed that it was strongly linked to high flow rate (or discharge rate). Turbulences were observed inside the vapor fence increasing

the mixing before the wind entrained the vapors. These observations influenced the vapor dispersion and then they were further analyzed through CFD modeling.

The CFD code called CFX from ANSYS was used to perform consequence modeling for LNG vapor dispersion. The modeling approach was to tune the model against experimental data collected at the BFTF and then use the tuned modeling in sensitivity analysis. The CFD model was tuned against three tests, two release on water and on release on concrete. The model showed a good agreement with collected data. The sensitivity analysis was performed on selected parameters, source term definition, wind velocity, and sensible heat flux. The sensitivity analysis demonstrates the influence of the source term at low wind velocity in the concentration level inside the cloud and the LFL distance. The other parameters showed a less significant effect on the vapor cloud. Even though the analysis was qualitative, the conclusion of the sensitivity analysis helps to understand the behavior of the cloud with respect to the different parameter values. The sensitivity analysis also showed the influence of the wind velocity. At low wind velocity, the source term parameters had to be well refined to be able to obtain a certain agreement with data collected. At high wind velocity, the wind velocity overcomes any effects from the source term which made the simulation results less sensitive than with low wind velocity.

One major weakness in the model was observed. The turbulence effect on the source term was only modeled by two equations model (k and ε) as an overall. The turbulence may only produced by the evaporation phenomena but also from other sources.

5.2 Future work

This work proposed to review and advance the LNG consequence modeling through CFD codes and also provided a level of understanding for LNG vapor dispersion behavior through the sensitivity analysis. The future work to carry out this research further would be to use the current CFD code methodology to study passive barriers such as dike design.

To predict the whereabouts of a vapor cloud with respect to one scenario release is a passive approach to the LNG vapor dispersion problem. The consequence modeling should be carried out into the design phase where the passive system are designed to reduce the hazards of LNG

vapor dispersion. For instance, the dike system may be design as it increases the turbulence inside of the cloud to increase the mixing effects in order to reduce LFL distance.

The data analysis of the March 2007 should also be done. Preliminary results were available but not significant relevant to this dissertation. Addition tests are also needed to study the turbulence at source, which may influence the concentration levels and the LFL distance. During the tests and the analysis, three main sources of the turbulence were identified, (i) from the evaporation phenomena (cryogenic liquid onto water creates large evaporation bubbles), (ii) the impact contact at the discharge hose between LNG and water surface, including spreading and (iii) the external turbulence effects such as fluid velocity and wind entrainment effect on the inside of the fence. These turbulence sources should be studied, and their respective effects should be assessed.

The tests presented in this dissertation were designed for a calm release onto water. The next series of tests may include a release at different heights providing a plugging effect for the cryogenic liquid at the water surface. This release will create more turbulence at the water contact that should result in a large localized mass evaporation rate. A release underwater should also be considered.

REFERENCES

Alinot, C., & Masson, C. (2005). k-e model for the atmospheric boundary layer under various thermal stratifications. *Journal of Solar Energy Engineering*, *127* (2005), 438-443.

Alp, E., Alp, S., Guerin, S. G., Reid, J., Matthias, C. H., Napier, D., & Portelli, R. V. (1985). LNG spill and dispersion modeling. *Technical Seminar for Chemical Spills*, Toronto, Ontario Canada.

American Gas Association (1974). LNG safety program: Phase II. *American Gas Association*, Report Proj. IS-3-1.

ANSYS (2007). *CFX-11 Solver Theory Manual CFX Ltd.* Oxfordshire.

Baik, J., Raghunathan, V., & Witlox, H. (2006). Consequence modeling of LNG marine incidents. *7th Professional Development Conference and Exhibition*, Kingdom of Bahrain.

Briscoe, F., & Shaw, P. (1980). Spread and evaporation of liquid. *Progress in Energy and Combustion Science*, *6* (2), 127-140.

Brown, T. C., Cederwall, R. T., Chan, S. T., Ermak, D. L., Koopman, R. P., Lamson, K. C., McClure, J. W., & Morris, L. K. (1990). Falcon series data report 1987 LNG vapor barrier verification field trials. *Lawrence Livermore National Laboratory*, Report GRI-89/0138.

Burgess, D., Biordi, J., & Murphy, J. (1972). Hazards of spillage of LNG into water. *Bureau of Mines*, Report PMSRC 4177.

Burgess, D., Murphy, J., & Zabetakis, M. G. (1970). Hazards associated with the spillage of liquefied natural gas on water. *Bureau of Mines*, Report 7448.

CCPS (1999). *Consequence Analysis of Chemical Releases.* New York, N.Y.: AIChE.

Chan, S. T. (1983). FEM3, a finite element model for the simulation of heavy gas dispersion and incompressible flow, user's manual. *Lawrence Livermore National Laboratory*, Report UCRL-53397.

Chan, S. T. (1990). FEM3A, simulation of selected LNG vapor barrier verification field tests. *Lawrence Livermore National Laboratory*, Report UCRL-CR-105184.

Chan, S. T. (1984). FEM3C, an improved three-dimensional heavy-gas dispersion model user's manual. *Lawrence Livermore National Laboratory*, Report UCRL-MA-116567.

Chan, S. T. (1992). Numerical simulations of LNG vapor dispersion from a fenced storage area. *Journal of Hazardous Materials*, *30* (2), 195-224.

Chan, S. T. (1994). Recent upgrades and enhancements of the FEM3A model. *Lawrence Livermore National Laboratory*, Report URCL-ID-119749.

Chan, S. T. (1997). A three-dimensional model for simulation atmospheric dispersion of heavy-gases over complex terrain. *Lawrence Livermore National Laboratory*, Report UCRL-JC-127475.

Chan, S. T., Ermak, D. L., & Morris, L. K. (1987). FEM3 model simulations of selected Thorney Island phase I trials. *Journal of Hazardous Materials*, *16* (1987), 267-292.

Conrado, C., & Vesovic, V. (2000). The influence of chemical composition on vaporisation of LNG and LPG on unconfined water surfaces. *Chemical Engineering Science*, *55* (20), 4549-4562.

Cormier, B. (2007). Effect of tank pressure and insulation on LNG liquid flow rate - experience at Brayton fire school. *Mary Kay O'Connor Process Safety Center Centerline Newsletters*, *11* (2), 12-21.

Cormier, B., Wang, Y., & Mannan, M. S. (2006). LNG Mitigation Experiments - Preliminary Results. *Mary Kay O'Connor Process Safety Center 2006 International Symposium*, College Station, TX.

Cox, R. A. (1980). Methods for predicting the atmospheric dispersion of massive releases of flammable vapour. *Progress in Energy and Combustion Science*, *6* (2), 141-149.

Crowl, D. A., & Louvar, J. F. (2002). *Chemical Process Safety – Fundamentals with Application.* (2 Ed.). Upper saddle River, New Jersey: Prentice Hall PTR.

Davies, M. E., & Singh, S. (1985). Thorney Island: Its geography and meteorology. *Journal of Hazardous Materials*, *11* (1985), 91-124.

DeVaull, G. D., King, J. A., Lantzy, R. J., & Fontaine, D. J. (1995). *Understanding Atmospheric Dispersion of Accident Releases.* New York: Center for Chemical Process Safety.

Dharmavaram, S., Hanna, S. R., & Hansen, O. R. (2005). Consequence analysis - Using a CFD model for industrial sites. *Process Safety Progress*, *24* (4), 316-327.

DNV (2004). LNG marine release consequence assessment. *Det Norske Veritas (U.S.A) Inc.*, Report Project 70004197, Rev. No. 2.

Energy Information Administration (2004). Annual energy outlook 2004 with projections to 2025. 2006, <http://www.eia.doe.gov/oiaf/archive/aeo04/index.html>.

Ermak, D. L. (1990). User's manual for SLAB: an atmospheric dispersion model for denser-than-air releases. *Lawrence Livermore National Laboratory*, Report UCRL-MA-105607.

Ermak, D. L., Chan, S. T., Morgan, D. L., & Morris, L. K. (1982). A comparison of dense gas dispersion model simulations with burro series LNG spill test results. *Journal of Hazardous Materials*, *6* (1-2), 129-160.

Fay, J. A. (2003). Model of spills and fires from LNG and oil tankers. *Journal of Hazardous Materials*, *96* (2-3), 171-188.

Feldbauer, G. F., Heigl, J. J., McQueen, W., Whipp, R. H., & May, W. G. (1972). Spills of LNG onto water: vaporization and downwind drift of combustible mixture. *Esso Research and Engineering Co.*, Report EE61E72.

Ferziger, J. H., & Peric, M. (1999). *Computational Methods for Fluid Dynamics* (2nd). New York: Springer.

Gavelli, F., Bullister, E., & Kytomaa, H. (2008). Application of CFD (Fluent) to LNG spills into geometrically complex environments. *Journal of Hazardous Materials*, 10.1016/j.jhazmat.2008.02.037.

Gavelli, F., Bullister, E., & Kytomaa, H. (2006). Validation of Fluent predictions for LNG spills into an impoundment. *Mary Kay O'Connor Process Safety Center 2006 International Symposium*, College Station, TX.

Goldwire, H. C., Rodean, H. C., Cederwall, R. T., Kansa, E. J., Koopman, R. P., McClure, J. W., McRae, T. G., Morris, L. K., Kamppinen, L. M., Kiefer, R. D., Urtiew, P. A., & Lind, C. D. (1893). Coyote series data report LLNL/NWC 1981 LNG spill tests dispersion, vapor burn, and rapid-phase-transition. *Lawrence Livermore Laboratory*, *Volume 2*, Report UCID- 19953.

Hanna, S. R., Chang, J. C., & Strimaitis, D. G. (1993). Hazardous gas model evaluation with field observations. *Atmospheric Environment, Part A: General Topics*, *27A* (15), 2265-2285.

Hanna, S. R., Hansen, O. R., & Dharmavaram, S. (2004). FLACS CFD air quality model performance evaluation with Kit Fox, MUST, Prairie Grass, and EMU observations. *Atmospheric Environment*, *38* (2004), 4675-4687.

Hanna, S. R., Strimaitis, D. G., & Chang, J. C. (1991). Hazard response modeling uncertainty; a quantitative method. volume II: evaluation of commonly-used hazardous gas dispersion models. *Sigma Research Corporation*, Report F08635-89-C-0136.

Havens, J., & Spicer, T. (2005). LNG vapor cloud exclusion zones for spills into impoundments. *Process Safety Progress*, *24* (3), 181-186.

Havens, J., Walker, H., & Spicer, T. (1994). Wind-tunnel data sets for complex dispersion model evaluation. *Journal of Loss Prevention in the Process Industries*, *7* (2), 124-129.

Havens, J. A. (1988). A dispersion model for elevated dense jet chemical releases. *U.S. Environmental Protection Agency*, *Volume 1*, Report EPA-450/44-88-006a.

Havens, J. A., Spicer, T. O., Sheppard, W. V., & Perry, K. (2004). LNG terminal siting: FEM3A vapor dispersion model development. *American Institute of Chemical Engineers*, *1740-1752*, New Orleans, LA.

Hightower, M., Gritzo, L., Luketa-Hanlin, A., Covan, J., Tieszen, S., Wellman, G., Irwan, M., Kaneshige, M., Melof, B., Morrow, C., & Ragland, D. (2004). Guidance on risk analysis and safety implications of a large liquefied natural gas (LNG) spill over water. *Sandia National Laboratory*, Report sand2004-6258.

Hissong, D. W. (2007). Keys to modeling LNG spills on water. *Journal of Hazardous Materials*, *140* (3), 465-477.

Honeywell (2004). *Searchpoint optima plus infrared point gas detector: Operation Instruction,* Chicago, IL.

Humbert-Basset, R., & Montet, A. (1972). Dispersion dans l'atmosphere d'un nuage gazeux forme par epandage de GNL sur le sol. *Third International Conference & Exhibition on Liquefied Natural Gas*, *Session VI* Paper 4.

Incropera, F. P., & DeWitt, D. P. (2002). *Fundamentals of Heat and Mass Transfer.* (5th). New York: John Wiley & Sons.

Kakko, R. (1991). Computer aided consequence analysis and some future needs. *Journal of Hazardous Materials*, *26* (1991), 105-125.

Kneebone, A., & Prew, L. R. (1974). Shipboard jettison test of LNG onto the sea. *4th International Conference on LNG*, *Session 5 Paper 5*, Algiers.

Koopman, R. P., Baker, J., Cederwall, R. T., Goldwire, H. C., Hogan, W. J., Kamppinen, L. M., Kiefer, R. D., McClure, J. W., McRae, T. G., Morgan, D. L., Morris, L. K., Spann, J. M. W., & Lind, C. D. (1982). Burro series data report LLNL/NWC 1980 LNG spill tests. *Lawrence Livermore Laboratory*, *Volume 1*, Report UCID- 19075.

Kuhwoi, K., Park, K., Mannan, M. S., & Yoon, E. S. (2005). Safety analysis for LNG terminal focused on the consequence calculation of accidental and intentional spills. *Mary Kay O'Connor Process Safety Center 2005 International Symposium*, College Station, TX.

Luketa-Hanlin, A. (2006). A review of large-scale LNG spills: Experiments and modeling. *Journal of Hazardous Materials*, *132* (2-3), 119-140.

Luketa-Hanlin, A., Koopman, R. P., & Ermak, D. L. (2007). On the application of computational fluid dynamics codes for liquefied natural gas dispersion. *Journal of Hazardous Materials*, *140* (2007), 504-517.

May, W. G., McQueen, W., & Whipp, R. H. (1973). Dispersion of LNG spills. *Hydrocarbon Processing*, *52* (5), 105-109.

McCallen, R. C. (1988). Investigation of the finite element incompressible flow code FEM3: the model, some of its options, a guide in how to obtain and run the code, and its performance on some chosen problems. *Lawrence Livermore National Laboratory*, Report UCID- 21527.

Melhem, G. A. (1991). LNG release assessment. *Arthur D.Little*, Report 61230-30.

Meroney, R. N., & Neff, D. E. (1982). Dispersion of vapor from liquid natural gas spills-evaluation of simulation in a meteorological wind tunnel: five-cubic-meter China Lake spill series. *Journal of Wind Engineering and Industrial Aerodynamics*, *10* (1), 1-19.

Ohba, R., Kouchi, A., Hara, T., Vieillard, V., & Nedelka, D. (2004). Validation of heavy and light gas dispersion models for the safety analysis of LNG tank. *Journal of Loss Prevention in the Process Industries*, *17* (5), 325-337.

Olvera, H. A., & Choudhuri, A. R. (2006). Numerical simulation of hydrogen dispersion in the vicinity of a cubical building in stable stratified atmospheres. *International Journal of Hydrogen Energy*, *31* (2006), 2356-2369.

Opschoor, G. (1977). Investigations into the spreading and evaporation of LNG spilled on water. *Cryogenics*, *17* (11), 629-33.

Opschoor, G. (1980). The spreading and evaporation of LNG- and Burning-spills on water. *Journal of Hazardous Materials*, *3* (1980), 249-266.

Panofsky, H. A., & Dutton, J. A. (1984). *Atmospheric Turbulence.* New York: John Wiley & Sons.

Pasquill, F. (1974). *Atmospheric Diffusion.* (2nd). New York: John Wiley & Sons.

Pasquill, F. (1978). Atmospheric dispersion parameters in plume modeling. *U.S. Environmental Protection Agency, Office of Research and Development, Environmental Sciences Research Laboratory*, Report PB 82-261 959.

Peterson, R. L. (1990). Effect of homogeneous surface roughness on heavier-than-air gas dispersion. *Journal of Wind Engineering and Industrial Aerodynamics*, *36* (1990), 643-653.

Pitblado, R. M., Baik, J., Hughes, G. J., Ferro, C., & Shaw, S. J. (2005). Consequences of liquefied natural gas marine incidents. *American Institute of Chemical Engineering Process Safety Progress*,*24* (2), 108-114.

Puttock, J. S., Blackmore, D. R., & Colenbrander, G. W. (1982). Field experiments on dense gas dispersion. *Journal of Hazardous Materials*, *6* (1-2), 13-41.

Qiao, Y., West, H. H., & Mannan, M. S. (2005). Assessment of the effects of release variables on the consequences of LNG spillage onto water using FERC models. *Journal of Hazardous Materials*, *2006* (1-2), 155-162.

Shin, S. H., Meroney, R. N., & Neff, D. E. (1991). LNG vapor barrier and obstacle evaluation: wind-tunnel simulation of 1987 Falcon spill series. *Gas Research Institute*, Report GRI-91/0219.

Sklavounos, S., & Rigas, F. (2005). Fuel gas dispersion under cryogenic release conditions. *Energy & Fuels*, *2005* (19), 2535-2544.

Sklavounos, S., & Rigas, F. (2006). Simulation of Coyote series trials - Part I: CFD estimation of non-isothermal LNG releases and comparison with box-model predictions. *Chemical Engineering Science*, *61* (5), 1434-1443.

Sklavounos, S., & Rigas, F. (2004). Validation of turbulence models in heavy gas dispersion over obstacles. *Journal of Hazardous Materials*, *108* (1-2), 9-20.

Spicer, T. O., & Havens, J. A. (1986). DEGADIS - A heavier-than-air gas atmospheric dispersion model developed for the U.S. Coast Guard. *University of Arkansas*, Report 86-42.2.

Spicer, T. O., & Havens, J. A. (1987). Field test validation of the DEGADIS model. *Journal of Hazardous Materials*, *16* (1987), 231-245.

Spicer, T. O., & Havens, J. A. (1989). User's guide for the DEGADIS 2.1 dense gas dispersion model. *Environmental Protection Agency*, Report 86-42.2.

Vesovic, V. (2006). The influence of ice formation on vaporization of LNG on water surfaces. *Journal of Hazardous Materials*, *140* (3), 518-526.

Waite, P. J., Whitehouse, R. J., Winn, E. B., & Wakeham, W. A. (1983). The spread and vaporisation of cryogenic liquids on water. *Journal of Hazardous Materials*, *8* (2), 165-184.

West, H. H., & Mannan, M. S. (2001). LNG safety practice & regulations: From the 1944 East Ohio tragedy to today's safety record. *American Institute Chemical Engineers*, Houston, TX.

Witlox, H. W. M. (1994). The HEGADAS model for ground-level heavy-gas dispersion I. Steady-state model. *Atmospheric Environment*, *28* (18), 2917-2932.

Witlox, H. W. M. (1994). The HEGADAS model for ground-level heavy-gas dispersion II. Time-dependent model. *Atmospheric Environment*, *28* (18), 2933-2946.

Zeman, O. (1979). Parameterization of the dynamics of stable boundary layers and nocturnal jets. *Journal of the Atmospheric Sciences*, *36* (5), 792-804.

Zeman, O., & Lumley, J. L. (1976). Modeling buoyancy driven mixed layers. *Journal of the Atmospheric Sciences*, *33* (10), 1974-88.

Zinn, C. D. (2005). LNG codes and process safety. *Process Safety Progress*, *24* (3), 158-167.

Zuber, K. (1976). LNG facilities — Engineered fire protection systems. *Fire Technology*, *12* (1), 41-48.

VITA

Name: Benjamin R. Cormier

Address: Mary Kay O'Connor Process Safety Center

3122 TAMU

College Station, TX 77843-3122

Education: B.S. Chemical Engineering, Virginia Tech

M.S. Chemical Engineering, Texas A&M University

Ph.D. Chemical Engineering, Texas A&M University